

**MRI-TRACKABLE MURINE MODEL OF
CEREBRAL RADIATION NECROSIS**

by

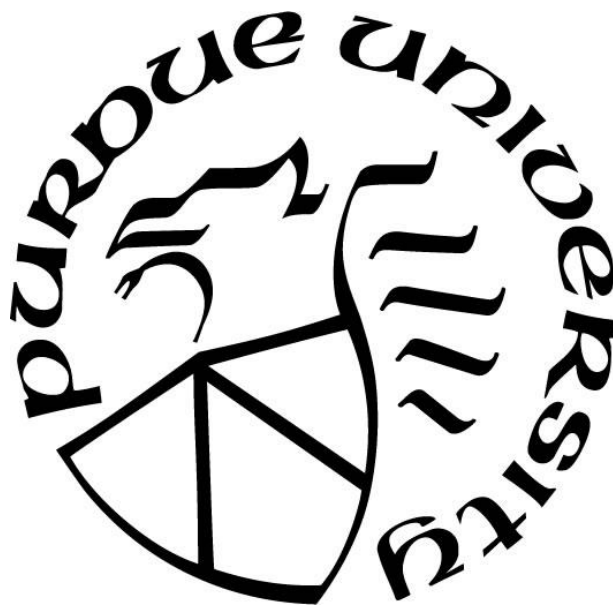
Andrew Joseph Boria

A Dissertation

Submitted to the Faculty of Purdue University

In Partial Fulfillment of the Requirements for the degree of

Doctor of Philosophy



Department of Health Sciences

West Lafayette, Indiana

May 2020

THE PURDUE UNIVERSITY GRADUATE SCHOOL

STATEMENT OF COMMITTEE APPROVAL

Dr. Carlos J Perez-Torres, Chair

Department of Health and Human Sciences

Dr. Keith M Stantz

Department of Health and Human Sciences

Dr. Linda H Nie

Department of Health and Human Sciences

Dr. Susan B Klein

Department of Physics at Indiana University, Bloomington

Approved by:

Dr. Aaron B Bowman

Dedicated to my family and friends

ACKNOWLEDGMENTS

I want to express my gratitude to my advisor Dr. Carlos J Perez-Torres for his continuous support during my Ph.D. studies and associated research, for his immense knowledge, for his motivation, and for his patience. His guidance was instrumental during my research as well as during the writing of this thesis. I could not have imagined a better mentor and advisor for my Ph.D. studies.

I would also like to thank the rest of my thesis committee: Dr. Keith M Stantz, Dr. Linda H Nie, and Dr. Susan B Klein. Their comments during committee meetings were insightful in broadening my knowledge and in helping to improve my research.

My sincerest thanks also go to Dr. Chang-Deng Hu for providing me access to the X-Rad 320 cabinet irradiator. Without this access, it would not have been possible to conduct this research.

I thank the members of my lab for the stimulating discussions and fun that we had during the course of my Ph.D. studies. Their comments during lab meetings also improved the research I carried out, which I am thankful to them for.

I thank Purdue University for providing me the Ross Fellowship which funded my Ph.D. studies.

Last but not least, I would like to thank my family: my father, my mother, and my sister for their endless support during writing this thesis and in my life in general.

TABLE OF CONTENTS

LIST OF TABLES	10
LIST OF FIGURES	11
ABSTRACT.....	12
PART I INTRODUCTION.....	13
Brain Cancer	13
Treatment of Brain Cancer	14
Surgery	15
Chemotherapy	16
Radiation Therapy	17
Radiation-Induced Injury in Human Patients	19
Radiation Necrosis.....	21
Radiation Protection	23
Mice Models	25
Efficacy of the X-RAD 320 Model	27
Impact of our Model	27
Future Focus of the Model.....	28
PART II – TECHNICAL CONSIDERATIONS	30
X-RAD 320 Filter Selection	30
Film Pixel Color to Dose Analysis	30
Dose Attenuation in the Vertical Plane	32
X-RAD 320 Setup.....	33
Initial Mice Positioning	33

Finalized Mice Positioning	33
PART III – INFLUENCE OF DOSE UNIFORMITY WHEN REPLICATING A GAMMA	
KNIFE MOUSE MODEL OF RADIATION NECROSIS WITH A PRECLINICAL	
IRRADIATOR	36
Abstract	37
Introduction.....	38
Materials and Methods.....	40
Setup and Treatment	40
Magnetic Resonance Imaging (MRI)	42
MRI Data Analysis	42
Histology.....	43
Statistics.....	43
Results.....	44
Increasing Radiation Dose Leads to Quicker Onset of Radiation Pathology	44
Radiation Necrosis Lesion Sizes either Plateau or Regress with Time	45
Histology Confirms the MRI Findings but Severity Does Not Correlate with Extent	48
Discussion	51
Acknowledgements.....	54
PART IV – MINIMAL DIFFERENCE BETWEEN FRACTIONATED AND SINGLE-	
FRACTION EXPOSURE IN A MURINE MODEL OF RADIATION NECROSIS	
Abstract	56
Introduction.....	57
Materials and Methods.....	58

Setup and treatment	58
Fractionation	58
Magnetic Resonance Imaging (MRI)	60
MRI Data Analysis	61
Statistics.....	61
Histology.....	61
Results.....	62
Discussion	63
Abbreviations.....	67
Acknowledgements.....	67
Authors' contributions	67
Funding	67
Availability of data and materials	67
Ethics approval.....	67
Consent for publication.....	68
Competing interests	68
 PART V – IMPACT OF MOUSE STRAIN AND SEX WHEN MODELING RADIATION	
NECROSIS	69
Abstract	70
Background	71
Methods.....	72
Setup and Treatment	72
Mouse strain and numbers	72

Magnetic Resonance Imaging (MRI)	73
MRI Data Analysis	73
Histology.....	74
Statistics.....	74
Results.....	74
In general, time post-irradiation and mouse strain significantly affect radiation necrosis modeling, while the effect of sex is minimal.....	75
There are differences between C57BL/6 and BALB/c mice but not between the N and J substrains of each strain.....	75
Discussion	77
Conclusion	81
List of abbreviations	81
Declarations	81
Ethics approval and consent to participate	81
Consent for publication.....	81
Availability of data and materials.....	81
Competing interests	82
Funding.....	82
Authors' contributions.....	82
Acknowledgements.....	82
APPENDIX A: SPSS T2-WEIGHTED MRI MIXED MODEL ANALYSIS	83
APPENDIX B: SPSS T1-WEIGHTED MRI MIXED MODEL ANALYSIS	101
APPENDIX C: SPSS HISTOLOGY ORDINAL REGRESSION ANALYSIS.....	117

PART VI – FUTURE DIRECTIONS AND CONCLUSIONS	123
Future Use of Murine Model of Cerebral Radiation Necrosis.....	123
Mouse Apparatus Positioning Accuracy.....	123
Future Fractionation Studies	124
Future Mouse Age and Sex Studies	126
Chronoradiosensitivity Mouse Study.....	127
Experimental Parameters and Reproducibility in Science.....	127
Radiation Necrosis Treatment Development.....	128
Radiation Necrosis: A Consequence of Radiation Therapy’s Success	129
REFERENCES	131

LIST OF TABLES

Table 1. Timeline and symptoms for the development of radiation-induced brain injury in human patients treated with fractionated whole brain irradiations.....	20
Table 2. BED and SFED calculated for three hypothetical α/β ratios for the four dose regimes used.	59
Table 3. Type III tests of fixed effects results for T2- and T1-weighted MRI lesion volumes from a linear mixed model and for histological grade from an ordinal model.....	76
Table 4. Pairwise comparisons of the main effects for T2- and T1-weighted MRI lesion volumes from a linear mixed model.....	77
Table 5. Pairwise comparisons of the interaction effects for T2- and T1-weighted MRI lesion volumes from a linear mixed model.	78

LIST OF FIGURES

Figure 1. Distribution of multiple brain cancer types by age.	14
Figure 2. Survival of tissues with low and high α/β values with and without fractionation.	19
Figure 3. Multiple human images of cerebral radiation necrosis.....	22
Figure 4. Diagram which shows the concept of the therapeutic index.	25
Figure 5. The energy spectrum produced with the X-RAD 320 using both of its filters.....	31
Figure 6. Whole field analysis of the X-RAD 320's 20 × 20 cm irradiation area.	32
Figure 7. Initial positioning of mice during X-Rad 320 irradiations.	34
Figure 8. Treatment setup used when delivering radiation to mice from the X-RAD 320.....	35
Figure 9. Time to onset of lesion on MRI as a function of dose.....	45
Figure 10. Lesion progression as a function of time post-irradiation and dose.....	46
Figure 11. Representative MRI images of murine radiation necrosis over time.	48
Figure 12. Representative histology images with increasing levels of severity.	49
Figure 13. Comparison of histologic grade to MRI images and radiation dose.	50
Figure 14. Lesion progression as a function of time post-irradiation.	63
Figure 15. Representative MRI and histology images of murine radiation necrosis.....	64
Figure 16. MRI lesion volumes and histological grade as a function of mouse strain and time post-irradiation.....	80

ABSTRACT

Cerebral radiation necrosis as a consequence of radiation therapy is often observed in patients several months to years after treatment. Complications include painful headaches, seizures, and in the worst-case death. Radiation necrosis is an irreversible condition with the options available to manage it all having noticeable downsides. As such, there is a critical need for better ways of either preventing the onset of necrosis and/or managing its symptoms. As radiation necrosis cannot be induced in humans for ethical reasons, a mouse model that mirrors the features of radiation necrosis observed in patients would allow for new techniques to be tested before being used in human clinical trials. This thesis will explain how our lab designed a murine model of cerebral radiation necrosis that uses a 320 keV cabinet irradiator to produce radiation necrosis and MRI and histology to evaluate the development of radiation necrosis at multiple time points.

Our model required the development of a mouse positioning apparatus that could be used in the cabinet irradiator used as well as the machining of lead shields so that focal semi-hemispheric irradiations could be conducted with other critical structures spared. The MRI scans used as well as the algorithm used to draw radiation necrosis lesions were based off what has been used in previous Gamma Knife models of radiation necrosis. Our initial work showed that since the cabinet irradiator has a relatively flat dose distribution unlike the Gamma Knife, the radiation lesion volumes produced in the former either plateaued or decreased, unlike in the case of the latter where lesion volumes tended to decrease over time. Further work analyzed the effects of fractionation and found minimal sparing using four different fractionation schemes. The effects of strain and sex on the development of radiation necrosis were also analyzed, with strain being found to be a statistically significant parameter while sex was not. Future research should focus on testing the effects of new drugs and techniques for better dealing with radiation necrosis.

PART I INTRODUCTION

Brain Cancer

Cancer is projected to become the number one cause of mortality globally in the next twenty years (1). In 2020, it is projected that in the United States 1,806,590 new cancers cases will occur with 606,520 cancer deaths projected with a corresponding mortality rate of ~33.6% (2). Of the new cases, it is projected that there will be 23,890 new cases of brain and other nervous system cancer (~1.3% of the total cancers that are projected) with 18,020 cancers deaths attributed to brain cancer (2). The corresponding mortality rate is ~75.4%, which puts brain cancer among the deadliest of all types of cancer. Brain cancer diagnosed in children is generally cured with a high rate of success, while adults generally are diagnosed with high-grade brain tumors that generally have a poor prognosis (3). In particular, there is a steep decline in the incidence of particular brain tumor types as a function of age as seen in Figure 1. In spite of brain cancer being an issue in younger patients, it is most commonly diagnosed in patients who are elderly, particularly patients who are 65 years old and older (4, 5), with the average age of diagnosis being 57 years old (6). As human life expectancy continues to increase, it is expected that more individuals will live long enough to develop brain cancer (7), with current data showing that individuals over 85 years old have the highest incidence of cancer (6). Several types of primary brain cancer are particularly deadly in older patients. For example, Glioblastoma, a diffuse glioma with an astrocyte origin, accounts for ~16% of all primary brain tumors in the United States and only has a median survival rate of ~15 months and a 5-year survival rate of 5% in patients age 55-64 (8-10). Several other types of brain cancers also have relatively low 5-year survival rates, with anaplastic oligodendrogliomas, low-grade (diffuse) astrocytomas, and anaplastic astrocytomas having rates of 46%, 22%, and 14% respectively in patients age 55-64 (10).

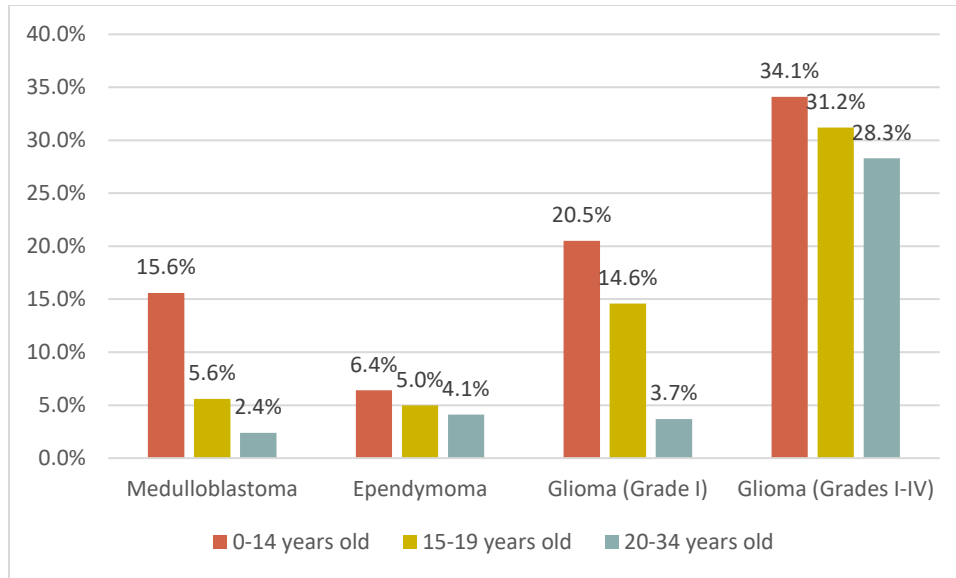


Figure 1. Distribution of multiple brain cancer types by age. Certain cancer types show a clear decline as patient ages increase. Data are from Merchant et al. (3).

Treatment of Brain Cancer

Brain cancer is particularly challenging to treat, as the brain is one of the body's most critical organs, and the location of the tumor within the brain may impede efforts to remove it via physical means. The brain being located behind the blood-brain barrier also poses challenges for chemotherapy, as the complex system of junctions and transport proteins is designed to keep substances out of the brain (11, 12). Compounding these issues is the rarity of brain cancers compared to cancers in other areas of the body, which limits the interest from the medical industry in developing new brain cancer treatments (13). As a result, the treatment of a diagnosed brain tumor is likely to depend on multiple factors, including patient factors such as health and age as well as tumor factors such as the tumor type, location, and size. Treatment options usually involve a mix of surgery, chemotherapy, and radiation therapy.

Surgery

Surgery is the oldest of the treatment options for treating cancer and is often the preferred way to treat cancerous tumors when the tumor type and patient health permit its use, with a surgeon often being the first member of a radiation oncology team a patient will meet (14). It is unique among the cancer treatment options in which surgery cures most patients with a single treatment, where both chemotherapy and radiation therapy usually require multiple treatments. Surgery is most effective and least expensive when it is performed for tumors that are local in their extent, such as early-stage and locally advanced cancers (15). Surgical removal is especially effective for solid tumors such as sarcomas, carcinomas, and lymphomas, with advancements in surgical techniques reducing both the mortality and the morbidity associated with removing solid tumors (14). Despite its advantages, surgery has its limitations, with surgical removal of advanced, diffuse, and/or metastatic cancers often not being possible. Brain cancers such as Glioblastoma in particular cannot be fully removed via surgical removal due to the diffuse nature and heterogeneity of the disease and the tendency for residual cancer cells after surgery to remain in the parenchyma, where they do not show up on imaging (16). Repeated surgical removal in such cases have been found to increase life expectancy though, with second, third, and fourth surgical interventions after reoccurrence of the disease being found to increase the survivability to 15.4, 22.4, and 26.6 months respectively, but surgery cannot cure patients of Glioblastoma and similar cancers (16). Furthermore, brain surgery requires breaking into the skull and potentially removing parts of the brain, which are likely to decrease patient quality of life. It is also estimated that 3.62% of brain surgeries have surgical complications that result in longer hospital stays, higher hospital costs, and other complications such as iatrogenic strokes which may

significantly increase the risk of morbidity (17). Because of these limitations, surgery may not be possible for patients with brain cancer, requiring them to rely on other treatment options.

Chemotherapy

Chemotherapy works by delivering medications called cytostatics to the body. There are several possible aims for chemotherapy: curative chemotherapy aims to eliminate all cancer cells in the human body outright, adjuvant chemotherapy aims to eliminate residual cancer cells following other treatments such as surgery, and neoadjuvant chemotherapy aims to shrink tumors so that they can be safely removed using surgery (18–20). Regarding curative chemotherapy, chemotherapy is particularly effective in treating cancers of the blood and bone marrow, with its use in treating acute lymphoblastic leukemia (ALL), the most common class of cancer found in children, having achieved a 5-year event-free-survival (EFS) rate of ~85% (21). For other types of cancers, chemotherapy is most often used in an adjuvant or neoadjuvant role, which is commonly the case in cancers found in the lungs (22), breast (23), pancreas (24). Its use in brain cancer though can be tricky, as many of the drugs used successfully in treating cancers in other parts of the body do not pass through the blood-brain barrier (11, 12). Of the types of cytostatics used that can pass through the blood-brain barrier, Temozolomide has proven useful, with it being the considered part of the primary standard of care for treating brain cancers such as Glioblastoma (25–27). Temozolomide and similar drugs have also been used alongside radiation therapy to treat brain cancers such as medulloblastoma and anaplastic astrocytoma (25, 28, 29). Despite its advantages, chemotherapy is usually not capable of treating brain cancers by itself with the exception of primary cerebral lymphomas (25). In addition, chemotherapy use in patients has multiple possible side effects that lead to a reduction in the quality of life such as

nausea, vomiting, ulceration, anorexia, anemia, and fatigue (30). Due to these side effects and other factors, it is estimated that 3%-19% of patients refuse the use of chemotherapy either partially or completely as a component of their cancer treatment (31). As a result of these limitations, chemotherapy plays a more supportive role in most types of brain cancer compared to either surgery or radiation therapy.

Radiation Therapy

The use of ionizing radiation for treating cancer has been used since shortly after the discovery of x-rays by Wilhelm Conrad Roentgen, with Emil Grubbe potentially being the first American physician to treat cancer using the newly discovered x-rays in 1896. Ionizing radiation is effective at killing cells by doing enough DNA damage so that cells are no longer able to undergo mitosis and eventually die via either direct ionization of DNA molecules or indirect ionization via creating reactive oxygen species due to the hydrolysis of water (32).

Unlike surgery or chemotherapy, radiation therapy is capable of being delivered both internally or externally, via brachytherapy and external beam radiation therapy respectively, with the vast majority of radiation therapy being delivered externally (33). The external delivery of radiation therapy makes it particularly attractive in cancer treatment, as other techniques such as surgery may not always be able to be used due to their invasive nature being risky on account of patient comorbidities. It is likely partially because of this that approximately 50% of patients receive radiation therapy with radiation therapy contributing to 40% of curative treatments (34).

Like other treatments for cancer treatment, the goal is to kill or remove all cancer cells while minimizing the damage to healthy tissue. This historically has been the reason for fractionated (external beam) radiation therapy, the most common way of delivering radiation therapy (35), for reasons related to the four R's of radiation therapy: repair, reoxygenation,

redistribution, and repopulation (36). The effectiveness of different fractionation schemes in the clinic can be estimated using the linear-quadratic model, which uses the dose per fraction, number of fractions, and α/β ratio to calculate the biologically effective dose (BED), which gives an estimate of the true biological dose delivered by a particular fractionated radiation scheme (37). Fractionation is particularly effective in brain cancer cases due to the difference in α/β values between cancer cells and healthy brain cancer cells, with the former usually being early responding tissue with an α/β value around 10 Gy, while the latter is considered late responding tissue with an α/β value around 2-3 Gy. This is because late-responding tissues with lower α/β ratios have a larger shoulder than cancer cells do on surviving fraction (of cells) vs dose curves as seen in Figure 2. This shoulder being preserved with the use of fractionation means that during brain irradiations, healthy brain cells are spared more than cancer cells. Patients who receive fractionated radiation therapy will receive either fractionated partial-brain radiation therapy or fractionated whole-brain radiation therapy (38). Concerning the latter, fractionated whole-brain radiation therapy is often the type of treatment prescribed for some cases of diffuse brain cancers as well as metastatic brain cancers, with its use in the latter case boosting the survival time of patients from one month to three to six months (39–43) with 30 Gy delivered in 10 fractions, with dose escalation beyond this not improving survival or local control (44). For cancers such as malignant gliomas, further dose escalation is recommended, with patients treated with less than 45 Gy assuming 1.8 to 2 Gy per fractionation having worse clinical outcomes (45). However, with the use of more aggressive dose treatments and with patients surviving longer as techniques and technology have improved, patients are more likely to experience complications from radiation-induced injury.

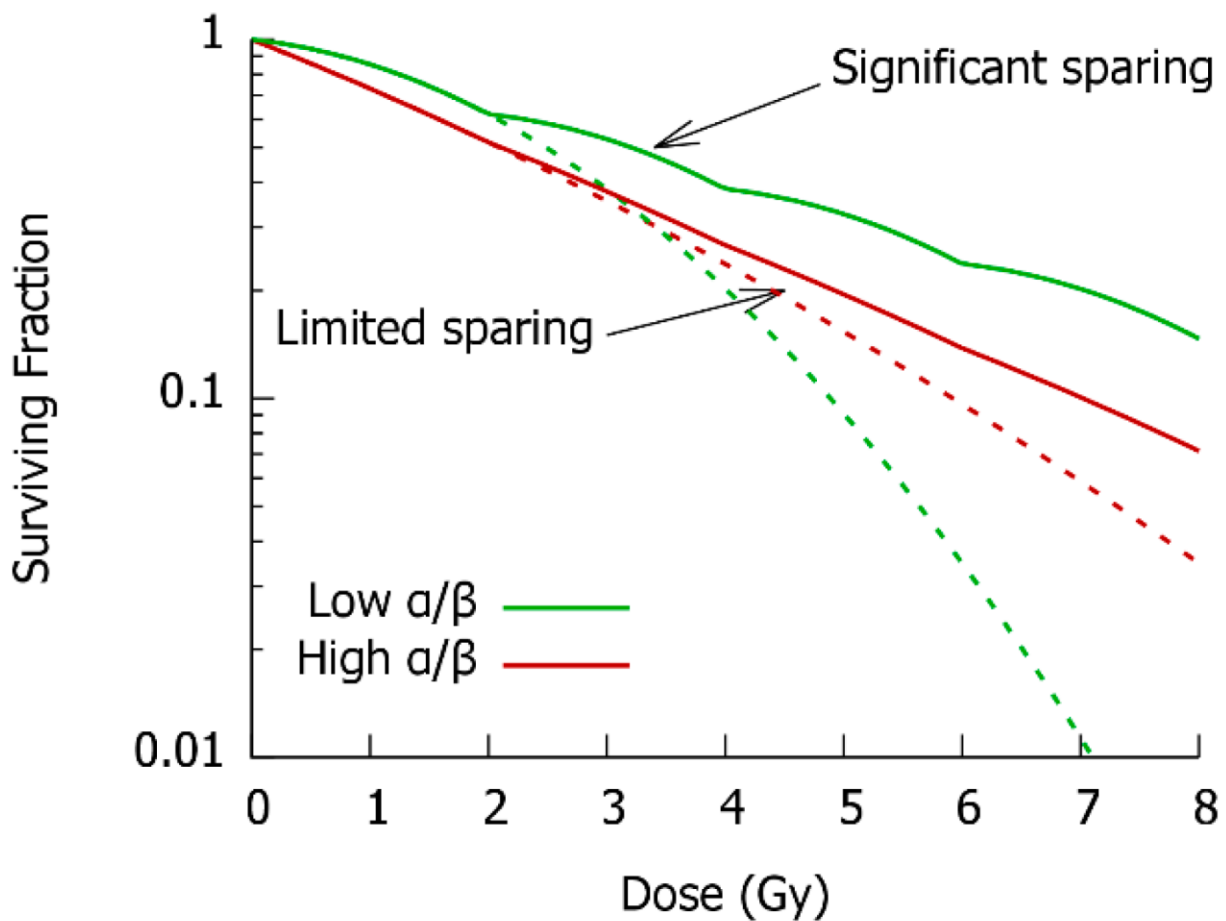


Figure 2. Survival of tissues with low and high α/β values with and without fractionation. Dashed lines indicate no fractionation while solid lines indicate fractionation. Late-responding tissue response (low α/β) is more curved than tumor cells (high α/β), which is what fractionation takes advantage of to spare late-responding tissue more than tumor cells during radiation therapy. This figure is reused from McMahon et al. (46) as allowed by *Cancers*'s MDPI Open-Access Creative Commons Attribution License.

Radiation-Induced Injury in Human Patients

Following the delivery of fractionated whole brain irradiation, the development of radiation-induced injury is possible, with the expression and appearance of this injury being divided into three main stages based on time after radiation delivery: acute, early-delayed, and late-delayed injury (38, 47) as can be observed in Table 1. The acute effects of radiation-induced injury are often expressed in a timespan ranging from days to weeks, with the acute symptoms being

Table 1. Timeline and symptoms for the development of radiation-induced brain injury in human patients treated with fractionated whole brain irradiations. Early, early-delayed, and late symptoms of radiation induced injury listed correspond to what are reported in Greene-Schloesser et al. (38).

Acute Symptoms (Days to Weeks)	Early-Delayed Symptoms (Weeks to Months)	Late Symptoms (Months to Years)
Drowsiness	Somnolence	Vascular Abnormalities
Edema	Attention Deficits	Demyelination
Headache	Transient Demyelination	Gliosis
	Short-Term Memory Loss	White Matter Necrosis
		Cognitive Impairment

edema, drowsiness, nausea, headaches, and vomiting due to increased cranial pressure (38, 48).

These acute symptoms usually do not last though, are reversible, and may be resolved without any medical assistance (48). At worst, corticosteroids may be necessary to suppress these symptoms, which are usually dexamethasone or methylprednisolone (48–50). Following the acute side effects being resolved, weeks to months after radiation therapy is delivered early-delayed side effects may appear. These symptoms include attention deficits, short-term memory loss, extreme somnolence (a state of strong desire for sleep and/or sleeping for unusually long periods), and potentially transient demyelination of cells in the brain as a result of encephalopathy (38, 48). Similar to acute symptoms, these early-delayed side effects also usually disappear after several months pass and usually are completely reversible (38, 48, 51).

More worrisome than either the acute symptoms or early-delayed symptoms are the late symptoms associated with radiation-induced injury. These symptoms are usually irreversible and often more severe than earlier side effects. The late symptoms are observed in a timespan of months to years, usually greater than six months after radiation delivery. The late effects include vascular abnormalities, gliosis (proliferation of glial cells in the central nervous system), demyelination, cognitive impairments, and white matter necrosis (38). If the late effects are particularly severe, dementia and death are a possible consequence.

Radiation Necrosis

Radiation necrosis, a late effect of radiation-induced injury, refers to the death of healthy tissue caused by radiation therapy, but also includes features such as telangiectasia, hyalinization, edema, calcifications, endothelial apoptosis, and neuroinflammation (52) as can be seen in Figure 3. It can occur as early in a matter of months, but usually it manifests within a timespan of one to two years (53). Its true incidence rate is hard to estimate, with it varying considerably based on treatment and diagnosis methods used, with rates of 3-63% being published in the literature (54–59). The symptoms of radiation necrosis include painful headaches, seizures, and in the worst-case death. The current treatments for radiation necrosis usually include steroids as long as patients can remain on them, hyperbaric oxygen therapy at centers that have this treatment available, and surgical removal of the necrotic lesion for patients who can handle surgery.

At present, radiation necrosis can be difficult to diagnose and manage as the symptoms and features of radiation necrosis are comparable to what would be observed with recurrent cancer (60). Radiation necrosis generally appears as focal lesions that can grow over time, which matches the features of growing tumors. As headaches and seizures are symptoms of both growing tumors and radiation necrosis, it is possible that patients could need medical treatment for one of these conditions and be diagnosed and treated for the other with deleterious consequences following.

Techniques for delineating radiation necrosis from recurrent cancer are currently being researched. The standard techniques for imaging the brain, conventional CT and MRI scans, usually do not give enough information to definitively determine whether focal lesions are composed of radiation necrosis or recurrent cancer (61). Biopsy of the focal lesions is considered the most reliable approach for differentiating radiation necrosis from recurrent cancer.

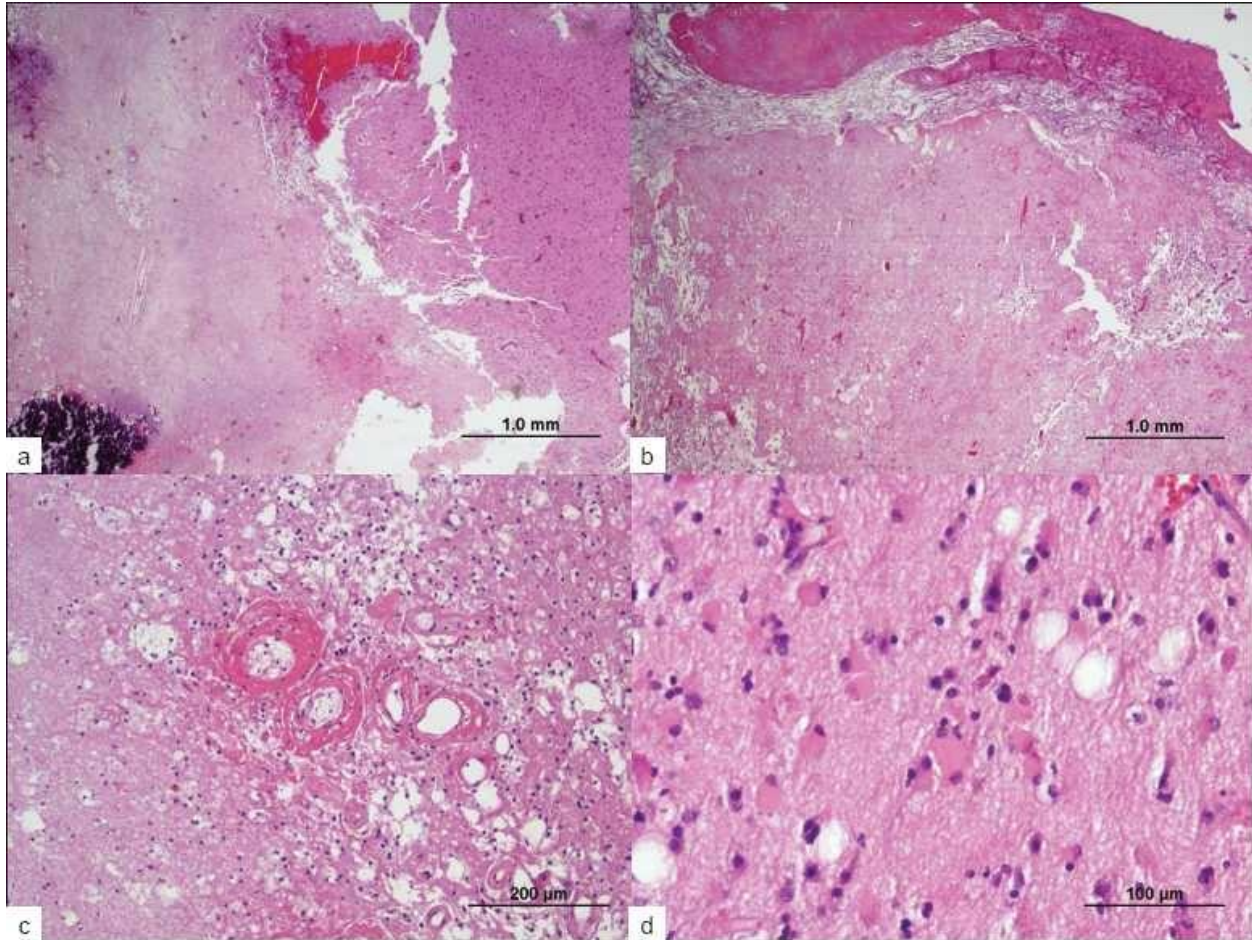


Figure 3. Multiple human images of cerebral radiation necrosis. The features include coarse calcium deposits (Panel a), leptomeningeal fibrosis (Panel b), hyalinized blood vessels (Panel c), and hypercellularity and cellular atypia (Panel d). This figure is reused from Chambliss et al. (62) under the terms of *Surgical Neurology International's* Open-Access Creative Commons Attribution License.

However, brain tissue biopsies are expensive, and surgery has risks associated with it that may prevent its use. The side effects of surgery also need to be considered, as surgical use will decrease the quality of life of patients that are already undergoing likely aggressive treatments to deal with cancer (52). As a result, current research efforts have focused on noninvasive techniques for delineating radiation necrosis from recurrent cancer. Diffusion-based MRI, which images the diffusion of water in tissue, has been investigated, yet it remains in an exploratory stage. It has multiple challenges to get working, which include measurement values such as

apparent diffusion coefficients (ADC) varying significantly based on the scanner used, a current lack of understanding how processes such as necrosis and scar tissue formation affect the measurement values, and limitations with resolving lesions that are a mixture of recurrent cancer and radiation necrosis (52, 63–66). MR perfusion imaging has also been explored as a technique for distinguishing recurrent cancer from radiation necrosis. It is promising since tumor recurrence is associated with increased permeability around the tumor site, while radiation necrosis generally is associated with regions of decreased perfusion such as coagulative necrosis (52). It too is currently being investigated for its benefit in the clinic. MRS also has been investigated. Tumors have been found to have noticeably higher choline to creatine and choline to NAA ratios than radiation necrosis (64, 67, 68). The current limitations of MRS as a tool for differentiating recurrent cancer from radiation necrosis are its relatively low spatial resolution and issues with classifying cases where both recurrent cancer and radiation necrosis are present (52).

Radiation Protection

Radiation protection usually involves the safety protocols necessary to keep dose levels to staff members as low as reasonably achievable (ALARA), which usually involves following three basic rules: minimize the amount of time staff members are exposed to ionizing radiation, maintain a good amount of distance between staff members and sources of ionizing radiation, and maintain adequate levels of shielding to reduce doses to staff members. While radiation therapy staff should be following these rules, radiation protection from a patient standpoint is very different. Patients cannot as easily be spared dose that is being delivered to them to cure their cancer. Instead, the focus of radiation protection is incorporated into the therapeutic index, which is best represented as a pair of sigmoid curves that measure the probability of tumor

control and the probability of complications as a function of dose which can be observed in Figure 4. Radiation protection and the probability of complications thus must be leveraged against the probability of tumor control. With uncontrolled cancer growth being the worst possible outcome for a patient, radiation protection may have to be considered a secondary concern to giving enough dose to be able to eradicate all traces of cancer in patients. Radiation protection can however be improved by increasing the therapeutic index, which means widening the distance between the probability of complications and the probability of tumor control. In theory, this is either accomplished by using radioprotectors to shift the probability of complications curve to the right or with radiosensitizers by shifting the probability of tumor control curve to the left. The concept of the therapeutic index is part of why fractionation is used: it acts as a radioprotector which shifts the probability of complications more to the right than it shifts the probability of tumor control to the right. Regarding drugs that act as either radioprotectors or radiosensitizers, there are no radiosensitizer drugs which are clinically approved for use in patients and only one clinically approved radioprotector: Amifostine, which has been shown to reduce the side effects associated with radiation therapy without protecting tumors in head and neck cases (69). The development of new radiosensitizers and radioprotectors would improve patient outcomes both in curing patients of cancer and from a radiation protection standpoint by decreasing the risk of complications from radiation-induced injury. However, the development of new radiosensitizers and radioprotectors requires the use of a radiation-induced injury model in order to study their effects. As ethical considerations prevent inducing radiation necrosis in human subjects, the use of proxy models such as animal models are necessary. However, the use of a mouse model to study the human condition requires the mouse model to be well characterized and for mice to as closely as possible exhibit the kinds of features and

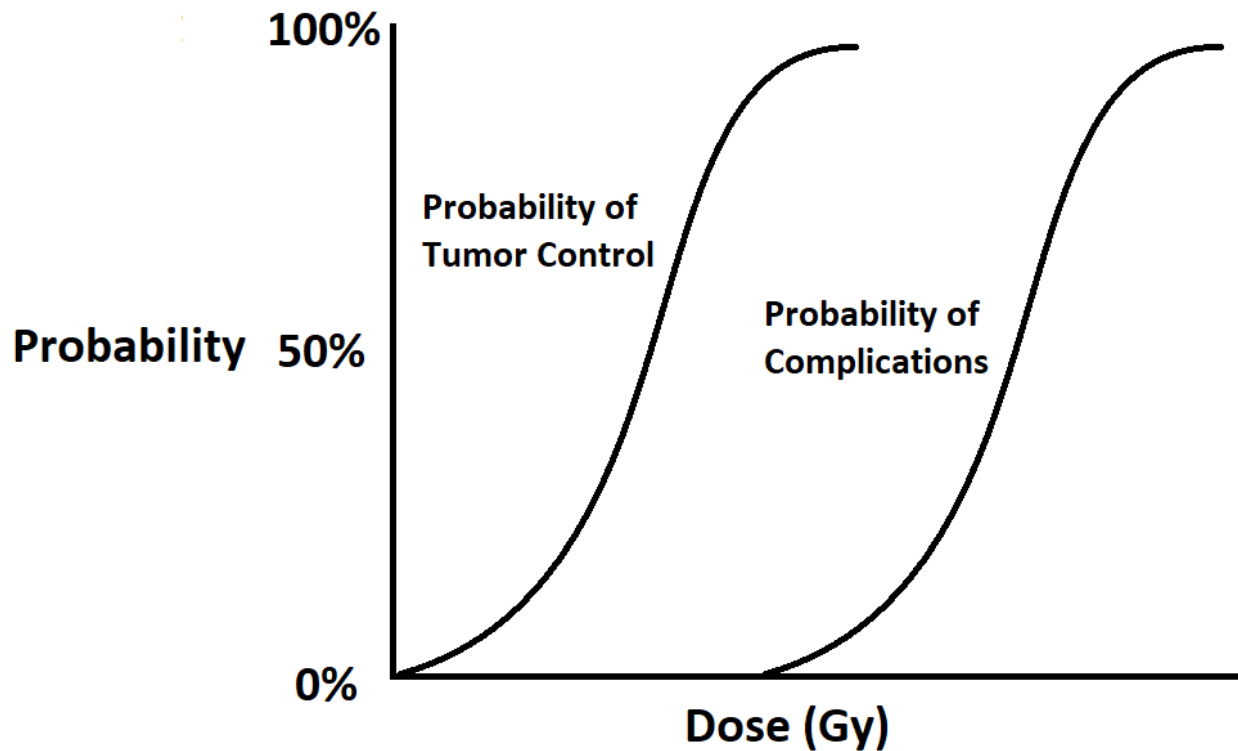


Figure 4. Diagram which shows the concept of the therapeutic index. A large difference between the probability of tumor control and the probability of complications corresponds to a large therapeutic index.

pathology that would be exhibited in humans. With these challenges accomplished however, the development of new ways of improving patient outcomes is possible.

Mice Models

As further study of radiation necrosis is necessary to develop new ways of treating the condition and because radiation necrosis cannot be induced for the purpose of studying it in humans due to ethical reasons, animal models such as mice models are necessary. Unlike other animal models which may be prohibitively expensive, many mice can be bought for a relatively inexpensive amount, which helps studies reach the power they need to obtain statistically significant results.

Mice also can also be handled with minimal training and can be anaesthetized more easily than larger, more complex animals, which is why they are a popular research animal.

However, the use of mice in research does present its own sets of challenges. The mouse brain is particularly small in comparison to other animals used in research, which requires very precise positioning in order to be consistent when conducting irradiations to induce radiation necrosis. Furthermore, it is common in preclinical animal work to conduct irradiations using ^{137}Cs (70–72) and orthovoltage irradiators (73–75) due to the lower cost of these devices compared to LINAC or Gamma Knife machines and the low depth penetration being adequate for mice. Mice are also more radioresistant than humans, which can be observed most easily from whole body irradiation data, with the dose to kill 50% of humans after 60 days ($\text{LD}_{50/60}$) being ~3.5-4.5 Gy (76–78) with the dose to kill 50% of mice after 30 days ($\text{LD}_{50/30}$) being ~7-9 Gy (79–82) respectively. The higher doses in mice needed to obtain similar pathological features as those observed in humans may complicate the translation of treatment results, with the exact pathological features exhibited in humans not being exhibited in mice. These and other factors may explain why the average rate of successful translation of animal models to human cancer trials is less than 8% (83).

Even when these limitations are considered, research performed with mouse models remains a cornerstone of preclinical work. Many of the drugs that are now commonly used by people were first tested via preclinical work such as with mouse models. Furthermore, other animal models such as those that use minipigs are also far more expensive than those that use mouse models, which limits the number of animals that can be used in these studies, hurting statistical power. Thus, as the NIH and other organizations require testing in at least two animal models before work can proceed to human trials, it is likely for the foreseeable future that a more

inexpensive animal model will be used first such as a mouse model to test for initial efficacy. This would then be followed by other animal models that are more expensive and use more complex animals which are more similar to humans to further verify efficacy before moving to human testing.

Efficacy of the X-RAD 320 Model

Our present and past mouse work has focused on the development of our mouse model that generates cerebral radiation necrosis using an X-RAD 320 (Precision X-Ray, North Branford, CT) cabinet irradiator. Our model is based off of previous work using Gamma Knife irradiations (84–87), with the Gamma Knife model of cerebral radiation necrosis being a particularly prominent and well-characterized model. However, the Gamma Knife is not available at many institutions due to its radiological concerns and high cost, which limits the ability to replicate and reproduce work using it. The X-RAD 320 is not as expensive and does not use radioactive sources like the Gamma Knife does. It is thus our intention that our X-RAD 320 model of radiation necrosis would be an excellent but affordable alternative to other models such as with the Gamma Knife.

Impact of our Model

Three different studies so far have been performed using our model. The first study focused on how dose uniformity affected radiation necrosis development by looking at the different growth patterns of radiation necrosis in mice that were irradiated with the Gamma Knife vs the X-RAD 320. The second focused on how fractionation would affect the development of radiation necrosis compared to the results exhibited with prior single fraction radiation delivery. The third study analyzed how the substrain and sex of mice used could affect the radiation necrosis

development. These studies together show how important it is in model design to carefully decide on their parameter choices. Of the many different labs that are using radiation in preclinical mouse models, the machine used to deliver radiation, choice of whether to fractionate or not, and the particular type of mouse used together each constitute a model. Study results could potentially differ considerably based on these choices, which makes comparing the results of different lab groups difficult. The greatest impact of this research thus is likely to be in reminding fellow scientists to be careful about their parameter choices during model design.

Future Focus of the Model

The work performed in our studies so far has focused on how particular parameters affect the development of radiation necrosis while improving the model's precision. Future work could potentially be done in both areas, with parameters such as age of the mice not yet being tested to see how it affects radiation necrosis development and other improvements to the model apparatus being possible such as the introduction of ear bars to hold mice more tightly during irradiations. There is a desire though to use the model to test the efficacy of different treatments that could potentially impair the development of radiation necrosis or better manage its symptoms than what is currently available. As such, testing a wide variety of drugs to see if they impair the development of radiation necrosis and act as a radioprotector is likely to be an important focus. For this to be an effective effort though, this type of study would need to be coupled with a similar study in a tumor model due to a radioprotector only being useful if it protects healthy tissue more than a tumor, which means the therapeutic index is being widened. In a similar manner, if a tumor model found that a radiosensitizer was effective at lowering the dose needed to cause a similar level of damage, said radiosensitizer could be used in our model

with the hope that it would not worsen the degree of damage done to healthy, with this also proving that the therapeutic index has been widened.

While a mouse model is a good place to start when testing the efficacy of new potential radioprotectors and radiosensitizers, further testing will need to be performed in another animal model before human trials can begin according to FDA regulations. This is to provide further verification of any treatment's efficacy as well as prove that the effectiveness of the treatments in question are not a mouse-only phenomenon. It is thus expected that an evolution of our model will be the development of another animal model which is more similar to humans. However, as any animal that is more similar to people will cost more to obtain and maintain, it is expected that mice will remain pivotal in the initial testing of new treatments of radiation necrosis work for the foreseeable future.

PART II – TECHNICAL CONSIDERATIONS

We utilized the X-RAD 320 (Precision X-Ray, North Branford, CT) to conduct irradiations. To be able to carry out small animal irradiations with the X-RAD 320, several design choices and calibrations had to be performed. This section aims to clarify to researchers what steps were taken in the model development.

X-RAD 320 Filter Selection

The X-RAD 320 utilizes a 320 keV energy spectrum with a current of 12.5 mA. The output energy spectrum can be shaped based on the choice of filter which is used, with the energy spectrum that each filter produces being visible in Figure 5. Of the two filters which were available, we noted that the dose rate of the first filter, marked “F1”, was approximately 2.2 Gy per minute, while the second filter, marked “F8”, had a dose rate that was less than 1.0 Gy per minute. To be able to conduct animal irradiations within a reasonable window of time and to avoid biological complications that are associated with low dose rates, we chose to use the first filter, which has a HVL of approximately 1 mm of Cu.

Film Pixel Color to Dose Analysis

In order to determine the dose distribution of the X-RAD 320’s radiation field, EBT2 Gafchromic film (Ashland[®], Covington, KY) was irradiated over the span of the X-RAD 320’s 20 × 20 cm field with doses ranging from 0.1 Gy to 10 Gy. The film was scanned using a Perfection V600 Photo Scanner (Epson[®], Suwa, Nagano, Japan) in both film mode and reflective mode, with film mode being used due to a slightly better image quality. ImageJ (National Institutes of Health, Bethesda, MD) was then used to extract the pixel information into red,

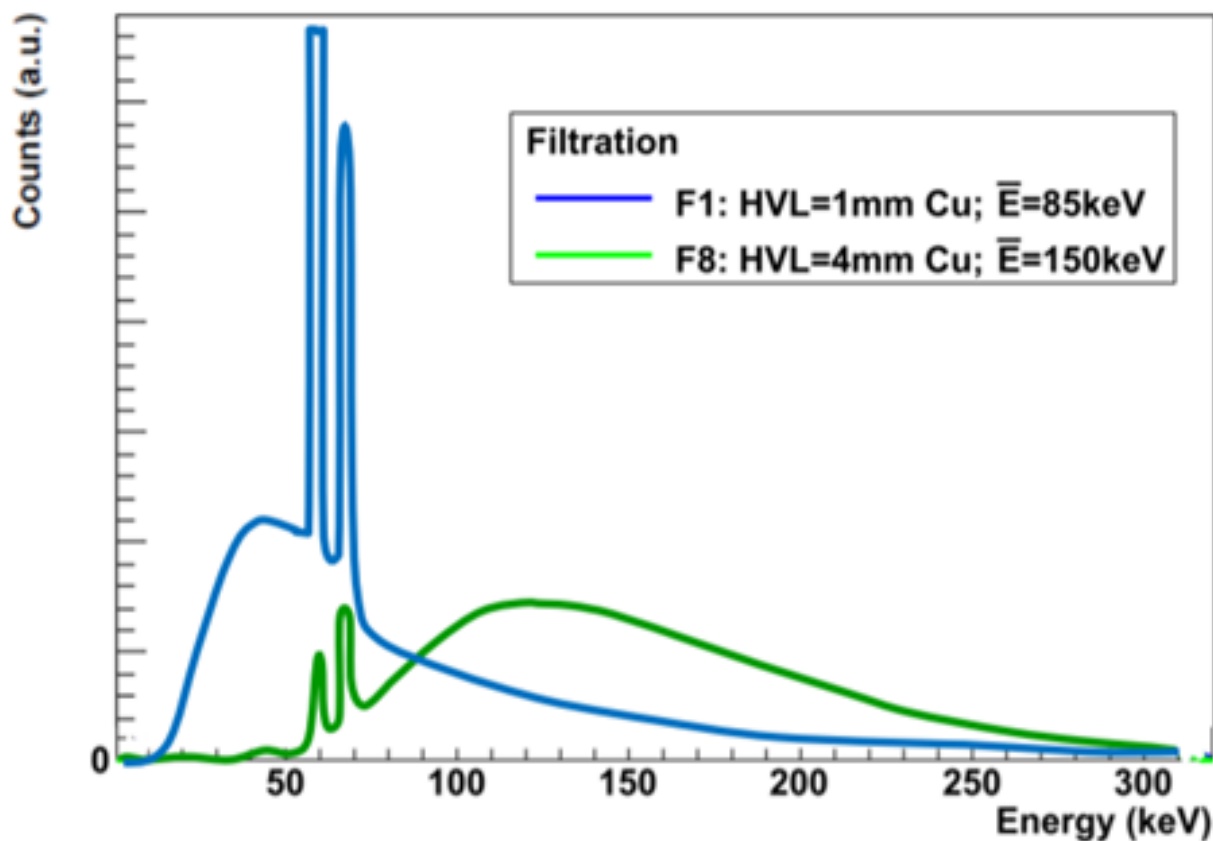


Figure 5. The energy spectrum produced with the X-RAD 320 using both of its filters. The second filter, listed as “F8”, is more attenuating than the first filter, listed as “F1”. This causes the energy spectrum of the second filter to be significantly more hardened than with the first filter, resulting in an average energy of 150 keV with the second filter as opposed to 85 keV as seen with the first filter.

green, and blue channels over the entire span of the irradiated field. MATLAB[®] (MathWorks[®], Natick, MA) was then used to design separate exponential fits of the data with dose as the dependent variable and each of the three colors as the independent variable, with the final dose prescribed to pixels being the average dose from the three exponential fits of the data. Following the calibration, film was irradiated over the span of the 20 × 20 cm field on the table holding the mouse apparatus as well as on a steel plate on top of the table. The analysis can be seen in Figure 6. The heel effect is observable particularly in Panel A in the form of less dose being delivered to

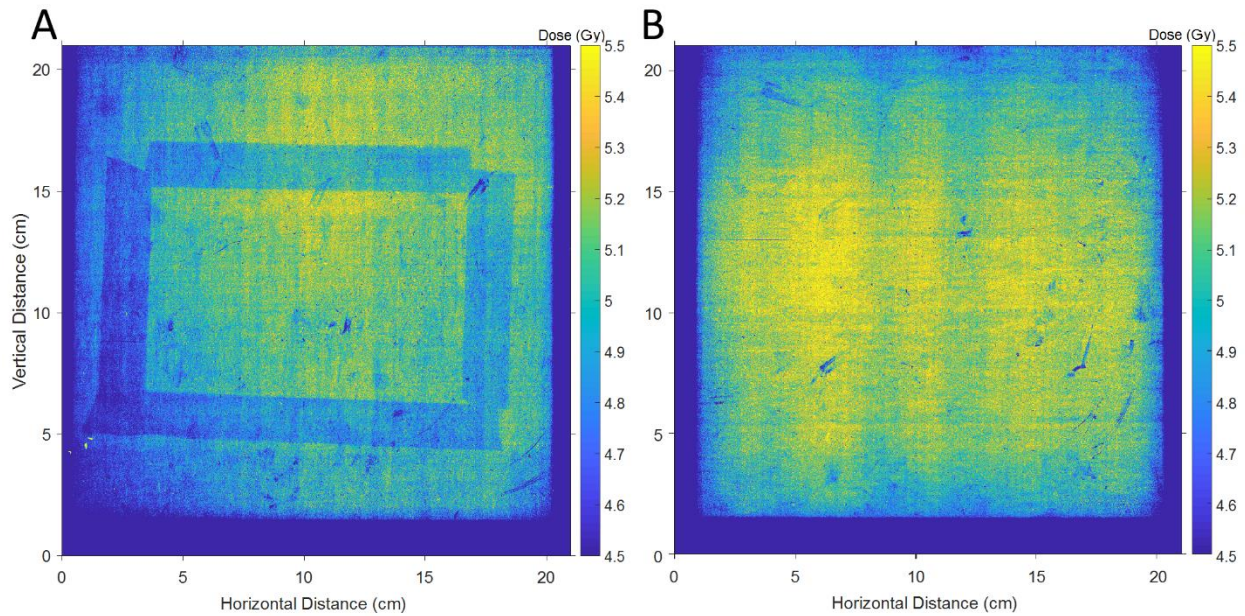


Figure 6. Whole field analysis of the X-RAD 320's 20×20 cm irradiation area. Analysis of the whole field of the X-RAD 320 was performed at 50 SSD both on the table the mouse apparatus sits on (Panel A) as well as on a steel plate (Panel B) which was placed between the table and film to remove the film artifact (visible as a rectangular pattern of dose loss in Panel A). Particularly in Panel A, the Heel Effect is observable as a reduction in dose on the left side of the X-RAD 320's field.

the left side of the field. This finding led us to position mice near the center of the beam away from the left side to maintain a relatively consistent horizontal dose distribution.

Dose Attenuation in the Vertical Plane

The X-RAD 320 lacks an MLC as would be found in medical LINACs to shape the irradiative field to the target of interest while sparing other critical structures. To address this, machined lead plates were used that could be placed over the mouse holding apparatus that had 0.5×0.5 cm openings to allow for semi-hemispheric cerebral doses to be delivered to mice. To analyze the attenuating effect of the lead plates, EBT2 Gafchromic film was placed within the mouse holding apparatus under the lead plates during irradiations. It was determined that a single lead plate would attenuate $87.7 \pm 1.0\%$ of the beam while two lead plates together would attenuate

93.1 \pm 0.7% of the beam. As doses as high as 100 Gy would be delivered using this model, two lead plates were used to keep doses to non-targeted critical structures below 10 Gy.

The dose loss attributed to attenuation within mice was measured using a water phantom with film positioned above and below it during irradiations. The dose was found to be 30% less in the bottom film for a water phantom with a diameter of 17 mm giving a dose reduction of 1.76% per mm of depth.

X-RAD 320 Setup

Initial Mice Positioning

Initial irradiations using the X-RAD 320 were performed using five mice at a time as can be observed in Figure 7, where the centerline of Position 3 was placed at the center of the irradiation field. This was not ideal though, as the position in the mouse cerebrum dose was delivered to shifted based on which position a particular mouse was placed at, with some of the dose not actually being delivered to the mouse cerebrum at particular positions. Furthermore, mice placed at Position 4 (labelled in Figure 7) usually had to be sacrificed shortly after irradiations were performed, likely as a consequence of large doses being delivered to the tongue at this position.

Finalized Mice Positioning

Due to the limitations of the previous setup, the number of mice irradiated at a time as well as the positions of the mice irradiated were adjusted, with the lead shields used also having to be redesigned. In the final setup as seen in Figure 8, two mice are positioned to receive dose to opposite but equal volumes of the brain. The positions of the mice within the apparatus are at what were originally Positions 2 and 3 in Figure 7, although several changes have been made to the setup. The apparatus has been pushed to the right so that the X-Rad 320's field vertical

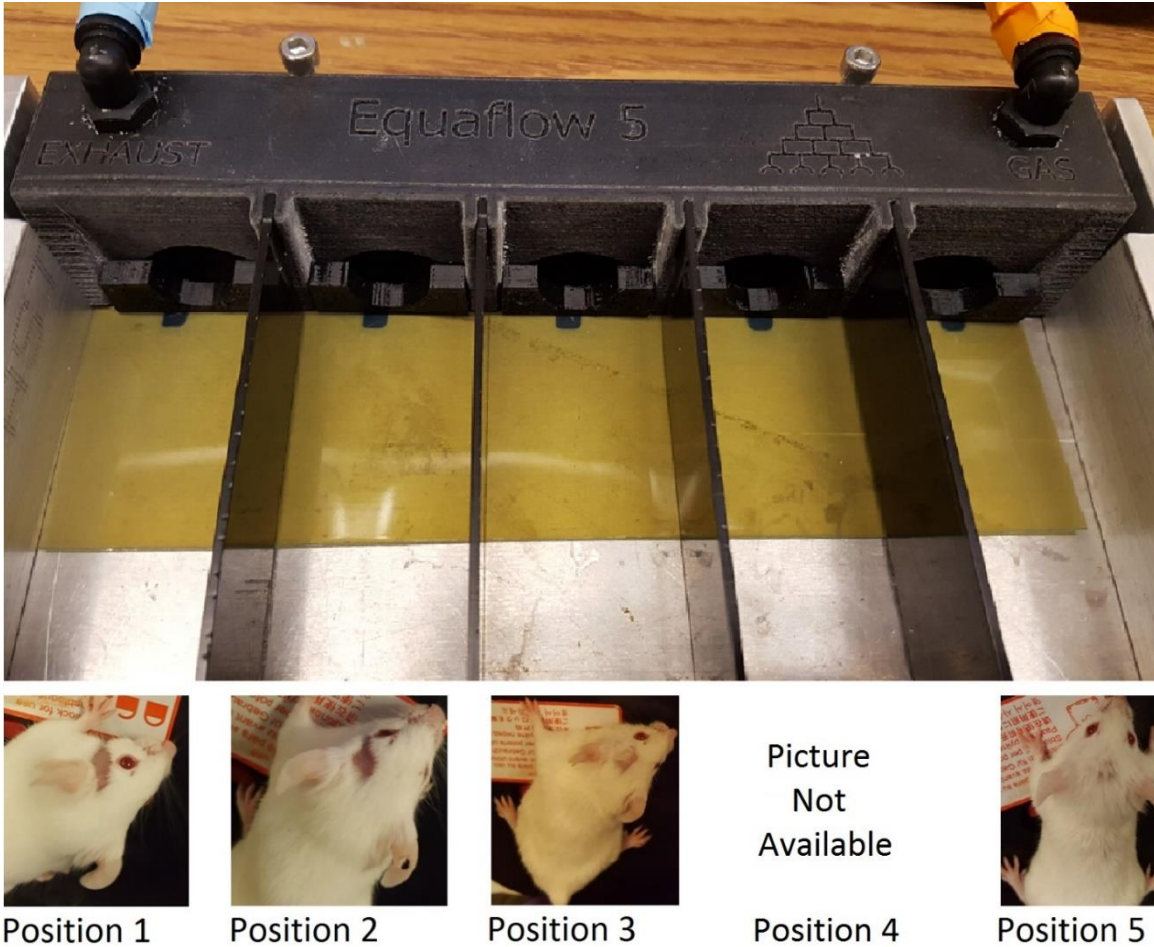


Figure 7. Initial positioning of mice during X-Rad 320 irradiations. Mice were initially irradiated five at a time at positions labelled 1 through 4. However, there were several issues with this arrangement. The position of dose delivery was also not consistent at the positions as can be seen by the movement of the alopecia and dark film spots based on which position a mouse was placed at. Also, mice irradiated at Position 4 often had to be sacrificed shortly afterward due to weight loss, which is why a picture of the alopecia at this position is unavailable.

midline now falls between Positions 2 and 3. The lead plates placed above the mouse holding apparatus have also been remade, with holes present only above Positions 2 and 3, with the hole above Position 3 moved to the right so that the distance between the two holes to the vertical midline is equal. The result is that opposite but equal volumes in the two mice irradiated at the same time are irradiated. As five mice are irradiated in total per group, three irradiations are needed to irradiate all of them, with one mouse being irradiated by itself.

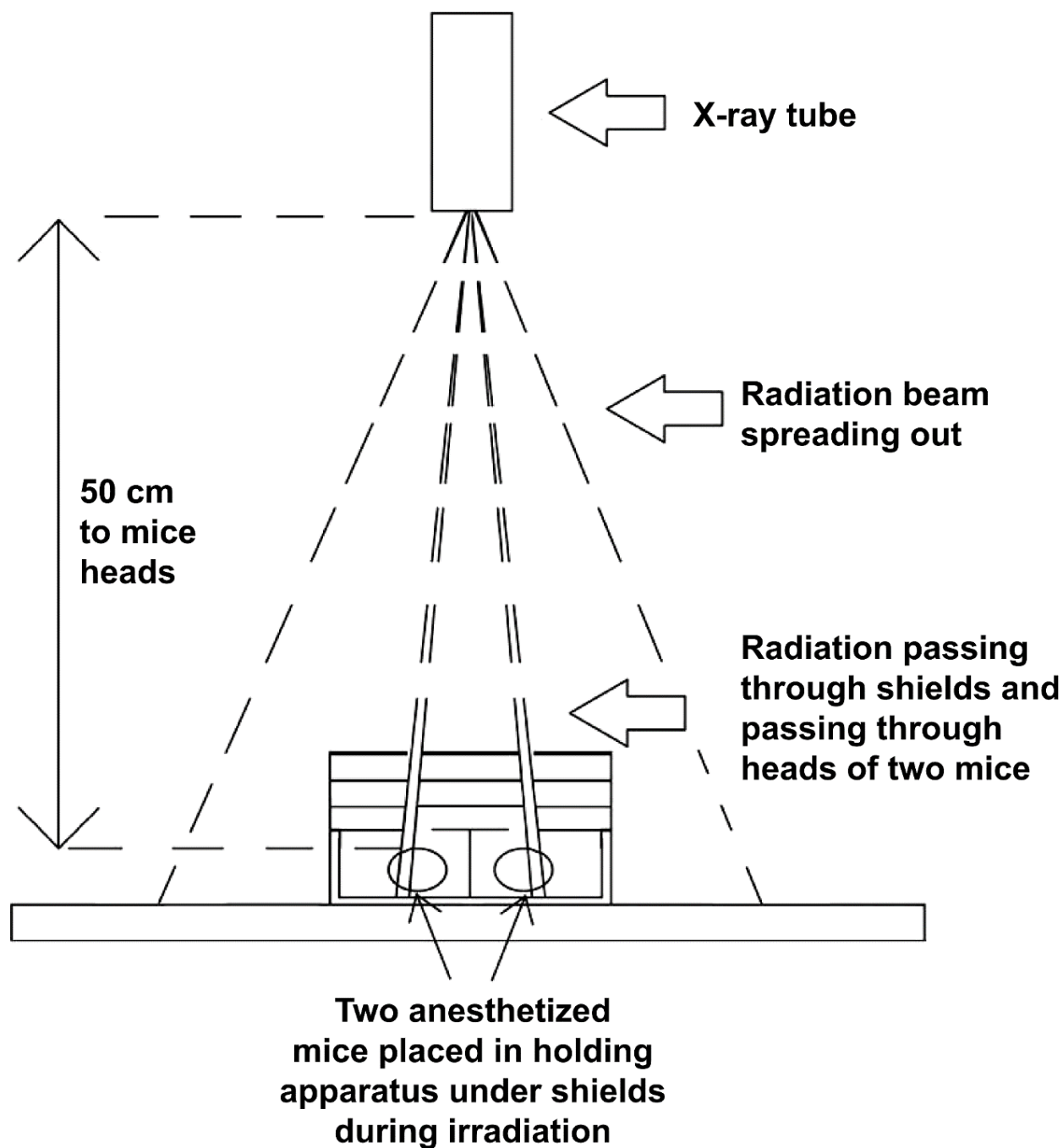


Figure 8. Treatment setup used when delivering radiation to mice from the X-RAD 320. The X-ray tube (top) produces radiation that spreads out, similar to a cone-beam effect, with increased distance from the X-Ray tube. Lead shields, which prevent exposure of critical structures within the brain, also serve to form the beam to the correct shape. At the bottom of the image, two anaesthetized mice receive radiation on opposite sides of the brain.

**PART III – INFLUENCE OF DOSE UNIFORMITY WHEN REPLICATING
A GAMMA KNIFE MOUSE MODEL OF RADIATION NECROSIS WITH
A PRECLINICAL IRRADIATOR**

Andrew J. Boria, BSE^a; Carlos J. Perez-Torres, PhD^{a,b}

^aSchool of Health Sciences, Purdue University, West Lafayette, IN, USA

^bPurdue University Center for Cancer Research, Purdue University, West Lafayette, IN, USA

Running title: Dose uniformity in necrosis mouse model

Number of figures and tables: 6

Conflicts of Interest Notification: There are no conflicts of interest to report.

Corresponding Author:

Carlos J. Perez-Torres,
550 Stadium Mall Drive,
Hampton Hall 1263A
West Lafayette, IN 47907, USA
Phone: 765-494-2974
Fax: 765-496-1377
Email: cperezto@purdue.edu

Abstract

Boria, A. J. and Perez-Torres, C. J. Influence of Dose Uniformity when Replicating a Gamma Knife Mouse Model of Radiation Necrosis with a Preclinical Irradiator. *Radiat. Res.* 191, 352–359 (2019).

A common mouse model used for studying radiation necrosis is generated with the Gamma Knife, which has a non-uniform dose distribution. The goal of this study was to determine whether the lesion growth observed in this mouse model is a function of non-uniform dose distribution and/or lesion progression. Here, a model similar to the Gamma Knife mouse model was generated; using a preclinical irradiator, mice received single-fraction doses from 50 to 100 Gy to a sub-hemispheric portion of the brain. The development of necrosis was tracked for up to 26 weeks with a 7T Bruker magnetic resonance imaging (MRI) scanner using T2 and post-contrast T1 imaging. MRI findings were validated with histology, specifically H&E staining. Single small beam 50 Gy irradiations failed to produce necrosis in a 26-week span, while doses from 60 to 100 Gy produced necrosis in a timeframe ranging from 16 weeks to 2 weeks, respectively. Postmortem histology confirmed pathological development in regions corresponding with those that showed abnormal signal on MRI. The growth of the necrotic lesion observed in this Gamma Knife model was due in part to a non-uniform dose distribution rather than to the increased severity of the lesion. Interpretation of results from the Gamma Knife model must take into consideration the potential effect of non-uniform dose distribution, particularly with regards to the timing of interventions. There are time points in this model at which pre-onset, onset and post-onset of radiation necrosis are all represented in the irradiated field.

© 2019 by Radiation Research Society

Keywords: Mouse model, radiation necrosis, radiation dose uniformity, MRI, radiation biology

Introduction

The incidence of radiation necrosis in the brain can be difficult to estimate, with rates reported between 3–63% depending on the radiation treatment and diagnosis methodology (54–59). The symptoms can be devastating and can include seizures, limb weakness, cognitive dysfunction, neural dysfunction, severe headaches, vomiting and alterations in state of consciousness (59, 88, 89). Even many of the treatment options for radiation necrosis can be problematic. For example, after corticosteroid treatment, patients experience adverse chronic side effects with a remission of the radiation necrosis (88, 90, 91). Other options, such as hyperbaric oxygen therapy, also have unwanted side effects (92) and are time consuming (53). While these treatment options may help manage the symptoms of radiation necrosis, there is no approved cure (89). As overall patient survival improves, more patients are likely to develop radiation necrosis, and the probability of occurrence warrants consideration (88, 93).

Given the limitations of patient-based studies, murine models are a common method to study disease in a more controlled fashion. The best characterized mouse model of radiation necrosis is generated via Gamma Knife irradiation (84–87). In this mouse model, the MRI-detectable radiation necrosis lesion increases in extent over time, and appears to coincide with an increase in severity (84, 85). This Gamma Knife model has been shown to successfully replicate the histological and radiological features of the disease (85) while also replicating the response to anti-VEGF therapy that has been seen in patients (84, 88, 94). The primary advantage of the Gamma Knife is that it delivers dose with several beams converging to a focal point via collimators (the smallest of which is 4 mm) to generate a high dose in an ovoid volume slightly larger than 4 mm with rapid dose drop-off past this volume (95–97). While convenient for mouse brain irradiations, the dose deposited by the Gamma Knife is not uniform, with dose usually

planned at the 50% isodose, meaning that twice the planned dose is delivered to the center of the target. Ideally, animal models should be generated with a flat prescription dose that allows better interpretation of the dose response of the tissue. A non-uniform dose distribution could potentially interfere with the interpretation of such models. A second limitation of the Gamma Knife is that it is a very specialized device found in only select hospitals, which limits the number of institutions that are able to generate this mouse model.

The goal of our study was to determine how the non-uniform dose distribution of the Gamma Knife mouse model impacts the features of said model. It is well known that for late effects of radiation, increasing dose leads to accelerated onset (98–100). The data found in the peer-reviewed literature on the Gamma Knife shows that increasing the dose at the 50% isodose line accelerated pathology (85). Prior work by Constanzo et al. (87) using a Gamma Knife rat model has already suggested that variable dose deposition leads to a delay in onset as a function of distance from the epicenter of the irradiated volume. We evaluated the generation of radiation necrosis in the mouse brain using a preclinical irradiator with a more uniform dose distribution at doses ranging from 50 to 100 Gy. As with Constanzo et al. (87), our primary hypothesis was that the growth of the radiation necrosis lesion in the Gamma Knife model was due, in part, to the non-uniform dose distribution. If our primary hypothesis is correct, for our single beam irradiation we hypothesized that increasing dose will accelerate onset and that the observed lesion size will not grow. The latter component of our hypothesis is unlikely to be perfectly met because our dose and the radioresistance within the field are not likely to be perfectly uniform. While the method of irradiation was different, we irradiated the same type of mice as in the Gamma Knife model found in the literature and evaluated the resultant injury in a similar manner. Our findings suggest that the growth of the necrotic lesion observed in this Gamma

Knife model was due in part to a non-uniform dose distribution rather than to the increased severity of the lesion.

Materials and Methods

All animal experiments were approved by the Purdue Animal Care and Use Committee. The general experimental framework included irradiation followed by MRI to track radiation necrosis lesion progression and finally postmortem validation with histology. As much as possible, these studies were designed based on the previous Gamma Knife work. To ensure consistency in replication, we have matched the biological variables previously reported in the Gamma Knife model, since mouse sex, strain and age could all potentially affect the results.

Setup and Treatment

A preclinical cabinet irradiator, X-RAD 320 (Precision X-ray, North Branford, CT), was used for single small beam irradiations of the brain of mice. EBT2 Gafchromic film (Ashland[®], Covington, KY) was used to check the dose homogeneity across the span of the 20 × 20 cm whole field, with a slight heel effect being noted (101). The heel effect was not significant in the center of the field; thus, two mice were irradiated side by side with single small beam irradiations hitting mirrored and opposite focal spots (Figure 8). To spare critical structures during irradiation of the mouse brain, one lead shield with openings 1 × 1 cm (used for placement by visualizing the entire head) and two partial-brain lead shields with openings 0.5 × 0.5 cm were used to deliver partial cerebral doses. With each shield being 1/8'' thick, shielded areas of the brain protected by the two partial-brain lead shields received ~7% of the total dose while the extracranial tissues received even less.

A filter with a half-value layer (HVL) of ~1.0 mm of copper was used to remove lower energies from the 320-keV spectrum while maintaining a high-dose rate of approximately 2 Gy/min. To measure the depth-dose dependence of our setup we measured the dose with film above and below a mouse-head-size cylindrical water phantom placed within the shielding apparatus. The dose was found to be 30% less in the bottom film for a phantom of 17 mm diameter giving a dose reduction of 1.76% per mm of depth. We used the same type of mice that were used in other published Gamma Knife model studies (84–86, 94): 8–9-week-old BALB/c (Harlan® Laboratories Inc., Indianapolis, IN). Mice were anesthetized using inhaled isoflurane two at a time while radiation doses from 50 to 100 Gy were delivered to opposite sub-hemispheric portions of the brain in the two mice, in one fraction, as shown in Figure 8. These doses were chosen to match the most common dose of 50 Gy at the 50% isodose for the Gamma Knife model (84–87).

Sixty mice were used in this study, with 51 mice (~85%) reaching their desired end point. A total of 10 mice received 50 Gy and were followed for 25 or 26 weeks (3 died early); 10 mice received 60 Gy and were followed for 24 weeks (2 died early); 11 mice received 70 Gy and were followed for 16 weeks (2 died early); 7 mice received 90 Gy and were followed for 6 weeks; 2 mice received 100 Gy and were followed for 2 weeks. In addition, several groups received 80 Gy, each comprised of 5 mice and followed for various times: for 12 weeks (2 died early), 8 weeks, 6 weeks and 4 weeks. Of note, the large rate of loss in the 50 Gy irradiated group was due to acute effects as we were optimizing our treatment setup with that group. The other mice that were lost underwent some MRI examinations but died of unexpected complications.

Magnetic Resonance Imaging (MRI)

Mice were anaesthetized prior to imaging with inhaled isoflurane. Mice were imaged at multiple time points using a Bruker BioSpec 70/30USR 7T MRI (Billerica, MA). Prior to imaging, mice received 0.2 ml intraperitoneal injection of gadobenate dimeglumine (Multi-Hance[®]; Bracco Diagnostics Inc, Princeton, NJ) diluted to a 1:10 ratio in saline. Rapid acquisition with relaxation enhancement (RARE) T2-weighted images (effective TE = 40 ms, TR = 4,000 ms, averages = 4) and MSME T1-weighted images (TE = 8 ms, TR = 500 ms, averages = 4) were acquired with 21 slices with 0.5-mm slice thickness each with the third slice centered on the separation of the olfactory bulbs and the rest of the cerebrum. The matrix size of the scans was 128×128 pixels with a field size of $15 \times 15 \text{ mm}^2$, with a corresponding resolution of 0.117 mm.

MRI Data Analysis

Radiation necrosis lesion quantification was assessed independently for each image contrast based on previous work for the Gamma Knife model reported elsewhere (94), using a semiautomatic threshold segmentation algorithm. Like the previous work performed using the Gamma Knife model, lesion was defined as regions of hyperintensity within the brain. Contrasting the previously published Gamma Knife studies, there was also a lower threshold used in addition to an upper threshold to include dark hemorrhage/necrosis regions as part of what is selected as lesion in this study. Both the upper and lower thresholds were chosen to be two standard deviations from the mean in normal mice, and the segmentation was performed using a MATLAB[®] (MathWorks[®], Natick, MA) program written in-house. Because this methodology defines the lesion as any voxel with signal intensity further than two standard deviations, even normal mice will have nonzero lesion sizes. Assuming signal intensities

precisely follow Gaussian distributions, normal brains should have a “lesion size” of ~4.6% of the total brain size, which is effectively the noise floor of our method.

Histology

After final imaging was performed, mice were euthanized, with their brains collected and left fixed in 4% paraformaldehyde for at least 24 h. The brain was processed through graded alcohols and embedded in paraffin, and 4- μ m sections were stained with hematoxylin and eosin (H&E). Sections were evaluated and photographed with an EVOS[®] XL (Life Technologies, Carlsbad, CA) digital inverted microscope. Grading of the lesions was performed based on the scale described elsewhere (85) for the Gamma Knife model. Grading was performed on a 0–3 scale with 0 representing no lesion and 3 representing a very severe lesion. However, the severity of injury present in the Gamma Knife model in general is slightly greater than in the model in this study. Grades given to mice in the previously published Gamma Knife studies generally reflect higher severity of injury than the same grade for mice in the current study. We chose to maintain the full range of 0–3 so as to better capture differences among animal groups even though that meant that the histologic grades in this study did not quantitatively match the grades in the Gamma Knife model. All of the sections were graded at the same time in a blinded fashion so as to minimize bias. The grading of the mice was compared to T2 lesion volumes, dose delivered and time since initial irradiation in the mice exposed to 80 Gy.

Statistics

Quantitative data were compiled in Prism version 7 (GraphPad Software, San Diego, CA) for the generation of plots and statistical analysis. When summary statistics are presented, data are

shown as mean \pm standard deviation. To correlate the MRI findings to histologic grade we performed Spearman correlations, given that histologic grade is not a continuous variable.

Results

The goal of our study was to determine how the non-uniform dose distribution of the Gamma Knife mouse model impacts the features of said model. We attempted to generate a model akin to the Gamma Knife mouse model generated by a 50 Gy (50% isodose) treatment using a preclinical irradiator and delivering a single 0.5×0.5 cm beam with doses between 50 and 100 Gy. Our overarching hypothesis was that the growth of the radiation necrosis lesion in the Gamma Knife model was due, in part, to the non-uniform dose distribution.

Increasing Radiation Dose Leads to Quicker Onset of Radiation Pathology

We inspected the MRI images from our irradiated mice qualitatively to establish when any abnormalities could be detected to determine the onset of radiation necrosis for each dose. Figure 9 shows that a higher radiation dose led to a shorter time to onset of lesion, which matches results already in the literature (102). Single small beam irradiations of 50 Gy using the X-RAD 320 failed to produce necrosis in a 26-week span. At 60 Gy, irradiations did not produce a consistent result, with onset of necrosis at approximately 12 weeks in one of the five mice irradiated at this dose level. Due to lack of lesion, neither are included in Figure 9. The time to onset of necrotic lesions analyzed with doses from 70 to 100 Gy ranged from 8 weeks to 2 weeks, respectively.

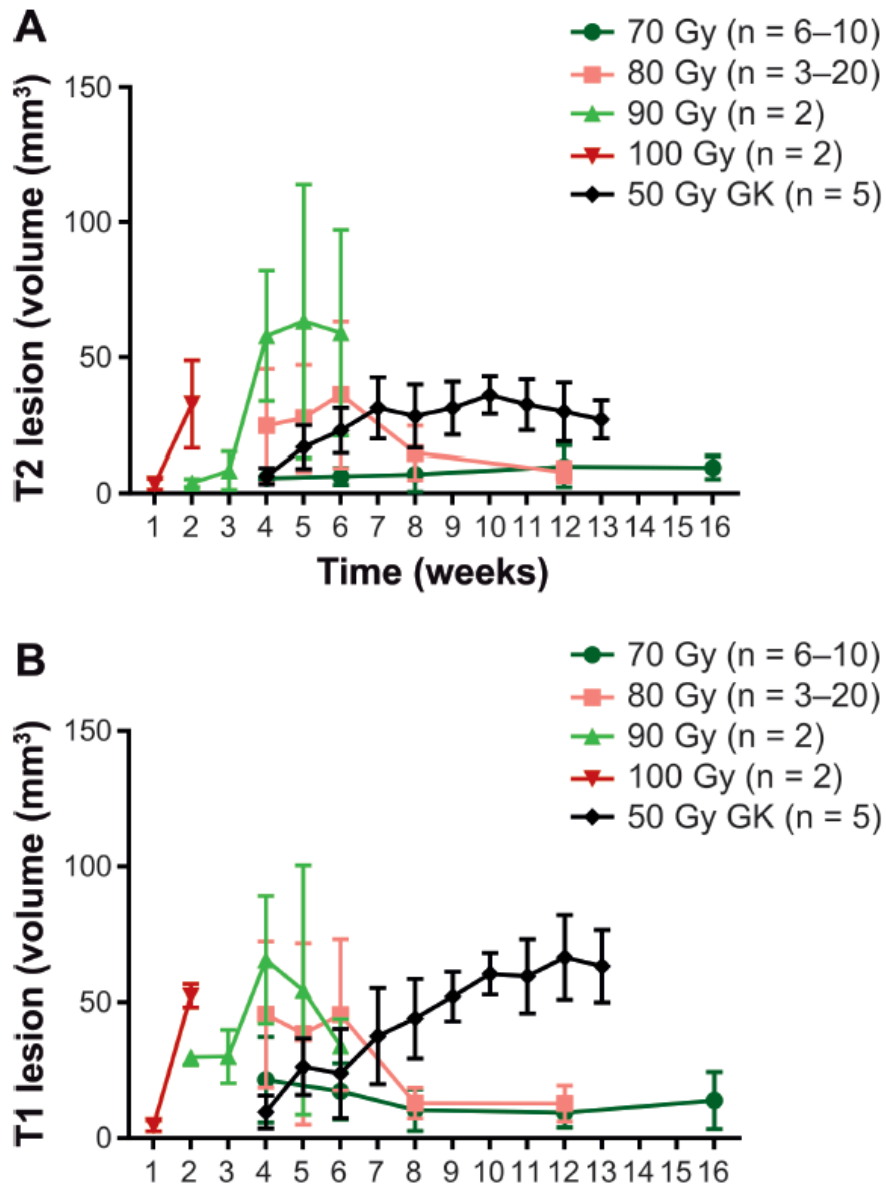


Figure 10. Lesion progression as a function of time post-irradiation and dose. Graphs show the lesion size (in mm³) over time (in weeks) for mice that received between 70 and 100 Gy for T2-weighted (panel A) or post-contrast T1-weighted (panel B) MRI images. Also included are data from the Gamma Knife model at the 50 Gy dose (50% isodose) (91). Data are presented as mean \pm standard deviation. The number of animals (n) are: for the 70 Gy group, weeks 4–8 (n = 6), week 12 (n = 10) and week 16 (n = 9); and for the 80 Gy group, week 4 (n = 20), week 5 (n = 10), week 6 (n = 15), week 8 (n = 9) and week 12 (n = 3). Note that in the Gamma Knife model the lesion size continuously increases, whereas with the X-RAD 320 our data show that this does not occur at any dose.

irradiation due to neurological side effects, with lesion development evident at two weeks post-irradiation. Mice irradiated with 90 Gy were similar but slightly delayed compared to the 100 Gy irradiated mice, and appeared to stabilize at approximately 4 weeks with large lesion volumes observed. Irradiations with 80 Gy produced lesion volumes that peaked at approximately week 6 and appeared to decrease over time. Mice irradiated with 70 Gy had lesions that were generally not as large as when higher doses were used, although the lesion was still apparent at this dose. Lesion volumes for all doses between 70 and 90 Gy (similar data for 100 Gy are not available due to the severe symptoms at this dose) generally increased with time before apparently flattening out and/or decreasing. Mice that received 50 Gy at the 50% isodose in the Gamma Knife model developed MRI-detectable radiation necrosis, which continued to grow for up to 13 weeks, as indicated on post-contrast T1 MRI images (84–86).

As an example of the MRI characteristics of the radiation necrosis lesion, Figure 11 shows the lesion development in both T2 and post-contrast T1 MRI images post-irradiation in a representative mouse that received 80 Gy. T2 lesions are generally hyperintense compared to normal brain due to increased edema, whereas hypointense spots are likely due to hemorrhage or necrotic regions. The T1 lesions are hyperintense due to leaky, damaged vasculature and subsequent gadolinium contrast agent infiltration, which is detected by MRI. The peak lesion volume is observed on both T2 and T1 at week 6, with the hyperintense lesion becoming less prominent on MRI beyond this point. Hypointense foci start to develop on T2 starting as early as week 4 and continue to expand even past week 6, with further hemorrhage/necrosis noticed at every additional time point.

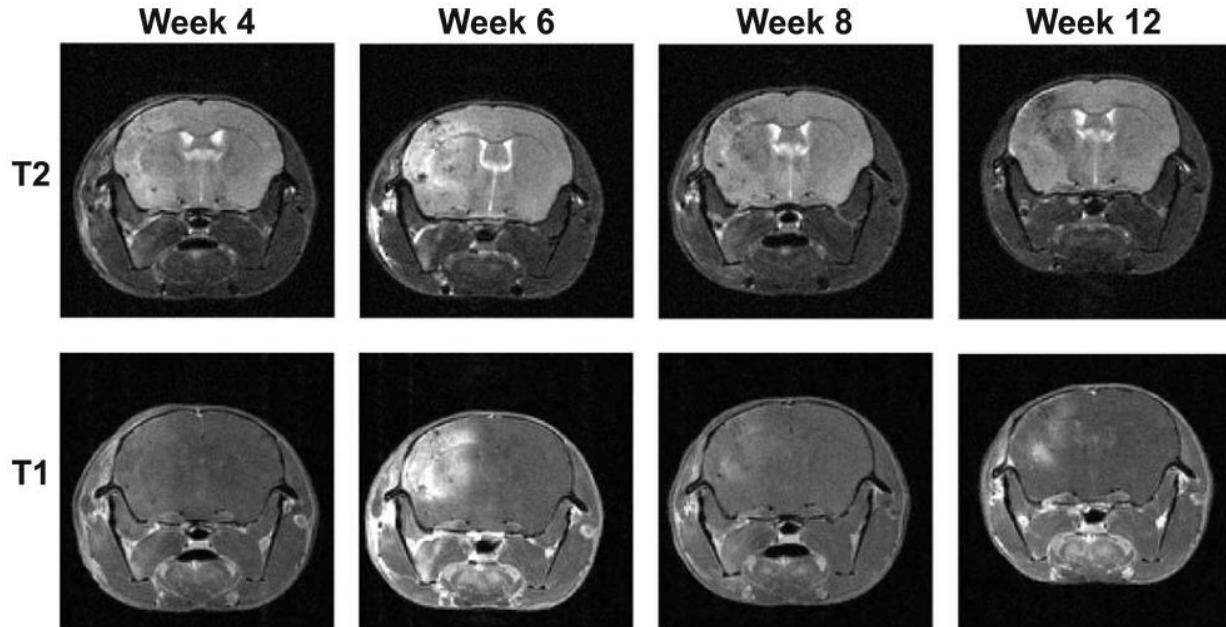


Figure 11. Representative MRI images of murine radiation necrosis over time. T2-weighted (top row) and post-contrast T1-weighted (bottom row) images of a mouse that received 80 Gy of radiation are shown from week 4 (left side) to week 12 post-irradiation (right side). Hyperintense areas on T2-weighted imaging likely reflect vasogenic edema, whereas hypointense regions likely reflect focal hemorrhage. Hyperintense regions on post-contrast T1-weighted imaging indicate a breakdown of the blood-brain barrier and leaky vasculature.

Histology Confirms the MRI Findings but Severity Does Not Correlate with Extent

Postmortem histology was performed to validate the MRI findings. Features observed in the histological sections include telangiectasia, hemorrhage, coagulation, inflammation, interstitial edema, hyalinization, immune infiltration, hippocampal necrosis and white matter damage to the contralateral side of the brain. These features are consistent with observations in both the Gamma Knife model (85, 103) and in clinical cases of radiation necrosis (104). Histologic grading was based on a scale designed for the Gamma Knife mouse model (85). Representative histology images of all grades are presented with increasing levels of severity in Figure 12 with 0

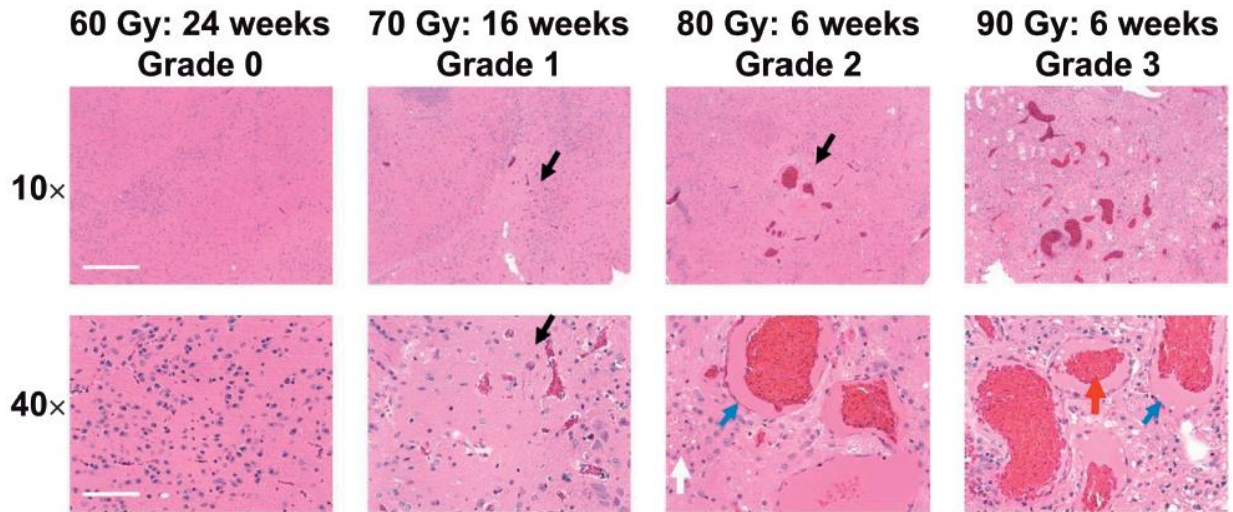


Figure 12. Representative histology images with increasing levels of severity. Brain sections graded from 0 to 3 are shown from left to right. Top row is a 10X magnification (scale bar = 0.4 mm). Bottom row shows 40X magnification of the same section (scale bar = 0.1 mm). Black arrows indicate telangiectasia, blue arrows indicate hyalinization, white arrow indicates interstitial edema and red arrow indicates hemorrhage.

representing no abnormal pathology and 3 representing extensive abnormal pathology. In the Gamma Knife literature (84–86), similar pathology is reported.

In the Gamma Knife model (84), lesion size on MRI correlates with pathology grade on histology based on the same scale that we have applied in the current work. For our data, as shown in Figure 13A, there was no correlation between T2 lesion volume and the histologic grade (Spearman $R^2 = 0.0526$; $P = 0.2230$), which differed from the Gamma Knife literature (85). Figure 13B shows there is a noticeable correlation between histologic grade and dose (Spearman $R^2 = 0.3448$; $P = 0.0016$). However, this correlation is likely highly dependent on the time points chosen for histological analysis. The histology is presented for the final imaging time point for all doses except 80 Gy, for which the 8-week time point was chosen since it had the highest severity. While imperfect, since the variable onset precludes comparing the doses at a singular time point, this correlation suggests that, as expected of deterministic effects, higher

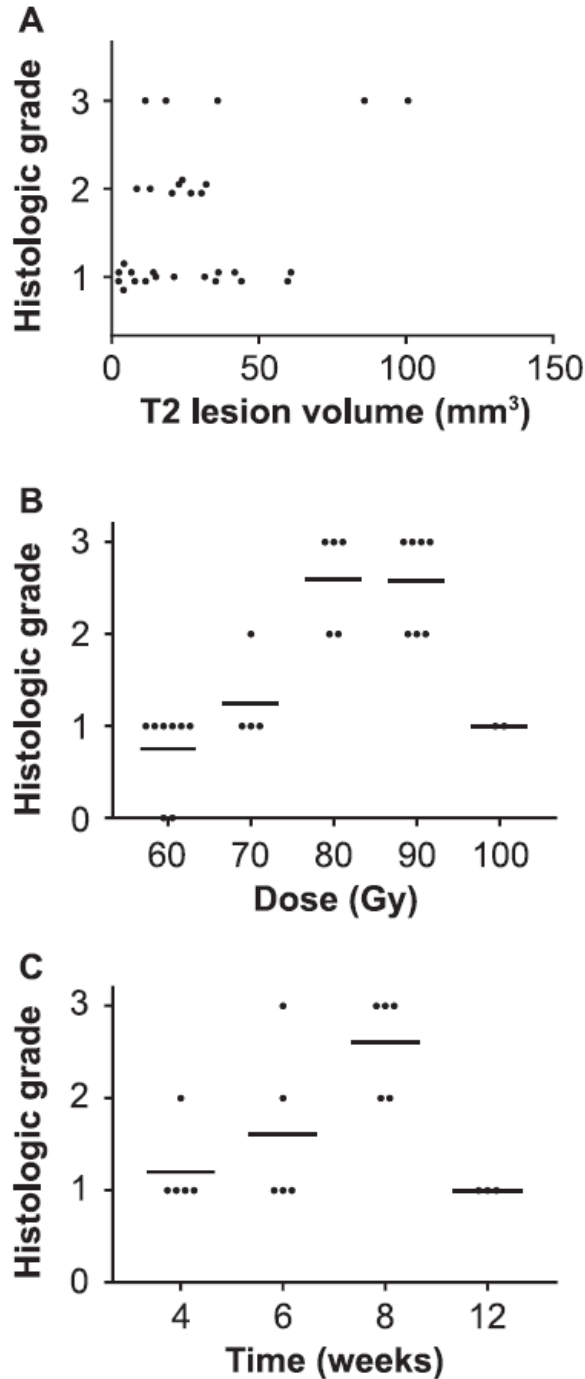


Figure 13. Comparison of histologic grade to MRI images and radiation dose. Panel A: Comparison of T2 lesion volume to the histologic grade, with each dot representing a mouse. Panel B: Comparison of histologic grade to the radiation dose, with each dot representing a mouse and horizontal bars representing the mean for that group. The time points for histology are 24 weeks for 60 Gy, 16 weeks for 70 Gy, 8 weeks for 80 Gy and 6 weeks for 60 Gy. Panel C: Comparison of histologic grade to time since irradiation in mice that received 80 Gy, with each dot representing a mouse and horizontal bars representing the mean for that group. Number of animals in each group (n) range from 2 to 18. Histological severity appears to correlate with radiation dose but not necessarily with MRI-derived lesion size.

doses lead to higher severity, which is also consistent with the larger lesion sizes for higher doses observed (Figure 10). Figure 13C shows that the histologic grade is highest at 8 weeks in 80 Gy irradiated mice and generally increases up to this point in time, after which it decreases noticeably at 12 weeks. Consistently, there was no correlation between time and histologic score for mice irradiated at 80 Gy (Spearman $R^2 = 0.0477$; $P = 0.3839$). In contrast, as shown in Figure 10, the time to maximal lesion size on MRI for the 80 Gy irradiated group was 6 weeks.

Discussion

While the Gamma Knife mouse model has proven to be quite useful, its non-uniform dose distribution presents a challenge. The goal of this study was to determine how this non-uniform dose distribution impacts the features seen in the Gamma Knife mouse model of radiation necrosis. Our overarching hypothesis was that the growth of the radiation necrosis lesion in the Gamma Knife model was due, in part, to the non-uniform dose distribution.

The time to onset of the necrotic lesions, as shown in Figure 9, accelerates with increased dose regimens, as is commonly seen in late radiation effects (98–100). In parallel, the observed lesion size does not necessarily increase in size as a function of time after onset (Figure 10 and Figure 11). These findings are different from what was observed in the Gamma Knife model, where a 50 Gy irradiation to the 50% isodose with the Gamma Knife produces a visible necrotic lesion at 4 weeks that continues grow as a function of time up to 13 weeks (84–86). This suggests that the growth of the lesion in the Gamma Knife model is at least partially due to dose distribution rather than reflecting a lesion that spreads as its severity increases.

Figure 10 and Figure 11 also show that the MRI signal of the lesion transforms over time, with the largest lesion size observed in the 80 Gy case at approximately 6 weeks, with the size of lesion apparently decreasing at 8 and 12 weeks. There is some increase in lesion size early on

which would contradict our hypothesis. As the T1 lesion is hyperintense due to leaky, damaged vasculature and subsequent gadolinium contrast agent infiltration, the decrease in T1 signal suggests the vasculature permeability is no longer present. Similarly, a reduction in the lesion volume as demonstrated by increased hyperintensity in T2, due primarily to vasogenic edema, would also be consistent with a cessation of vascular permeability. Seen most prominently in T2 images in Figure 11 is the development of hemorrhage/necrosis, which appears in this murine model to be a feature that occurs generally after the start of visible edema. However, the development of hemorrhage/necrosis as early as 4 weeks, as observed for 80 Gy irradiations, does not necessarily correlate with other similar studies, e.g., Ngen et al. (105), who also irradiating with 80 Gy, but no hemorrhage was reported up to 10 weeks. Hemorrhage was observed in the Gamma Knife model, however, with the highest level also being observed at 13 weeks (84), which is more similar to the current study.

Histologic grade and dose appear to have a linear relationship, as shown in Figure 13B, with Figure 12 visually showing representative cases. However, that correlation may be a function of the time points chosen for histological evaluation for each dose. T2 lesion volume and histologic grade do not appear to have a correlation such as that shown in Figure 13A, which contrasts the Gamma Knife model having such a correlation. A potential cause is the late-term decrease in MRI-visible lesion as seen with 80 Gy mice after 6 weeks. It is important to note that our histologic score has limitations. Namely, the score heavily weights vascular injury and apparent lesion extent as the primary drivers of the score. In their extensive histological analysis, Constanzo et al. (87) describe three tissue types within the lesion that likely occur sequentially. Type I is permeable neovascularization without necrosis; type II is necrosis with abnormal blood vessels; and type III applies to nonperfused necrotic tissues. Our histologic score likely

undervalues type III tissues. An increase in type III tissues would also explain the decrease in lesion volume on MRI, particularly as measured on post-contrast T1. A lesion becoming less discernable on MRI thus does not necessarily mean that the severity of the lesion has lessened. This is noticeable in Figure 13C, where the histologic grade peaks at week 8 while at the same time MRI lesion volumes are decreasing at this point. Further work may be necessary to analyze the state of late-term lesions. Other MRI modalities are known to be more sensitive and accurate to the changes over time in the necrosis lesion (86, 87, 106) which may better describe the changes occurring at these later time points.

There are certain limitations when comparing our work to the Gamma Knife model literature. While we attempted to replicate as many of the materials and methods from the Gamma Knife literature, the treatment plans and treatment volumes are not the same. Additionally, dose uniformity for the X-RAD 320 does not have the same quality standards as those required for a clinical device. When adding the potential additional effect to the skull for these low-energy photons, it is likely that we are overestimating the dose to brain of mice in the current study. Finally, our data are likely more imprecise than the work in the Gamma Knife studies because our mouse placement is likely not as reproducible.

Even when these limitations are considered, the main conclusion remains the same: by mixing multiple radiation doses, lesion growth in the Gamma Knife model is driven by a mix of its variable dose distribution and true progression. While the doses in this work might be overestimated, it is likely to be a consistent factor across all doses in our work. Our data then clearly show that there is a variable onset to lesion when mouse brain is irradiated within the 50–100 Gy dose range, even if we might not have perfect dose uniformity ourselves. Studies with the goal of treating for radiation necrosis could particularly be affected in the Gamma Knife

model and should be performed once the lesion has stopped growing. Otherwise, those drugs would be acting as treatments (post-onset) and mitigators (pre-onset) at the same time within that mouse model.

Acknowledgements

We gratefully acknowledge the Purdue Small Animal MRI core facility and Purdue Histology Research Laboratory core facility where this work was performed. We also thank Dr. Chang-Deng Hu for providing access to the X-RAD 320.

Received: October 16, 2018; accepted: January 18, 2019; published online: February 19, 2019

**PART IV – MINIMAL DIFFERENCE BETWEEN FRACTIONATED AND
SINGLE-FRACTION EXPOSURE IN A MURINE MODEL OF
RADIATION NECROSIS**

Andrew J. Boria, BSE^a (aboria@purdue.edu); Carlos J. Perez-Torres, PhD^{a,b,1}
(cperezto@purdue.edu)

^aSchool of Health Sciences, Purdue University, West Lafayette, IN, USA

^bPurdue University Center for Cancer Research, Purdue University, West Lafayette, IN, USA

¹Corresponding Author.

Running title: Fractionation in necrosis mouse model

Number of figures and tables: 3

Address for correspondence: School of Health Sciences, Purdue University, 550 Stadium Mall
Drive, Hampton Hall 1263A, West Lafayette, IN 47907, USA.

Abstract

Boria, A. J. and Perez-Torres, C. J. Minimal difference between fractionated and single-fraction exposure in a murine model of radiation necrosis. *Radiat Oncol.* 14, 144 (2019).

Purpose: Despite the success of fractionation in clinical practice to spare healthy tissue, it remains common for mouse models used to study the efficacy of radiation therapy to use minimal or no fractionation. The goal of our study was to create a fractionated mouse model of radiation necrosis that we could compare to our single fraction model.

Methods: Precision X-Ray's X-RAD 320 cabinet irradiator was used to irradiate the cerebrum of mice with four different fractionation schemes, while a 7 T Bruker magnetic resonance imaging (MRI) scanner using T2 and post-contrast T1 imaging was used to track the development of radiation necrosis over the span of six weeks.

Results: All four fractionation schemes with single fraction equivalent doses (SFED) less than 50 Gy for the commonly accepted alpha/beta ratio (α/β) value of 2–3 Gy produced radiation necrosis comparable to what would be achieved with single fraction doses of 80 and 90 Gy. This is surprising when previous work using single fractions of 50 Gy produced no visible radiation necrosis, with the results of this study showing fractionation not sparing brain tissue as much as expected.

Conclusion: Further interpretation of these results must take into consideration other studies which have shown a lack of sparing when fractionation has been incorporated, as well as consider factors such as the use of large doses per fraction, the time between fractions, and the limitations of using a murine model to analyze the human condition.

© The Author(s)

Keywords: Fractionation, Mouse model, MRI, Radiation biology, Radiation necrosis

Introduction

Radiation therapy is essential to cancer treatment, with approximately 50% of cancer patients receiving radiation therapy and radiation contributing toward 40% of the curative treatments of the disease (34). Fractionated radiation therapy is the most prominent technique for treating cancer with radiation (35) due primarily to fractionation allowing for the selective sparing of healthy tissue (33, 34). Fractionation thus serves clinically to reduce the complications attributed to radiation therapy (107–110).

Though fractionation is the established approach clinically, it remains common in preclinical studies to perform experiments and generate animal models with high single fraction doses (84–87, 111). This unfractionated approach has practical advantages such as a shorter time commitment and avoiding potential confounds due to the potentially limited reproducibility of positioning for focal treatments. Even so, ideally animal models of radiation-induced injury should be performed with fractionated regimes to ensure that the radiation exposure is as human-like as possible.

We have recently published a mouse model of radiation necrosis generated with a large single fraction treatment (112). Based on the logic above, our goal was to create a fractionated mouse model in order to treat mice in a way more similar to how humans are treated with radiation. Our hypothesis was that fractionation would provide a noticeable level of sparing to healthy tissue as seen in patients. However, the level of sparing was found to be minimal, with fractionation schemes predicted not to cause radiation necrosis based on our previous findings (112) instead causing radiation necrosis almost as severe as observed with single fraction doses of equal total dose.

Materials and Methods

All animal experiments were approved by the Purdue Animal Care and Use Committee. The general experimental framework included irradiation followed by MRI to track radiation necrosis lesion progression and finally post-mortem validation with histology.

Setup and treatment

Irradiation was performed as previously described (*112*) so that our fractionated treatments are comparable to the single fraction data from that publication. Briefly, an X-RAD 320 (Precision X Ray, North Branford, CT) preclinical cabinet irradiator was used to deliver partial cerebrum doses to mice via a field 0.5 cm by 0.5 cm such that a single hemisphere was irradiated at a dose rate of about 2 Gy per minute. Female 8–9 week old BALB/c (Harlan, Indianapolis, IN) were irradiated once a day Monday through Friday as is usually done in the clinic.

Fractionation

Four different radiation fractionation schemes were used: 5 fractions of 20 Gy, 10 fractions of 10 Gy, 5 fractions of 18 Gy, and 10 fractions of 9 Gy. We chose not to do more than 10 fractions over two weeks because in our previous work onset of pathology occurred at 2 or 3 weeks for 100 and 90 Gy in a single fraction respectively (*112*). We were concerned that further protraction might lead to overlap of treatment and lesion onset. Based on the linear-quadratic model, the biologically effective dose (BED) and single fraction equivalent dose (SFED) were calculated for all four schemes and are included in Table 1 based off the commonly assumed alpha/beta ratio (α/β) for early and late responding tissue (*113*). For both equations, n is the fraction number, d is the dose per fraction in Gy, and α/β in Gy is from the linear-quadratic model.

Table 2. BED and SFED calculated for three hypothetical α/β ratios for the four dose regimes used.

Late Effects/Cerebrum $\alpha/\beta=2$ Gy	n	d (Gy)	BED (Gy)	SFED (Gy)
	5	20	1100	45.91
	10	10	600	33.66
	5	18	900	41.44
	10	9	495	30.48
Late Effects/Cerebrum $\alpha/\beta=3$ Gy	n	d (Gy)	BED (Gy)	SFED (Gy)
	5	20	766.7	46.48
	10	10	433.3	34.59
	5	18	630	42.00
	10	9	360	31.40
Early Effects/Tumor $\alpha/\beta=10$ Gy	n	d (Gy)	BED (Gy)	SFED (Gy)
	5	20	300	50
	10	10	200	40
	5	18	252	45.45
	10	9	171	36.65

The fraction number (n), dose per fraction (d), biologically effective dose (BED), and single fraction equivalent dose (SFED) are all included.

The BED is calculated as given in Fowler (113) as

$$BED = (nd) \times \left(1 + \frac{d}{\alpha/\beta}\right). \quad (1)$$

The single fraction equivalent dose (SFED) is obtained from the BED by substituting $d = SFED$ and $n = 1$, and then solving for SFED giving the following equation:

$$SFED = \frac{-1 + \sqrt{1^2 + 4 \frac{BED}{\alpha/\beta}}}{\frac{2}{\alpha/\beta}}. \quad (2)$$

Magnetic Resonance Imaging (MRI)

Inhaled isoflurane was used to anaesthetize mice prior to imaging. Mice received an intraperitoneal injection of 0.2 mL of Multihance (gadobenate dimeglumine; Bracco Diagnostics Inc., Princeton, NJ) prior to imaging diluted to a 1:10 ratio in saline. A Bruker BioSpec 70/30USR 7 T MRI (Billerica, MA) was used to image mice at multiple timepoints up to a final timepoint of six weeks. RARE T2-weighted images (Effective TE = 40 ms, TR = 4000 ms, Averages = 4) and MSME T1-weighted images (TE = 8 ms, TR = 500 ms, Averages = 4) were acquired. Twenty one slices with a 0.5 mm slice thickness were obtained for each scan type with the 3rd slice of both set of scans centered on where the olfactory bulbs and the rest of the cerebrum were separated. The matrix size of the scans was 128 pixels by 128 pixels with a field size of 15 by 15mm², with a corresponding resolution of ~0.117 mm.

MRI Data Analysis

Radiation necrosis lesion quantification was assessed using a semi-automatic threshold segmentation algorithm as we have previously performed in this model (112). Lesion is defined as regions of hyperintensity and hypointensity within the brain in this study with T1 and T2 images being analyzed independently. Both the upper and lower thresholds were chosen to be two standard deviations from the mean in normal mice. Brain segmentation and defining of lesion was carried out with a MATLAB (Math-Works, Natick, MA) program written in-house. Once the algorithm determined which voxels comprised the lesion, the lesion volumes is calculated by multiplying the total number of voxels by the unit volume for a voxel based on the scan geometry. In our scans, each voxel has a unit volume of roughly 0.007 mm^3 .

Statistics

Quantitative data were compiled in Prism 8 (GraphPad Software, San Diego, CA) for the generation of plots and statistical analysis. When summary statistics are presented, data are shown as mean \pm standard deviation. Two-Way ANOVA with a Tukey post-hoc test was used to compare the lesion volumes as a function of radiation scheme and time for T1 and T2 images independently.

Histology

Mice were euthanized after final imaging with their brains collected and left fixed in 4% paraformaldehyde with graded alcohols being used for processing. Mouse brains were embedded in paraffin. Hematoxylin and eosin (H&E) staining was used on four micrometer sections of each mouse brain. An Evos XL (Life Technologies, Carlsbad, CA) digital inverted microscope was used to evaluate and photograph brain sections.

Results

The original purpose of our study was to create a fractionated mouse model of radiation necrosis that we could compare to our single fraction model. Mice were irradiated with four fractionation schemes and tracked up to 6 weeks with lesion volumes being measured. The lesion volumes measured were compared to what is generated with the same irradiation setup but single fraction doses (112). Lesion development is observable on MRI in mice irradiated with all four fractionation schemes that is similar to what is observed in single fraction irradiations of 80 Gy or higher as is seen in Figure 14 (Panels A and B). The two 100 Gy total fractionation schemes of 5 fractions of 20 Gy and 10 fractions of 10 Gy had lesion volumes most comparable to what is observed in single fraction irradiations of 90 Gy, while the two 90 Gy total fractionation schemes of 5 fractions of 18 Gy and 10 fractions of 9 Gy had lesion volumes most comparable to what is observed in single fraction irradiations of 80 Gy. Using a Two-Way ANOVA, there was no significant difference between 5 fractions of 20 Gy and 1 fraction of 90 Gy, 5 fractions of 18 Gy and 1 fraction of 80 Gy, and 10 fractions of 9 Gy and 1 fraction of 80 Gy at either 4 or 6 weeks post-irradiation on both T2 and T1. 10 fractions of 10 Gy and 1 fraction of 90 Gy showed a significant difference at 4 weeks post-irradiation on T2 (Tukey P = 0.0282) and T1 (Tukey P = 0.0492), but did not show a significant difference 6 weeks post-irradiation. Similarly, quantification of the radiation necrosis lesion on based on hematoxylin and eosin staining found no differences between the irradiation schemes at 6 weeks post-irradiation (Figure 14 Panel C). A one-way ordinary ANOVA of the Histology Grade vs Dose (Gy) data found that the most significant Tukey post-hoc adjusted p value was 0.0617 between 20 Gy * 5 vs. 80 Gy, showing a lack of statistical significance in this data.

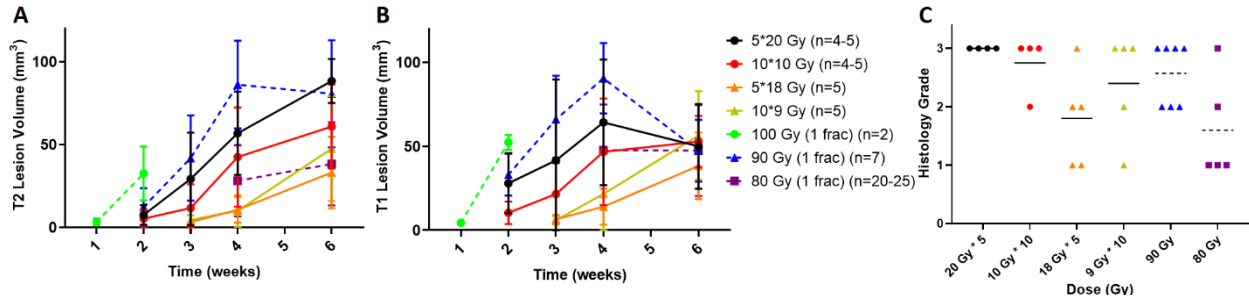


Figure 14. Lesion progression as a function of time post-irradiation. The figure shows the lesion size (in mm³) over time (in weeks) for mice that received multiple fractionation regimens as well as single fraction doses between 80 and 100 Gy for T2-Weighted (Panel A) and post-contrast T1-weighted (Panel B) MRI images as well as histological scores at 6 weeks post-irradiation (Panel C). The data is presented as mean \pm standard deviation for lesion progression in Panels A and B with mean values present as bars in Panel C. The number of animals in each group (n) ranges from 2 to 25. Notice that the fractionated schemes' lesion volumes are comparable to those of the three single fraction regimens against the expectations of the SFED seen in Table 2. Also, the post-radiation side effects for single fraction 100 Gy irradiations were severe enough that mice needed to be sacrificed at 2 weeks with data not available past this point. Histological scores for 100 Gy are not in Panel C since post-irradiation side effects required sacrificing these mice early at 2 weeks.

Furthermore, brain swelling is observable in the former two fractionation schemes but mostly absent in the latter two fractionation schemes as observed in Figure 15 with measurable damage caused by radiation on both MRI and Hematoxylin and eosin (H&E) being generally greater in the former than the latter. The results thus show that fractionation is less effective at controlling lesion development than expected with total dose being an important predictive factor of lesion development.

Discussion

The purpose of this study was to create a fractionated mouse model of radiation necrosis that could be compared to our single-fraction model. All four fractionation schemes had single fraction equivalent doses less than 50 Gy. Though our single fraction irradiations of 50 Gy did not produce radiation necrosis within 26 weeks (112), all fractionated regimes led

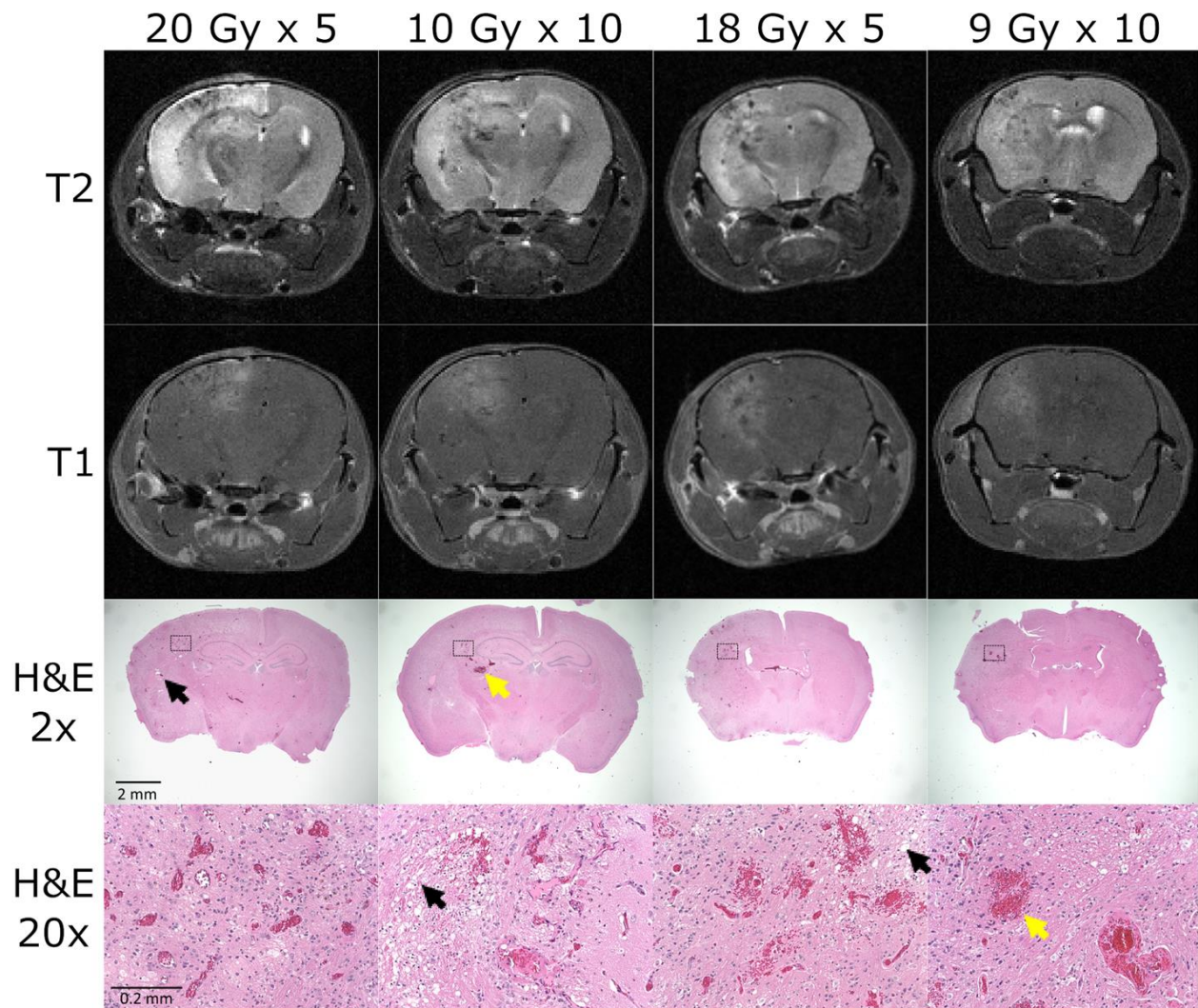


Figure 15. Representative MRI and histology images of murine radiation necrosis. T2-weighted (1st row), post-contrast T1-weighted (2nd row), and H&E images with a magnification of 2 and 20 respectively (3rd and 4th row) are presented for all four fractionation schemes: 5 fractions of 20 Gy, 10 fractions of 10 Gy, 5 fractions of 18 Gy, and 10 fractions of 9 Gy. The 3rd and 4th H&E images have black scales bars equal to 2mm and 0.2 mm respectively. Areas of radiation injury on MRI (left hemisphere) correspond to visible pathology such as interstitial edema (black arrows) and hemorrhage (yellow arrows) on H&E images.

to measurable radiation necrosis on MRI and histology. The two 100 Gy total fractionation schemes had lesion volumes most similar to single fraction irradiations of 90 Gy, while the two 90 Gy total fractionation schemes were most similar to single fraction irradiations of 80 Gy.

The lack of sparing expected by fractionation observed is surprising, as this has been well evidenced in most tissues in laboratory animals leading to fractionation as the most common way we perform radiotherapy (*114–117*). However, the sparing effects of radiation being less than anticipated in the rodent brain is not a new phenomenon. A prior report on a murine model of radiation necrosis (*85*) showed no difference when comparing a 60 Gy (50% isodose) treatment given in both 1 and 3 fractions. Similar results have been found when comparing fractionated to unfractionated regimes in a rat model of cognitive impairment (*118*) with single-fraction doses ranging from 11 to 17 Gy.

One potential explanation for the lack of sparing is the large fraction sizes and total dose in our study. However, various hypo-fractionated schemes are reported for late-responding tissues with similar fraction sizes to the low end of what we used which generally conform to the BED (*110, 119, 120*). Another potential reason may be that we did not wait long enough in between delivering fractions. A prior report (*121*) gives a repair halftime for radiation necrosis to be 38.1 (6.9–76) hours based on human data. Thus, irradiating every other day instead of every day may result in additional sparing of damage.

An important limitation of our work is the rodent brain itself. The differences in levels of brain folding and white to grey matter composition between rodents and humans complicates the interpretations of any findings. Rodent models of radiation induced brain injury may not behave in a manner consistent with human disease. A clear example of this is

the large doses that are needed to generate radiation necrosis in rodents (112). We have also seen this in the past with models of radiation induced cognitive impairment not replicating the MRI deficits seen in humans (122). Fractionation may not be as important a parameter in our murine model compared to parameters such as total dose, but we believe this is much more likely a feature of rodent brain irradiation models that is unlikely to be reflected in human patients.

Abbreviations

BED: Biologically effective dose; H&E: Hematoxylin and eosin; MRI: Magnetic resonance imaging; SFED: Single fraction equivalent dose; α/β : alpha/beta ratio

Acknowledgements

We would like to thank the following Purdue core facilities where the work was performed: Purdue Small Animal MRI facility and Histology Research Lab. We also wish to thank Dr. Chang-Deng Hu for providing access to the X-RAD 320.

Authors' contributions

AJB helped design and performed the experiments, analyzed the data, and wrote the manuscript. CJPT designed experiments and wrote and edited the manuscript. Both authors read and approved the final manuscript.

Funding

There are no funding sources to report for this study.

Availability of data and materials

The datasets used and/or analyzed during the current study are available from the corresponding author on reasonable request.

Ethics approval

All animal experiments were approved by the Purdue Animal Care and Use Committee.

Consent for publication

Not applicable

Competing interests

The authors declare that they have no competing interests.

Received: 11 March 2019 Accepted: 7 August 2019

Published online: 13 August 2019

PART V – IMPACT OF MOUSE STRAIN AND SEX WHEN MODELING RADIATION NECROSIS

Andrew J. Boria, BSE^a; Carlos J. Perez-Torres, PhD^{a,b,1}

^aSchool of Health Sciences, Purdue University, West Lafayette, IN, USA

^bPurdue University Center for Cancer Research, Purdue University, West Lafayette, IN, USA

Running title: Effect of strain and sex on necrosis

Number of figures and tables: 4

¹Address for correspondence: School of Health Sciences, Purdue University, 550 Stadium Mall Drive, Hampton Hall 1263A, West Lafayette, IN 47907, USA; cperezto@purdue.edu

Abstract

Background: Murine models are among the most common type of preclinical animal models used to study the human condition, but a wide selection of different mice is currently in use with these differences potentially compromising study results and impairing the ability to reconcile interstudy results. Our goal was to determine how the strain and sex of the mice selection would affect the development of radiation necrosis in our murine model of radiation-induced cerebral necrosis.

Methods: We generated this model by using a preclinical irradiator to irradiate a sub-hemispheric portion of the brain of mice with single-fraction doses of 80 Gy. Eight possible combinations of mice made up of two different strains with two substrains each (BALB/cN, BALB/cJ, C57BL/6N, and C57BL/6J) and both sexes were irradiated in this study. Radiation necrosis development was tracked up to eight weeks with a 7T Bruker MRI utilizing T2-weighted and post-contrast T1-weighted imaging. MRI results were compared to and validated with the use of histology which utilized a scale from 0-3 in ascending order of damage.

Results: Both time post-irradiation and strain (BALB/c vs C57BL/6) were significant factors affecting radiation necrosis development. Sex was in general not a statistically significant parameter in terms of radiation necrosis development.

Conclusion: Mouse strain thus need to be considered when evaluating the results of necrosis models. However, sex does not appear to be a variable needing major consideration.

Keywords: Radiation necrosis, Sex as a biological variable, Mouse Strain, animal models

Background

Mouse models of disease remain a powerful tool in biomedical research, with similar models being used across multiple labs spanning multiple countries. Ideally, these mouse models should produce results that are as close to identical as possible across all locations. However, for this to happen, the parameters used in each of the models should be as consistent as possible. That being said, some parameters will affect each model more than others. We are interested in modeling cerebral radiation necrosis, a consequence of brain irradiation for cancer that affects 3 to 23% of patients (*123, 124*). Previously, we have shown how changes in the radiation delivery parameters, including a comparison of two radiation delivery devices, can affect the modeling of radiation necrosis (RN) in the mouse (*112, 125*).

Given that this is a model of a radiation-induced pathology, the natural inclination would be to focus primarily on replication of the radiation delivery parameters to ensure the model is reproducible. However, biological parameters can also influence the ability to properly reproduce the model. There are examples in the literature of brain irradiations being modeled in BALB/c (*112, 125*) and C57BL/6 (*126, 127*), which is not surprising as they are the two most common “normal” mouse strains. Ironically, for the cited reports above, the BALB/c studies were done in females while the C57BL/6 studies were done in males which is another biological factor that could influence the response of the model. We know from studies on radiation lethality that BALB/c mice should be more sensitive to radiation than C57BL/6 (*128, 129*).

The goal of this study was to determine the effect mouse strain and sex have in reference to our previously established model of RN (*112, 125*). As both the BALB/c and C57BL/6 strains have existed for over 100 years, and genetic drift is known to have occurred (*130, 131*), we further decided to include two different vendors for each strain encompassing the N and J

substrains for each strain. Radiation parameters were kept constant across all mice and consistent with our prior work. Consistent with the prior reports on radiosensitivity based on lethality, we found that BALB/c mice are more sensitive than C57BL/6 mice leading to accelerated onset of the model. However, sex was not found to affect the results of the model.

Methods

All animal experiments were approved by the Purdue Animal Care and Use Committee. Irradiation of mice was followed by MRI at multiple timepoints to track radiation necrosis lesion progression followed by post-mortem validation with histology after the final timepoint.

Setup and Treatment

In depth details of our irradiation setup can be found in our prior publication (*112*). Briefly, an X-Rad 320 (Precision X Ray, North Branford, CT) pre-clinical cabinet irradiator was used to deliver partial cerebrum doses to mice to a 0.5 cm by 0.5 cm field at a dose rate of about 2 Gy per minute. All mice received 80 Gy in a single treatment under isoflurane anesthesia.

Mouse strain and numbers

8-9-week-old mice were sourced as follows: BALB/cN (Harlan Laboratories Inc., Indianapolis, IN), BALB/cJ (Jackson Laboratory, Bar Harbor, ME), C57BL/6N (Charles River Laboratories Inc., Wilmington, MA), and C57BL/6J (Jackson Laboratory, Bar Harbor, ME). 95 total mice were used in this study: 15 female BALB/cN mice; 10 male BALB/cN mice; 15 female BALB/cJ mice; 10 male BALB/cJ mice; 15 female C57BL/6N mice; 10 male C57BL/6N mice; 10 female C57BL/6J mice; and 10 male C57BL/6J mice. Of these, 40 mice (5 of each of the 8

possible combinations of sex and substrain) were followed for 4-weeks, and 55 mice were followed for 8-weeks (2 died early).

Magnetic Resonance Imaging (MRI)

Prior to imaging, inhaled isoflurane was used to anaesthetize mice, and mice were given an intraperitoneal injection of 0.2 mL of Multihance (gadobenate dimeglumine; Bracco Diagnostics Inc, Princeton, NJ) diluted to a 1:10 ratio in saline. Imaging was carried out using a Bruker BioSpec 70/30USR 7T MRI (Billerica, MA) which was used to image mice at timepoints of 4, 6, and 8 weeks. Both RARE T2-weighted images (Effective TE=40 ms, TR=4000 ms, Averages=4) and MSME T1-weighted images (TE=8 ms, TR=500 ms, Averages=4) were acquired. Twenty-one slices with a 0.5 mm slice thickness were obtained for each scan type with the 3rd slice of both set of scans centered on where the olfactory bulbs and the rest of the cerebrum were separated. The matrix size of the scans was 128 pixels by 128 pixels with a field size of 15 by 15 mm², with a corresponding resolution of ~0.117 mm.

MRI Data Analysis

Quantification of the radiation necrosis lesion was carried out using a semi-automatic threshold segmentation algorithm as we have previously described (112). The lesion was defined as the areas of both hyperintensity and hypointensity for both T2 and T1 imaging. Both the upper and lower thresholds for determining what constitutes lesion were chosen to be two standard deviations from the mean that is present in normal mice. Segmentation of the brain and definition of lesion volumes was performed with a MATLAB (MathWorks[®], Natick, MA) program written in-house.

Histology

Mice were euthanized after final imaging with their brains collected. Hematoxylin and eosin (H&E) sections were generated for each mouse brain and evaluated with an Evos XL (Life Technologies, Carlsbad, CA) digital inverted microscope. Histological slices were graded on a 0-3 scale where 0 represents no lesion and 3 represents a severe lesion as we have previously performed in this model (*112, 125*). All of the sections were graded at the same time in a blinded fashion so as to minimize bias.

Statistics

All analysis testing for statistical significance was performed in SPSS[®] Statistics (IBM, Armonk, NY). A linear mixed model was used for T2 and T1 lesion volumes while an ordinal regression model was used for the histological grades to test for statistical significance as a function of time (number of weeks post-irradiation), sex, and strain/substrain. In the case of the MRI data, the model controls for repeated measurements and we additionally performed Sidak adjusted pairwise comparisons. All SPSS output files are included in Appendix A-C.

Results

The goal of this study was to determine the effect of mouse strain and sex in reference to our previously established model of RN. We analyzed all mice from four to eight weeks post-irradiation as we had previously shown that the former is the onset of lesion and the latter is the peak lesion size on BALB/cN females (*112, 125*). We evaluated the induction of radiation necrosis using three metrics: T1-weighted MRI, T2-weighted MRI and a histology score. We had a total of 95 mice where we varied the mouse strain (including substrain), and sex which

were evaluated at multiple time points (4, 6 and 8 weeks for MRI and 4 and 8 weeks for histology).

In general, time post-irradiation and mouse strain significantly affect radiation necrosis modeling, while the effect of sex is minimal

Given the number of variables, we decided to use regression analyses to determine the effect strain, sex and time after irradiation had on the development of radiation necrosis. We evaluated each outcome metric independently. Since the MRI measurements are continuous and appear normally-distributed, we used a multi-linear regression. However, the histology score is an ordinal measurement, so an ordinal model was used in that case. The results of the fixed effects tests are shown in Table 3 for all three outcome variables. Time after radiation, as expected, was found to be a significant factor for all three outcomes ($P \leq 0.002$). Mouse strain was significant on T2-weighted MRI ($P = 0.000$) but not T1-weighted MRI or histology. However, the interaction term between strain and time was significant for all three measurements ($P \leq 0.038$) suggesting that strain may be playing a role in radiation necrosis development. Sex by itself was not significant for any measurement ($P \geq 0.446$) with only the sex and strain interaction term being significant and only for T1-weighted MRI ($P = 0.008$).

There are differences between C57BL/6 and BALB/c mice but not between the N and J substrains of each strain.

Within each model, we further performed pairwise comparisons for the MRI data to identify further differences nested within each dependent variable. The statistical results of the pairwise comparisons are shown in Table 4. When looking within the effect of time after irradiation, pooling all the strains and both sexes, week 4 after irradiation is consistently significant versus weeks 6 and 8 ($P \leq 0.016$). However, there is no statistical significance between weeks 6 and 8

Table 3. Type III tests of fixed effects results for T2- and T1-weighted MRI lesion volumes from a linear mixed model and for histological grade from an ordinal model.

Parameter	<i>T2-Weighted MRI</i>			<i>T1-Weighted MRI</i>			<i>Histology</i>		
	df	F	Sig.	df	F	Sig.	df	χ^2	Sig.
Strain	3	16.194	0.000	3	1.388	0.252	3	2.206	0.531
Sex	1	0.005	0.945	1	0.586	0.446	1	0.038	0.845
Time	2	15.015	0.000	2	6.569	0.002	1	32.380	0.000
Sex * Week	2	0.358	0.700	2	0.003	0.997	1	1.193	0.275
Strain * Sex	3	0.668	0.574	3	4.150	0.008	3	3.816	0.282
Strain * Time	6	2.310	0.038	6	2.751	0.015	3	10.650	0.014

The parameters tested, parameter degrees of freedom (df), F statistics (F) for the linear model or Wald Chi-square (χ^2) for the ordinal model, and P values (Sig.) are all included. P values are Sidak adjusted for MRI data.

post-irradiation ($P \geq 0.962$). When looking within the effect of mouse strain, pooling all the time points and both sexes, we find significant differences between C57BL/6 and BALB/c mice ($P \leq 0.015$) but not between the N and J substrains within each strain ($P \geq 0.145$) but only for T2-weighted imaging. Lesion sizes in BALB/c mice are consistently larger than C57BL/6 mice in T2-weighted imaging but not in T1-weighted imaging. For sex, there was no difference between male and female mice. Both findings would be expected from Table 3.

Table 3 noted an interaction effect between mouse strain and time. Statistics for the pairwise comparison for the interaction terms for the MRI data are presented on Table 5. Considering that sex and substrain were not found to be significantly different, Figure 16 compares the BALB/c strain versus the C57BL/6 strain for all three measurements as a function of time with substrains and sexes averaged out. Again, differences between the strains can be observed on T2 at all time points. The data for T1-weighted lesion volume is noisier and thus harder to interpret, but it suggests that BALB/c mice might have slightly larger lesions at earlier time points. In fact, we found significant differences between BALB/cN mice and C57BL/6N at week 4 ($P = 0.005$). The histological data if anything suggest that there might not be large differences at either time point.

Table 4. Pairwise comparisons of the main effects for T2- and T1-weighted MRI lesion volumes from a linear mixed model.

		<i>T2-Weighted MRI</i>			<i>T1-Weighted MRI</i>		
Strain		Mean Diff.	Std. Err.	Sig.	Mean Diff.	Std. Err.	Sig.
BALB/cN	BALB/cJ	7.927	3.508	0.145	4.875	5.321	0.932
	C57BL/6N	22.757*	3.633	0.000	10.065	5.518	0.355
	C57BL/6J	18.585*	3.771	0.000	1.759	5.684	1.000
BALB/cJ	BALB/cN	-7.927	3.508	0.145	-4.875	5.321	0.932
	C57BL/6N	14.831*	3.269	0.000	5.190	4.820	0.867
	C57BL/6J	10.658*	3.417	0.015	-3.117	5.010	0.990
C57BL/6N	BALB/cN	-22.757*	3.633	0.000	-10.065	5.518	0.355
	BALB/cJ	-14.831*	3.269	0.000	-5.190	4.820	0.867
	C57BL/6J	-4.172	3.511	0.804	-8.306	5.155	0.508
C57BL/6J	BALB/cJ	-18.585*	3.771	0.000	-1.759	5.684	1.000
	BALB/cN	-10.658*	3.417	0.015	3.117	5.010	0.990
	C57BL/6N	4.172	3.511	0.804	8.306	5.155	0.508
		<i>T2-Weighted MRI</i>			<i>T1-Weighted MRI</i>		
Sex		Mean Diff.	Std. Err.	Sig.	Mean Diff.	Std. Err.	Sig.
F	M	0.178	2.560	0.945	2.926	3.823	0.446
M	F	-0.178	2.560	0.945	-2.926	3.823	0.446
		<i>T2-Weighted MRI</i>			<i>T1-Weighted MRI</i>		
Time		Mean Diff.	Std. Err.	Sig.	Mean Diff.	Std. Err.	Sig.
4	6	-10.513*	2.400	0.000	-12.775*	4.046	0.006
	8	-11.610*	2.401	0.000	-10.844*	3.847	0.016
6	4	10.513*	2.400	0.000	12.775*	4.046	0.006
	8	-1.097	2.579	0.965	1.931	4.439	0.962
8	4	11.610*	2.401	0.000	10.844*	3.847	0.016
	6	1.097	2.579	0.965	-1.931	4.439	0.962

The parameters tested, mean differences (Mean Diff.), standard errors (Std. Err.), and P values (Sig.) are all included. P values are Sidak adjusted.

Discussion

The goal was to determine if mouse strain and sex have an impact when modeling radiation necrosis. The rationale was that these two parameters are known to not be consistent in prior reports of murine models of radiation necrosis. Our prior publications have already shown that radiation delivery parameters (dose, device, and fractionation) can all affect the results (112, 125). Additional biological factors not included in this report but also of interest would be age at

Table 5. Pairwise comparisons of the interaction effects for T2- and T1-weighted MRI lesion volumes from a linear mixed model.

			<i>T2-Weighted MRI</i>			<i>T1-Weighted MRI</i>		
Sex * Time			Mean Diff.	Std. Err.	Sig.	Mean Diff.	Std. Err.	Sig.
4	F	M	2.169	2.891	0.454	3.059	4.539	0.501
6			0.289	4.626	0.950	2.498	7.526	0.740
8			-1.925	4.006	0.632	3.220	6.327	0.611
Strain * Sex			Mean Diff.	Std. Err.	Sig.	Mean Diff.	Std. Err.	Sig.
BALB/cN	F	M	5.547	5.113	0.280	19.113*	7.993	0.018
BALB/cJ			-0.196	4.363	0.964	0.011	6.433	0.999
C57BL/6N			-3.716	4.631	0.424	-15.406*	6.867	0.027
C57BL/6J			-0.923	4.881	0.850	7.985	7.195	0.270
Strain * Time			Mean Diff.	Std. Err.	Sig.	Mean Diff.	Std. Err.	Sig.
4	BALB/cN	BALB/cJ	9.996	3.881	0.064	8.011	6.089	0.718
		C57BL/6N	15.480*	4.088	0.001	21.766*	6.419	0.005
		C57BL/6J	14.568*	4.088	0.003	11.819	6.419	0.342
	BALB/cJ	BALB/cN	-9.996	3.881	0.064	-8.011	6.089	0.718
		C57BL/6N	5.484	4.085	0.699	13.755	6.412	0.184
		C57BL/6J	4.573	4.085	0.842	3.809	6.412	0.992
	C57BL/6N	BALB/cN	-15.480*	4.088	0.001	-21.766*	6.419	0.005
		BALB/cJ	-5.484	4.085	0.699	-13.755	6.412	0.184
		C57BL/6J	-0.911	4.277	1.000	-9.946	6.717	0.597
	C57BL/6J	BALB/cN	-14.568*	4.088	0.003	-11.819	6.419	0.342
		BALB/cJ	-4.573	4.085	0.842	-3.809	6.412	0.992
		C57BL/6N	0.911	4.277	1.000	9.946	6.717	0.597
6	BALB/cN	BALB/cJ	12.640	5.945	0.193	8.393	9.736	0.949
		C57BL/6N	35.301*	6.566	0.000	22.012	10.768	0.231
		C57BL/6J	28.368*	6.584	0.000	9.632	10.767	0.939
	BALB/cJ	BALB/cN	-12.640	5.945	0.193	-8.393	9.736	0.949
		C57BL/6N	22.661*	5.491	0.000	13.620	8.762	0.542
		C57BL/6J	15.728*	5.517	0.029	1.239	8.768	1.000
	C57BL/6N	BALB/cN	-35.301*	6.566	0.000	-22.012	10.768	0.231
		BALB/cJ	-22.661*	5.491	0.000	-13.620	8.762	0.542
		C57BL/6J	-6.934	5.928	0.813	-12.381	9.463	0.723
	C57BL/6J	BALB/cN	-28.368*	6.584	0.000	-9.632	10.767	0.939
		BALB/cJ	-15.728*	5.517	0.029	-1.239	8.768	1.000
		C57BL/6N	6.934	5.928	0.813	12.381	9.463	0.723

Table 5 continued

8	BALB/cN	BALB/cJ	1.143	5.333	1.000	-1.778	8.505	1.000
		C57BL/6N	17.490*	5.345	0.008	-13.583	8.400	0.495
		C57BL/6J	12.818	5.896	0.173	-16.175	9.275	0.405
	BALB/cJ	BALB/cN	-1.143	5.333	1.000	1.778	8.505	1.000
		C57BL/6N	16.347*	5.042	0.009	-11.806	8.024	0.604
		C57BL/6J	11.674	5.588	0.209	-14.398	8.874	0.491
	C57BL/6N	BALB/cN	-17.490*	5.345	0.008	13.583	8.400	0.495
		BALB/cJ	-16.347*	5.042	0.009	11.806	8.024	0.604
		C57BL/6J	-4.673	5.592	0.955	-2.592	8.784	1.000
	C57BL/6J	BALB/cN	-12.818	5.896	0.173	16.175	9.275	0.405
		BALB/cJ	-11.674	5.588	0.209	14.398	8.874	0.491
		C57BL/6N	4.673	5.592	0.955	2.592	8.784	1.000

The parameter combinations tested, mean differences (Mean Diff.), and P values (Sig.) are all included. P values are Sidak adjusted. The first column indicates the variable that was held constant whereas the second and third column indicates the parameters that are being compared.

irradiation and species, as rats have also been used to model radiation necrosis (132, 133). We compared BALB/c and C57BL/6 mice of both sexes that received 80 Gy in a single fraction based on MRI-derived lesion volumes and a histological score.

Our results are mixed, with Table 3 and Table 4 showing that strain is a significant factor for T2-weighted lesion volume but not T1-weighted lesion volume or histological score. There is a potential interaction between strain and time after irradiation for T1-weighted lesion volume and histology which still suggests that strain has a significant effect on these outcomes. Overall, our results suggest that BALB/c mice are likely more sensitive to radiation necrosis than C57BL/6 mice. This is consistent with radiosensitivity data previously reported for whole-body irradiation (128, 129). When looking within strain, we also had included N and J substrains for each, but these were not found to be significant. Similarly, sex did not seem to significantly affect our results.

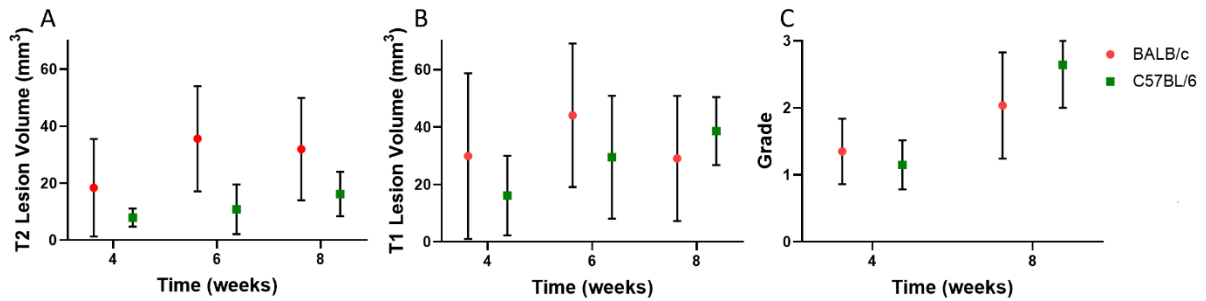


Figure 16. MRI lesion volumes and histological grade as a function of mouse strain and time post-irradiation. Plots show the T2-weighted (Panel A) and T1-weighted (Panel B) lesion size (in mm³) and histological grade over time (in weeks) for mice that received 80 Gy (Panel C). Data includes both substrains for each strain and both sexes. Symbols indicate the mean and the error bars are standard deviation.

A potential reason for the difference between T1-weighted and T2-weighted lesion volume is that T2-weighted lesion volume was more consistent, with smaller standard deviations and therefore more statistical power. Statistical power also needs to be considered for the histological grade, since due to its ordinal nature we could not use the more powerful parametric statistical analysis. Additional considerations that impact our results include the choice of radiation dose and the consistency of mouse placement in the irradiator. For the latter, if our irradiation setup had included a more tightly shaped mouse immobilizer and more precise localization of the holder itself, it is likely that our mouse to mouse variation would be smaller. Finally, our results are restricted to modeling radiation necrosis which we have previously shown requires very large radiation doses (*125, 134*). We cannot guarantee that this would extend to other models of radiation induced pathology, particularly those generated with lower radiation doses.

Conclusion

The goal of our study was to test the impact of mouse strain and sex when modeling radiation necrosis. Our results show that mouse strain can impact the sensitivity to radiation in a manner consistent with prior work on whole body irradiation. Though there are known genetic differences within the substrains for BALB/c and C57BL/6 mice, these substrains were not significantly different in their response. Similarly, sex did not appear to modify the response in our model.

List of abbreviations

MRI – magnetic resonance imaging

H&E – hematoxylin and eosin

Declarations

Ethics approval and consent to participate

All animal experiments were approved by the Purdue Animal Care and Use Committee.

Consent for publication

“Not applicable”

Availability of data and materials

“The datasets used and/or analyzed during the current study are available from the corresponding author on reasonable request.”

Competing interests

The authors declare that they have no competing interests.

Funding

There are no funding sources to report for this study.

Authors' contributions

AJB helped design and performed the experiments, analyzed the data, and wrote the manuscript.

CJPT designed and oversaw experiments and data analysis and wrote the manuscript.

Acknowledgements

We would like to thank the following Purdue core facilities where the work was performed:

Purdue Small Animal MRI facility and Histology Research Lab. We wish to acknowledge Dr.

Chang-Deng Hu for providing access to the X-Rad 320. Finally, the statistical analysis was done

with the help of the Statistical Consulting Service from the Department of Statistics at Purdue

University.

APPENDIX A: SPSS T2-WEIGHTED MRI MIXED MODEL ANALYSIS

MIXED T2 BY Week Substrain Sex

```

/CRITERIA=DFMETHOD(SATTERTHWAITE) CIN(95) MXITER(100) MXSTEP(10) SCORING(1)
SINGULAR(0.000000000001) HCONVERGE(0, ABSOLUTE) LCONVERGE(0, ABSOLUTE)
PCONVERGE(0.000001, ABSOLUTE)
/FIXED=Week Substrain Sex Substrain*Week Substrain*Sex Sex*Week | SSTYPE(3)
/METHOD=REML
/REPEATED=Week | SUBJECT(Number) COVTYPE(AR1)
/EMMEANS=TABLES(Substrain) COMPARE ADJ(SIDAK)
/EMMEANS=TABLES(Sex) COMPARE ADJ(SIDAK)
/EMMEANS=TABLES(Week) COMPARE ADJ(SIDAK)
/EMMEANS=TABLES(Sex*Week) COMPARE(Sex) ADJ(SIDAK)
/EMMEANS=TABLES(Sex*Week) COMPARE(Week) ADJ(SIDAK)
/EMMEANS=TABLES(Substrain*Sex) COMPARE(Substrain) ADJ(SIDAK)
/EMMEANS=TABLES(Substrain*Sex) COMPARE(Sex) ADJ(SIDAK)
/EMMEANS=TABLES(Substrain*Week) COMPARE(Substrain) ADJ(SIDAK)
/EMMEANS=TABLES(Substrain*Week) COMPARE(Week) ADJ(SIDAK).

```

Mixed Model Analysis

Notes		
Output Created		17-JAN-2020 11:59:01
Comments		
Input	Data	
	Active Dataset	DataSet1
	Filter	<none>
	Weight	<none>
	Split File	<none>
	N of Rows in Working Data	188
	File	
Missing Value Handling	Definition of Missing	User-defined missing values are treated as missing.
	Cases Used	Statistics are based on all cases with valid data for all variables in the model.

Syntax

```
MIXED T2 BY Week Substrain
Sex

/CRITERIA=DFMETHOD(SAT
TERTHWAITE) CIN(95)
MXITER(100) MXSTEP(10)
SCORING(1)

SINGULAR(0.000000000001)
HCONVERGE(0, ABSOLUTE)
LCONVERGE(0, ABSOLUTE)
PCONVERGE(0.000001,
ABSOLUTE)
/FIXED=Week Substrain Sex
Substrain*Week
Substrain*Sex Sex*Week |
SSTYPE(3)
/METHOD=REML
/REPEATED=Week |
SUBJECT(Number)
COVTYPE(AR1)

/EMMEANS=TABLES(Substra
in) COMPARE ADJ(SIDAK)
/EMMEANS=TABLES(Sex)
COMPARE ADJ(SIDAK)
/EMMEANS=TABLES(Week)
COMPARE ADJ(SIDAK)

/EMMEANS=TABLES(Sex*W
eek) COMPARE(Sex)
ADJ(SIDAK)

/EMMEANS=TABLES(Sex*W
eek) COMPARE(Week)
ADJ(SIDAK)

/EMMEANS=TABLES(Substra
in*Sex) COMPARE(Substrain)
ADJ(SIDAK)
```

		/EMMEANS=TABLES(Substrain*Sex) COMPARE(Sex) ADJ(SIDAK)
		/EMMEANS=TABLES(Substrain*Week) COMPARE(Substrain) ADJ(SIDAK)
		/EMMEANS=TABLES(Substrain*Week) COMPARE(Week) ADJ(SIDAK).
Resources	Processor Time	00:00:00.08
	Elapsed Time	00:00:00.08

Model Dimension^a

		Number of Levels	Covariance Structure	Number of Parameters	Subject Variables	
Fixed Effects	Intercept	1		1		
	Week	3		2		
	Substrain	4		3		
	Sex	2		1		
	Week * Substrain	12		6		
	Substrain * Sex	8		3		
	Week * Sex	6		2		
Repeated Effects	Week	3	First-Order Autoregressive	2	Number	
Total		39		20		

Information Criteria^a

-2 Restricted Log Likelihood	1407.882
Akaike's Information Criterion (AIC)	1411.882
Hurvich and Tsai's Criterion (AICC)	1411.954
Bozdogan's Criterion (CAIC)	1420.153
Schwarz's Bayesian Criterion (BIC)	1418.153

The information criteria are displayed in smaller-is-better form.^a

a. Dependent Variable: T2.

Fixed Effects

Type III Tests of Fixed Effects^a

Source	Numerator df	Denominator df	F	Sig.
Intercept	1	96.785	259.761	.000
Week	2	123.707	15.015	.000
Substrain	3	94.013	16.194	.000
Sex	1	99.763	.005	.945
Week * Substrain	6	123.433	2.310	.038
Substrain * Sex	3	102.513	.668	.574
Week * Sex	2	125.381	.358	.700

a. Dependent Variable: T2.

Covariance Parameters

Estimates of Covariance Parameters^a

Parameter	Estimate	Std. Error
Repeated Measures		
AR1 diagonal	182.969888	20.396748
AR1 rho	.250130	.097780

a. Dependent Variable: T2.

Estimated Marginal Means

1. Substrain

Substrain	Estimates ^a			95% Confidence Interval	
	Mean	Std. Error	df	Lower Bound	Upper Bound
1BALB/cN	32.617	2.753	142.462	27.175	38.060
2BALB/cJ	24.691	2.246	76.852	20.219	29.163
3C57BL/6N	9.860	2.385	88.947	5.121	14.600
4C57BL/6J	14.033	2.576	78.910	8.905	19.160

a. Dependent Variable: T2.

Pairwise Comparisons ^a							95% Confidence Interval for Difference ^c	
(I) Substrain	(J) Substrain	Mean Difference (I-J)	Std. Error	df	Sig. ^c	Lower Bound		
1BALB/cN	2BALB/cJ	7.927	3.508	113.462	.145	-1.468		
	3C57BL/6N	22.757*	3.633	120.718	.000	13.039		
	4C57BL/6J	18.585*	3.771	110.276	.000	8.483		
2BALB/cJ	1BALB/cN	-7.927	3.508	113.462	.145	-17.321		
	3C57BL/6N	14.831*	3.269	83.479	.000	6.022		
	4C57BL/6J	10.658*	3.417	78.014	.015	1.433		
3C57BL/6N	1BALB/cN	-22.757*	3.633	120.718	.000	-32.475		
	2BALB/cJ	-14.831*	3.269	83.479	.000	-23.639		
	4C57BL/6J	-4.172	3.511	83.392	.804	-13.634		
4C57BL/6J	1BALB/cN	-18.585*	3.771	110.276	.000	-28.686		
	2BALB/cJ	-10.658*	3.417	78.014	.015	-19.883		
	3C57BL/6N	4.172	3.511	83.392	.804	-5.289		

Univariate Tests^a

Numerator df	Denominator df	F	Sig.
3	93.147	16.194	.000

The F tests the effect of Substrain. This test is based on the linearly independent pairwise comparisons among the estimated marginal means.^a

a. Dependent Variable: T2.

2. Sex

Estimates^a

Sex	Mean	Std. Error	df	95% Confidence Interval	
				Lower Bound	Upper Bound
F	20.389	1.525	81.465	17.355	23.423
M	20.211	2.031	109.014	16.187	24.236

a. Dependent Variable: T2.

Pairwise Comparisons^a

(I) Sex	(J) Sex	Mean Difference (I-J)	Std. Error	df	Sig. ^b	95% Confidence Interval for Difference ^b	
						Lower Bound	Upper Bound
F	M	.178	2.560	99.763	.945	-4.901	5.256
M	F	-.178	2.560	99.763	.945	-5.256	4.901

Based on estimated marginal means^a

a. Dependent Variable: T2.

b. Adjustment for multiple comparisons: Sidak.

Univariate Tests^a

Numerator df	Denominator df	F	Sig.
1	99.763	.005	.945

The F tests the effect of Sex. This test is based on the linearly independent pairwise comparisons among the estimated marginal means.^a

a. Dependent Variable: T2.

3. Week

Estimates^a

Week	Mean	Std. Error	df	95% Confidence Interval	
				Lower Bound	Upper Bound
4	12.926	1.445	161.007	10.071	15.781
6	23.439	2.185	161.212	19.124	27.753
8	24.536	1.989	163.072	20.609	28.463

a. Dependent Variable: T2.

Pairwise Comparisons^a

(I) Week	(J) Week	Mean Difference (I-J)	Std. Error	df	Sig. ^c	95% Confidence Interval for Difference ^c	
						Lower Bound	Upper Bound
4	6	-10.513 [*]	2.400	105.783	.000	-16.335	
	8	-11.610 [*]	2.401	168.637	.000	-17.401	
6	4	10.513 [*]	2.400	105.783	.000	4.691	
	8	-1.097	2.579	82.730	.965	-7.382	
8	4	11.610 [*]	2.401	168.637	.000	5.820	
	6	1.097	2.579	82.730	.965	-5.187	

Univariate Tests^a

Numerator df	Denominator df	F	Sig.
2	109.671	15.015	.000

The F tests the effect of Week. This test is based on the linearly independent pairwise comparisons among the estimated marginal means.^a

a. Dependent Variable: T2.

4. Sex * Week

Estimates ^a						
Sex	Week	Mean	Std. Error	df	95% Confidence Interval	
					Lower Bound	Upper Bound
F	4	14.011	1.945	161.086	10.169	17.852
	6	23.584	2.537	169.751	18.576	28.591
	8	23.574	2.357	161.951	18.919	28.228
M	4	11.841	2.139	160.941	7.618	16.065
	6	23.294	3.717	149.786	15.951	30.638
	8	25.499	3.221	163.504	19.138	31.860

a. Dependent Variable: T2.

Pairwise Comparisons ^a								
Week	(I) Sex	(J) Sex	Mean Difference (I-J)	Std. Error	df	Sig. ^b	95% Confidence Interval for Difference ^b	
								Lower Bound
4	F	M	2.169	2.891	161.007	.454	-3.540	
	M	F	-2.169	2.891	161.007	.454	-7.878	
6	F	M	.289	4.626	156.901	.950	-8.848	
	M	F	-.289	4.626	156.901	.950	-9.427	
8	F	M	-1.925	4.006	162.887	.632	-9.835	
	M	F	1.925	4.006	162.887	.632	-5.986	

Univariate Tests ^a				
Week	Numerator df	Denominator df	F	Sig.
4	1	161.007	.563	.454
6	1	156.901	.004	.950
8	1	162.887	.231	.632

Each F tests the simple effects of Sex within each level combination of the other effects shown. These tests are based on the linearly independent pairwise comparisons among the estimated marginal means.^a

a. Dependent Variable: T2.

5. Sex * Week

Estimates ^a						
Sex	Week	Mean	Std. Error	df	95% Confidence Interval	
					Lower Bound	Upper Bound
F	4	14.011	1.945	161.086	10.169	17.852
	6	23.584	2.537	169.751	18.576	28.591
	8	23.574	2.357	161.951	18.919	28.228
M	4	11.841	2.139	160.941	7.618	16.065
	6	23.294	3.717	149.786	15.951	30.638
	8	25.499	3.221	163.504	19.138	31.860

a. Dependent Variable: T2.

Pairwise Comparisons ^a								
Sex	(I) Week	(J) Week	Mean Difference (I-J)	Std. Error	df	Sig. ^c	95% Confidence Interval for Difference ^c	
							Lower Bound	
F	4	6	-9.573*	2.878	106.464	.004	-16.554	
		8	-9.563*	2.980	168.315	.005	-16.750	
	6	4	9.573*	2.878	106.464	.004	2.592	
		8	.010	3.038	88.227	1.000	-7.385	
	8	4	9.563*	2.980	168.315	.005	2.377	
		6	-.010	3.038	88.227	1.000	-7.405	
M	4	6	-11.453*	4.012	104.288	.016	-21.190	
		8	-13.657*	3.792	168.997	.001	-22.802	
	6	4	11.453*	4.012	104.288	.016	1.716	
		8	-2.204	4.325	80.887	.941	-12.749	
	8	4	13.657*	3.792	168.997	.001	4.512	
		6	2.204	4.325	80.887	.941	-8.341	

Univariate Tests^a

Sex	Numerator df	Denominator df	F	Sig.
F	2	110.784	7.309	.001
M	2	113.876	7.740	.001

Each F tests the simple effects of Week within each level combination of the other effects shown. These tests are based on the linearly independent pairwise comparisons among the estimated marginal means.^a

a. Dependent Variable: T2.

6. Substrain * Sex

Estimates^a

Substrain	Sex	Mean	Std. Error	df	95% Confidence Interval	
					Lower Bound	Upper Bound
1BALB/cN	F	35.391	2.678	71.735	30.051	40.731
	M	29.844	4.589	167.096	20.784	38.904
2BALB/cJ	F	24.593	2.668	72.627	19.276	29.910
	M	24.789	3.534	82.725	17.760	31.818
3C57BL/6N	F	8.002	3.090	103.063	1.875	14.130
	M	11.718	3.543	82.310	4.670	18.767
4C57BL/6J	F	13.571	3.549	82.052	6.512	20.630
	M	14.494	3.549	82.052	7.435	21.554

a. Dependent Variable: T2.

Pairwise Comparisons^a

Sex	(I) Substrain	(J) Substrain	Mean Difference (I-J)	Std. Error	df	Sig. ^c	95% Confidence Interval for Difference ^c	
							Lower Bound	
F	1BALB/cN	2BALB/cJ	10.798*	3.776	72.261	.033	.585	
		3C57BL/6N	27.389*	4.089	88.283	.000	16.383	
		4C57BL/6J	21.820*	4.437	78.299	.000	9.844	
	2BALB/cJ	1BALB/cN	-10.798*	3.776	72.261	.033	-21.011	
		3C57BL/6N	16.591*	4.063	89.693	.001	5.659	
		4C57BL/6J	11.022	4.414	79.424	.084	-.888	
	3C57BL/6N	1BALB/cN	-27.389*	4.089	88.283	.000	-38.394	
		2BALB/cJ	-16.591*	4.063	89.693	.001	-27.522	
		4C57BL/6J	-5.569	4.675	91.340	.802	-18.140	
	4C57BL/6J	1BALB/cN	-21.820*	4.437	78.299	.000	-33.796	
		2BALB/cJ	-11.022	4.414	79.424	.084	-22.932	
		3C57BL/6N	5.569	4.675	91.340	.802	-7.002	
M	1BALB/cN	2BALB/cJ	5.055	5.604	142.302	.937	-9.897	
		3C57BL/6N	18.126*	5.648	141.650	.010	3.054	
		4C57BL/6J	15.349*	5.656	140.846	.044	.256	
	2BALB/cJ	1BALB/cN	-5.055	5.604	142.302	.937	-20.007	
		3C57BL/6N	13.070	4.939	84.415	.057	-.236	
		4C57BL/6J	10.294	4.946	84.099	.220	-3.033	
	3C57BL/6N	1BALB/cN	-18.126*	5.648	141.650	.010	-33.197	
		2BALB/cJ	-13.070	4.939	84.415	.057	-26.377	
		4C57BL/6J	-2.776	4.964	83.525	.994	-16.154	
	4C57BL/6J	1BALB/cN	-15.349*	5.656	140.846	.044	-30.442	
		2BALB/cJ	-10.294	4.946	84.099	.220	-23.622	
		3C57BL/6N	2.776	4.964	83.525	.994	-10.602	

Univariate Tests^a

Sex	Numerator df	Denominator df	F	Sig.
F	3	82.263	17.333	.000
M	3	99.648	4.873	.003

Each F tests the simple effects of Substrain within each level combination of the other effects shown. These tests are based on the linearly independent pairwise comparisons among the estimated marginal means.^a

a. Dependent Variable: T2.

7. Substrain * Sex

Estimates ^a						
Substrain	Sex	Mean	Std. Error	df	95% Confidence Interval	
					Lower Bound	Upper Bound
1BALB/cN	F	35.391	2.678	71.735	30.051	40.731
	M	29.844	4.589	167.096	20.784	38.904
2BALB/cJ	F	24.593	2.668	72.627	19.276	29.910
	M	24.789	3.534	82.725	17.760	31.818
3C57BL/6N	F	8.002	3.090	103.063	1.875	14.130
	M	11.718	3.543	82.310	4.670	18.767
4C57BL/6J	F	13.571	3.549	82.052	6.512	20.630
	M	14.494	3.549	82.052	7.435	21.554

a. Dependent Variable: T2.

Pairwise Comparisons ^a								
Substrain	(I) Sex	(J) Sex	Mean Difference (I-J)	Std. Error	df	Sig. ^b	95% Confidence Interval for Difference ^b	
							Lower Bound	
1BALB/cN	F	M	5.547	5.113	151.942	.280	-4.554	
	M	F	-5.547	5.113	151.942	.280	-15.648	
2BALB/cJ	F	M	-.196	4.363	81.123	.964	-8.877	
	M	F	.196	4.363	81.123	.964	-8.485	
3C57BL/6N	F	M	-3.716	4.631	92.711	.424	-12.913	
	M	F	3.716	4.631	92.711	.424	-5.481	
4C57BL/6J	F	M	-.923	4.881	85.705	.850	-10.627	
	M	F	.923	4.881	85.705	.850	-8.781	

Univariate Tests^a

Substrain	Numerator df	Denominator df	F	Sig.
1BALB/cN	1	151.942	1.177	.280
2BALB/cJ	1	81.123	.002	.964
3C57BL/6N	1	92.711	.644	.424
4C57BL/6J	1	85.705	.036	.850

Each F tests the simple effects of Sex within each level combination of the other effects shown. These tests are based on the linearly independent pairwise comparisons among the estimated marginal means.^a

a. Dependent Variable: T2.

8. Substrain * Week

Substrain	Week	Estimates ^a			95% Confidence Interval	
		Mean	Std. Error	df	Lower Bound	Upper Bound
1BALB/cN	4	22.937	2.750	160.555	17.506	28.368
	6	42.516	5.062	128.023	32.501	52.532
	8	32.399	4.062	164.535	24.378	40.420
2BALB/cJ	4	12.941	2.746	160.038	7.519	18.364
	6	29.876	3.566	169.643	22.837	36.915
	8	31.256	3.601	161.870	24.145	38.366
3C57BL/6N	4	7.457	3.024	161.520	1.486	13.429
	6	7.215	4.173	167.636	-1.024	15.454
	8	14.909	3.607	161.055	7.785	22.032
4C57BL/6J	4	8.369	3.025	160.941	2.395	14.342
	6	14.148	4.210	169.997	5.838	22.459
	8	19.581	4.273	162.887	11.143	28.020

a. Dependent Variable: T2.

Pairwise Comparisons^a

Week	(I) Substrain	(J) Substrain	Mean Difference (I-J)	Std. Error	df	Sig. ^c	95% Confidence Interval for Difference ^c	
							Lower Bound	Upper Bound
4	1BALB/cN	2BALB/cJ	9.996	3.881	160.153	.064	-.342	20.333
		3C57BL/6N	15.480*	4.088	160.972	.001	4.590	26.369
		4C57BL/6J	14.568*	4.088	160.767	.003	3.679	25.458
	2BALB/cJ	1BALB/cN	-9.996	3.881	160.153	.064	-20.333	.342
		3C57BL/6N	5.484	4.085	160.719	.699	-5.398	16.366
		4C57BL/6J	4.573	4.085	160.537	.842	-6.309	15.455
	3C57BL/6N	1BALB/cN	-15.480*	4.088	160.972	.001	-26.369	-4.590
		2BALB/cJ	-5.484	4.085	160.719	.699	-16.366	5.398
		4C57BL/6J	-.911	4.277	161.232	1.000	-12.304	10.481
	4C57BL/6J	1BALB/cN	-14.568*	4.088	160.767	.003	-25.458	-3.679
		2BALB/cJ	-4.573	4.085	160.537	.842	-15.455	6.309
		3C57BL/6N	.911	4.277	161.232	1.000	-10.481	12.304
6	1BALB/cN	2BALB/cJ	12.640	5.945	152.258	.193	-3.207	28.488
		3C57BL/6N	35.301*	6.566	147.302	.000	17.791	52.812
		4C57BL/6J	28.368*	6.584	152.696	.000	10.818	45.917
	2BALB/cJ	1BALB/cN	-12.640	5.945	152.258	.193	-28.488	3.207
		3C57BL/6N	22.661*	5.491	169.541	.000	8.044	37.278
		4C57BL/6J	15.728*	5.517	169.919	.029	1.041	30.414
	3C57BL/6N	1BALB/cN	-35.301*	6.566	147.302	.000	-52.812	-17.791
		2BALB/cJ	-22.661*	5.491	169.541	.000	-37.278	-8.044
		4C57BL/6J	-6.934	5.928	169.457	.813	-22.714	8.847
	4C57BL/6J	1BALB/cN	-28.368*	6.584	152.696	.000	-45.917	-10.818
		2BALB/cJ	-15.728*	5.517	169.919	.029	-30.414	-1.041
		3C57BL/6N	6.934	5.928	169.457	.813	-8.847	22.714

8	1BALB/cN	2BALB/cJ	1.143	5.333	163.544	1.000	-13.061	15.348
		3C57BL/6N	17.490*	5.345	162.846	.008	3.254	31.727
		4C57BL/6J	12.818	5.896	163.693	.173	-2.885	28.520
	2BALB/cJ	1BALB/cN	-1.143	5.333	163.544	1.000	-15.348	13.061
		3C57BL/6N	16.347*	5.042	160.812	.009	2.916	29.777
		4C57BL/6J	11.674	5.588	162.472	.209	-3.210	26.558
	3C57BL/6N	1BALB/cN	-17.490*	5.345	162.846	.008	-31.727	-3.254
		2BALB/cJ	-16.347*	5.042	160.812	.009	-29.777	-2.916
		4C57BL/6J	-4.673	5.592	162.146	.955	-19.568	10.223
	4C57BL/6J	1BALB/cN	-12.818	5.896	163.693	.173	-28.520	2.885
		2BALB/cJ	-11.674	5.588	162.472	.209	-26.558	3.210
		3C57BL/6N	4.673	5.592	162.146	.955	-10.223	19.568

Based on estimated marginal means^a

*. The mean difference is significant at the .05 level.

a. Dependent Variable: T2.

c. Adjustment for multiple comparisons: Sidak.

Univariate Tests^a

Week	Numerator df	Denominator df	F	Sig.
4	3	160.711	6.228	.001
6	3	157.984	11.978	.000
8	3	162.490	5.332	.002

Each F tests the simple effects of Substrain within each level combination of the other effects shown. These tests are based on the linearly independent pairwise comparisons among the estimated marginal means.^a

a. Dependent Variable: T2.

9. Substrain * Week

Estimates ^a						
Substrain	Week	Mean	Std. Error	df	95% Confidence Interval	
					Lower Bound	Upper Bound
1BALB/cN	4	22.937	2.750	160.555	17.506	28.368
	6	42.516	5.062	128.023	32.501	52.532
	8	32.399	4.062	164.535	24.378	40.420
2BALB/cJ	4	12.941	2.746	160.038	7.519	18.364
	6	29.876	3.566	169.643	22.837	36.915
	8	31.256	3.601	161.870	24.145	38.366
3C57BL/6N	4	7.457	3.024	161.520	1.486	13.429
	6	7.215	4.173	167.636	-1.024	15.454
	8	14.909	3.607	161.055	7.785	22.032
4C57BL/6J	4	8.369	3.025	160.941	2.395	14.342
	6	14.148	4.210	169.997	5.838	22.459
	8	19.581	4.273	162.887	11.143	28.020

a. Dependent Variable: T2.

Pairwise Comparisons^a

Substrain	(I) Week	(J) Week	Mean Difference (I-J)	Std. Error	df	Sig. ^c	95% Confidence Interval for Difference ^c	
							Lower Bound	
1BALB/cN	4	6	-19.579*	5.293	93.633	.001	-32.447	
		8	-9.462	4.714	168.343	.133	-20.832	
	6	4	19.579*	5.293	93.633	.001	6.711	
		8	10.117	5.531	81.220	.198	-3.366	
	8	4	9.462	4.714	168.343	.133	-1.908	
		6	-10.117	5.531	81.220	.198	-23.601	
2BALB/cJ	4	6	-16.935*	4.024	109.298	.000	-26.692	
		8	-18.314*	4.376	167.309	.000	-28.868	
	6	4	16.935*	4.024	109.298	.000	7.178	
		8	-1.380	4.352	83.127	.985	-11.984	
	8	4	18.314*	4.376	167.309	.000	7.760	
		6	1.380	4.352	83.127	.985	-9.225	
3C57BL/6N	4	6	.242	4.697	108.110	1.000	-11.149	
		8	-7.451	4.620	169.675	.292	-18.592	
	6	4	-.242	4.697	108.110	1.000	-11.634	
		8	-7.694	4.910	92.874	.320	-19.633	
	8	4	7.451	4.620	169.675	.292	-3.689	
		6	7.694	4.910	92.874	.320	-4.246	
4C57BL/6J	4	6	-5.780	4.722	115.430	.532	-17.221	
		8	-11.213	5.125	168.429	.087	-23.573	
	6	4	5.780	4.722	115.430	.532	-5.661	
		8	-5.433	5.208	81.977	.657	-18.126	
	8	4	11.213	5.125	168.429	.087	-1.147	
		6	5.433	5.208	81.977	.657	-7.261	

Univariate Tests^a

Substrain	Numerator df	Denominator df	F	Sig.
1BALB/cN	2	117.240	7.021	.001
2BALB/cJ	2	103.132	12.018	.000
3C57BL/6N	2	119.745	1.669	.193
4C57BL/6J	2	103.191	2.434	.093

Each F tests the simple effects of Week within each level combination of the other effects shown. These tests are based on the linearly independent pairwise comparisons among the estimated marginal means.^a

a. Dependent Variable: T2.

APPENDIX B: SPSS T1-WEIGHTED MRI MIXED MODEL ANALYSIS

```
MIXED T1 BY Week Substrain Sex
  /CRITERIA=DFMETHOD(SATTERTHWAITE) CIN(95) MXITER(100) MXSTEP(10) SCORING(1)
  SINGULAR(0.000000000001) HCONVERGE(0, ABSOLUTE) LCONVERGE(0, ABSOLUTE)
PCONVERGE(0.000001, ABSOLUTE)
  /FIXED=Week Substrain Sex Substrain*Week Substrain*Sex Sex*Week | SSTYPE(3)
  /METHOD=REML
  /REPEATED=Week | SUBJECT(Number) COVTYPE(AR1)
  /EMMEANS=TABLES(Substrain) COMPARE ADJ(SIDAK)
  /EMMEANS=TABLES(Sex) COMPARE ADJ(SIDAK)
  /EMMEANS=TABLES(Week) COMPARE ADJ(SIDAK)
  /EMMEANS=TABLES(Sex*Week) COMPARE(Sex) ADJ(SIDAK)
  /EMMEANS=TABLES(Sex*Week) COMPARE(Week) ADJ(SIDAK)
  /EMMEANS=TABLES(Substrain*Sex) COMPARE(Substrain) ADJ(SIDAK)
  /EMMEANS=TABLES(Substrain*Sex) COMPARE(Sex) ADJ(SIDAK)
  /EMMEANS=TABLES(Substrain*Week) COMPARE(Substrain) ADJ(SIDAK)
  /EMMEANS=TABLES(Substrain*Week) COMPARE(Week) ADJ(SIDAK).
```

Mixed Model Analysis

Notes		
Output Created		17-JAN-2020 11:59:48
Comments		
Input	Data	
	Active Dataset	DataSet1
	Filter	<none>
	Weight	<none>
	Split File	<none>
	N of Rows in Working Data	188
Missing Value Handling	File	
	Definition of Missing	User-defined missing values are treated as missing.
	Cases Used	Statistics are based on all cases with valid data for all variables in the model.

Syntax

```
MIXED T1 BY Week Substrain
Sex

/CRITERIA=DFMETHOD(SAT
TERTHWAITE) CIN(95)
MXITER(100) MXSTEP(10)
SCORING(1)

SINGULAR(0.000000000001)
HCONVERGE(0, ABSOLUTE)
LCONVERGE(0, ABSOLUTE)
PCONVERGE(0.000001,
ABSOLUTE)
/FIXED=Week Substrain Sex
Substrain*Week
Substrain*Sex Sex*Week |
SSTYPE(3)
/METHOD=REML
/REPEATED=Week |
SUBJECT(Number)
COVTYPE(AR1)

/EMMEANS=TABLES(Substra
in) COMPARE ADJ(SIDAK)
/EMMEANS=TABLES(Sex)
COMPARE ADJ(SIDAK)
/EMMEANS=TABLES(Week)
COMPARE ADJ(SIDAK)

/EMMEANS=TABLES(Sex*W
eek) COMPARE(Sex)
ADJ(SIDAK)

/EMMEANS=TABLES(Sex*W
eek) COMPARE(Week)
ADJ(SIDAK)

/EMMEANS=TABLES(Substra
in*Sex) COMPARE(Substrain)
ADJ(SIDAK)
```

		/EMMEANS=TABLES(Substr in*Sex) COMPARE(Sex) ADJ(SIDAK)
		/EMMEANS=TABLES(Substr in*Week) COMPARE(Substrain) ADJ(SIDAK)
		/EMMEANS=TABLES(Substr in*Week) COMPARE(Week) ADJ(SIDAK).
Resources	Processor Time	00:00:00.06
	Elapsed Time	00:00:00.05

Model Dimension^a

		Number of Levels	Covariance Structure	Number of Parameters	Subject Variables	
Fixed Effects	Intercept	1		1		
	Week	3		2		
	Substrain	4		3		
	Sex	2		1		
	Week * Substrain	12		6		
	Substrain * Sex	8		3		
	Week * Sex	6		2		
Repeated Effects	Week	3	First-Order Autoregressiv e	2	Number	
Total		39		20		

Information Criteria^a

-2 Restricted Log Likelihood	1556.782
Akaike's Information Criterion (AIC)	1560.782
Hurvich and Tsai's Criterion (AICC)	1560.855
Bozdogan's Criterion (CAIC)	1569.042
Schwarz's Bayesian Criterion (BIC)	1567.042

The information criteria are displayed in smaller-is-better form.^a

a. Dependent Variable: T1.

Fixed Effects

Type III Tests of Fixed Effects^a

Source	Numerator df	Denominator df	F	Sig.
Intercept	1	92.973	261.634	.000
Week	2	127.193	6.569	.002
Substrain	3	87.951	1.388	.252
Sex	1	95.086	.586	.446
Week * Substrain	6	128.161	2.751	.015
Substrain * Sex	3	103.115	4.150	.008
Week * Sex	2	128.609	.003	.997

a. Dependent Variable: T1.

Covariance Parameters

Estimates of Covariance Parameters^a

Parameter	Estimate	Std. Error
Repeated Measures		
AR1 diagonal	451.167119	49.398952
AR1 rho	.108640	.108742

a. Dependent Variable: T1.

Estimated Marginal Means

1. Substrain

Estimates ^a					
Substrain	Mean	Std. Error	df	95% Confidence Interval	
				Lower Bound	Upper Bound
1BALB/cN	34.554	4.257	152.813	26.144	42.964
2BALB/cJ	29.679	3.303	69.774	23.091	36.267
3C57BL/6N	24.490	3.519	78.046	17.483	31.496
4C57BL/6J	32.796	3.767	69.363	25.282	40.310

a. Dependent Variable: T1.

Pairwise Comparisons ^a							
(I) Substrain	(J) Substrain	Mean Difference (I-J)	Std. Error	df	Sig. ^b	95% Confidence Interval for Difference ^b	
						Lower Bound	
1BALB/cN	2BALB/cJ	4.875	5.321	119.746	.932	-9.361	
	3C57BL/6N	10.065	5.518	123.589	.355	-4.690	
	4C57BL/6J	1.759	5.684	112.480	1.000	-13.465	
2BALB/cJ	1BALB/cN	-4.875	5.321	119.746	.932	-19.111	
	3C57BL/6N	5.190	4.820	74.439	.867	-7.838	
	4C57BL/6J	-3.117	5.010	69.541	.990	-16.683	
3C57BL/6N	1BALB/cN	-10.065	5.518	123.589	.355	-24.819	
	2BALB/cJ	-5.190	4.820	74.439	.867	-18.218	
	4C57BL/6J	-8.306	5.155	73.268	.508	-22.246	
4C57BL/6J	1BALB/cN	-1.759	5.684	112.480	1.000	-16.982	
	2BALB/cJ	3.117	5.010	69.541	.990	-10.450	
	3C57BL/6N	8.306	5.155	73.268	.508	-5.633	

Univariate Tests^a

Numerator df	Denominator df	F	Sig.
3	86.115	1.388	.252

The F tests the effect of Substrain. This test is based on the linearly independent pairwise comparisons among the estimated marginal means.^a

a. Dependent Variable: T1.

2. Sex

Estimates^a

Sex	Mean	Std. Error	df	95% Confidence Interval	
				Lower Bound	Upper Bound
F	31.843	2.243	73.137	27.371	36.314
M	28.917	3.055	107.455	22.861	34.972

a. Dependent Variable: T1.

Pairwise Comparisons^a

(I) Sex	(J) Sex	Mean Difference (I-J)	Std. Error	df	Sig. ^b	95% Confidence Interval for Difference ^b	
						Lower Bound	Upper Bound
F	M	2.926	3.823	95.086	.446	-4.665	10.516
M	F	-2.926	3.823	95.086	.446	-10.516	4.665

Based on estimated marginal means^a

a. Dependent Variable: T1.

b. Adjustment for multiple comparisons: Sidak.

Univariate Tests^a

Numerator df	Denominator df	F	Sig.
1	95.086	.586	.446

The F tests the effect of Sex. This test is based on the linearly independent pairwise comparisons among the estimated marginal means.^a

a. Dependent Variable: T1.

3. Week

Estimates ^a					
Week	Mean	Std. Error	df	95% Confidence Interval	
				Lower Bound	Upper Bound
4	22.506	2.270	166.753	18.025	26.988
6	35.282	3.542	157.697	28.286	42.278
8	33.351	3.138	166.985	27.156	39.546

a. Dependent Variable: T1.

Pairwise Comparisons ^a							
(I) Week	(J) Week	Mean Difference (I-J)	Std. Error	df	Sig. ^c	95% Confidence Interval for Difference ^c	
						Lower Bound	
4	6	-12.775*	4.046	104.729	.006	-22.594	
	8	-10.844*	3.847	168.846	.016	-20.123	
6	4	12.775*	4.046	104.729	.006	2.957	
	8	1.931	4.439	81.275	.962	-8.891	
8	4	10.844*	3.847	168.846	.016	1.565	
	6	-1.931	4.439	81.275	.962	-12.754	

Univariate Tests ^a			
Numerator df	Denominator df	F	Sig.
2	114.535	6.569	.002

The F tests the effect of Week. This test is based on the linearly independent pairwise comparisons among the estimated marginal means.^a

a. Dependent Variable: T1.

4. Sex * Week

Estimates ^a						
Sex	Week	Mean	Std. Error	df	95% Confidence Interval	
					Lower Bound	Upper Bound
F	4	24.036	3.054	166.661	18.006	30.066
	6	36.531	4.046	168.916	28.544	44.519
	8	34.961	3.747	166.781	27.563	42.359
M	4	20.977	3.358	166.828	14.347	27.608
	6	34.033	6.086	145.418	22.004	46.062
	8	31.741	5.066	167.048	21.739	41.742

a. Dependent Variable: T1.

Pairwise Comparisons ^a								
Week	(I) Sex	(J) Sex	Mean Difference (I-J)	Std. Error	df	Sig. ^b	95% Confidence Interval for Difference ^b Lower Bound	
								4
	M	F	-3.059	4.539	166.753	.501	-12.021	
6	F	M	2.498	7.526	154.841	.740	-12.369	
	M	F	-2.498	7.526	154.841	.740	-17.366	
8	F	M	3.220	6.327	166.927	.611	-9.270	
	M	F	-3.220	6.327	166.927	.611	-15.710	

Univariate Tests ^a				
Week	Numerator df	Denominator df	F	Sig.
4	1	166.753	.454	.501
6	1	154.841	.110	.740
8	1	166.927	.259	.611

Each F tests the simple effects of Sex within each level combination of the other effects shown. These tests are based on the linearly independent pairwise comparisons among the estimated marginal means.^a

a. Dependent Variable: T1.

5. Sex * Week

Estimates ^a						
Sex	Week	Mean	Std. Error	df	95% Confidence Interval	
					Lower Bound	Upper Bound
F	4	24.036	3.054	166.661	18.006	30.066
	6	36.531	4.046	168.916	28.544	44.519
	8	34.961	3.747	166.781	27.563	42.359
M	4	20.977	3.358	166.828	14.347	27.608
	6	34.033	6.086	145.418	22.004	46.062
	8	31.741	5.066	167.048	21.739	41.742

a. Dependent Variable: T1.

Pairwise Comparisons ^a							
Sex	(I) Week	(J) Week	Mean Difference (I-J)	Std. Error	df	Sig. ^c	95% Confidence Interval for Difference ^c
							Lower Bound
F	4	6	-12.495*	4.848	106.726	.034	-24.256
		8	-10.925	4.802	168.792	.071	-22.506
	6	4	12.495*	4.848	106.726	.034	.735
		8	1.570	5.230	88.728	.987	-11.158
	8	4	10.925	4.802	168.792	.071	-.656
		6	-1.570	5.230	88.728	.987	-14.299
M	4	6	-13.056	6.773	103.571	.160	-29.493
		8	-10.764	6.056	168.905	.214	-25.369
	6	4	13.056	6.773	103.571	.160	-3.382
		8	2.292	7.445	79.519	.986	-15.867
	8	4	10.764	6.056	168.905	.214	-3.842
		6	-2.292	7.445	79.519	.986	-20.451

Univariate Tests^a

Sex	Numerator df	Denominator df	F	Sig.
F	2	115.967	4.206	.017
M	2	120.564	2.588	.079

Each F tests the simple effects of Week within each level combination of the other effects shown. These tests are based on the linearly independent pairwise comparisons among the estimated marginal means.^a

a. Dependent Variable: T1.

6. Substrain * Sex

Substrain	Sex	Estimates ^a			95% Confidence Interval	
		Mean	Std. Error	df	Lower Bound	Upper Bound
1BALB/cN	F	44.111	3.892	64.725	36.337	51.885
	M	24.998	7.283	168.182	10.620	39.375
2BALB/cJ	F	29.685	3.945	68.745	21.814	37.555
	M	29.674	5.191	74.494	19.331	40.016
3C57BL/6N	F	16.786	4.614	92.675	7.623	25.949
	M	32.193	5.202	73.920	21.827	42.559
4C57BL/6J	F	36.788	5.209	73.700	26.409	47.167
	M	28.803	5.209	73.700	18.424	39.182

a. Dependent Variable: T1.

Pairwise Comparisons^a

Sex	(I) Substrain	(J) Substrain	Mean Difference (I-J)	Std. Error	df	Sig. ^c	95% Confidence Interval for Difference ^c Lower Bound	
F	1BALB/cN	2BALB/cJ	14.426	5.534	66.819	.066	-5.78	
		3C57BL/6N	27.325*	6.037	79.754	.000	11.038	
		4C57BL/6J	7.323	6.490	70.527	.840	-10.245	
	2BALB/cJ	1BALB/cN	-14.426	5.534	66.819	.066	-29.431	
		3C57BL/6N	12.898	6.053	83.114	.198	-3.414	
		4C57BL/6J	-7.104	6.502	73.046	.859	-24.686	
	3C57BL/6N	1BALB/cN	-27.325*	6.037	79.754	.000	-43.612	
		2BALB/cJ	-12.898	6.053	83.114	.198	-29.211	
		4C57BL/6J	-20.002*	6.920	83.112	.029	-38.653	
	4C57BL/6J	1BALB/cN	-7.323	6.490	70.527	.840	-24.891	
		2BALB/cJ	7.104	6.502	73.046	.859	-10.478	
		3C57BL/6N	20.002*	6.920	83.112	.029	1.351	
M	1BALB/cN	2BALB/cJ	-4.676	8.681	157.591	.995	-27.807	
		3C57BL/6N	-7.195	8.742	156.249	.959	-30.491	
		4C57BL/6J	-3.806	8.749	155.605	.999	-27.121	
	2BALB/cJ	1BALB/cN	4.676	8.681	157.591	.995	-18.454	
		3C57BL/6N	-2.519	7.270	76.812	1.000	-22.151	
		4C57BL/6J	.870	7.278	76.557	1.000	-18.787	
	3C57BL/6N	1BALB/cN	7.195	8.742	156.249	.959	-16.100	
		2BALB/cJ	2.519	7.270	76.812	1.000	-17.113	
		4C57BL/6J	3.390	7.299	75.715	.998	-16.329	
	4C57BL/6J	1BALB/cN	3.806	8.749	155.605	.999	-19.509	
		2BALB/cJ	-.870	7.278	76.557	1.000	-20.528	
		3C57BL/6N	-3.390	7.299	75.715	.998	-23.108	

Univariate Tests^a

Sex	Numerator df	Denominator df	F	Sig.
F	3	75.139	7.240	.000
M	3	93.217	.233	.873

Each F tests the simple effects of Substrain within each level combination of the other effects shown. These tests are based on the linearly independent pairwise comparisons among the estimated marginal means.^a

a. Dependent Variable: T1.

7. Substrain * Sex

Estimates ^a						
Substrain	Sex	Mean	Std. Error	df	95% Confidence Interval	
					Lower Bound	Upper Bound
1BALB/cN	F	44.111	3.892	64.725	36.337	51.885
	M	24.998	7.283	168.182	10.620	39.375
2BALB/cJ	F	29.685	3.945	68.745	21.814	37.555
	M	29.674	5.191	74.494	19.331	40.016
3C57BL/6N	F	16.786	4.614	92.675	7.623	25.949
	M	32.193	5.202	73.920	21.827	42.559
4C57BL/6J	F	36.788	5.209	73.700	26.409	47.167
	M	28.803	5.209	73.700	18.424	39.182

a. Dependent Variable: T1.

Pairwise Comparisons ^a								
Substrain	(I) Sex	(J) Sex	Mean Difference (I-J)	Std. Error	df	Sig. ^c	95% Confidence Interval for Difference ^c Lower Bound	
1BALB/cN	F	M	19.113 [*]	7.993	166.723	.018	3.333	
	M	F	-19.113 [*]	7.993	166.723	.018	-34.894	
2BALB/cJ	F	M	.011	6.433	75.136	.999	-12.804	
	M	F	-.011	6.433	75.136	.999	-12.827	
3C57BL/6N	F	M	-15.406 [*]	6.867	85.615	.027	-29.059	
	M	F	15.406 [*]	6.867	85.615	.027	1.754	
4C57BL/6J	F	M	7.985	7.195	78.805	.270	-6.336	
	M	F	-7.985	7.195	78.805	.270	-22.306	

Univariate Tests ^a				
Substrain	Numerator df	Denominator df	F	Sig.
1BALB/cN	1	166.723	5.718	.018
2BALB/cJ	1	75.136	.000	.999
3C57BL/6N	1	85.615	5.033	.027
4C57BL/6J	1	78.805	1.232	.270

Each F tests the simple effects of Sex within each level combination of the other effects shown. These tests are based on the linearly independent pairwise comparisons among the estimated marginal means.^a

a. Dependent Variable: T1.

8. Substrain * Week

Estimates ^a						
Substrain	Week	Mean	Std. Error	df	95% Confidence Interval	
					Lower Bound	Upper Bound
1BALB/cN	4	32.905	4.317	166.727	24.382	41.429
	6	45.291	8.431	118.628	28.597	61.985
	8	25.466	6.396	167.356	12.839	38.093
2BALB/cJ	4	24.895	4.308	166.320	16.390	33.400
	6	36.898	5.659	168.873	25.728	48.069
	8	27.244	5.799	166.714	15.796	38.693
3C57BL/6N	4	11.140	4.750	166.856	1.763	20.517
	6	23.279	6.686	168.445	10.080	36.477
	8	39.050	5.660	166.039	27.874	50.226
4C57BL/6J	4	21.086	4.750	166.828	11.709	30.463
	6	35.659	6.697	168.996	22.439	48.880
	8	41.642	6.717	166.923	28.381	54.902

a. Dependent Variable: T1.

Pairwise Comparisons ^a								
Week	(I) Substrain	(J) Substrain	Mean Difference (I-J)	Std. Error	df	Sig. ^c	95% Confidence Interval for Difference ^c	
							Lower Bound	Upper Bound
4	1BALB/cN	2BALB/cJ	8.011	6.089	166.488	.718	-8.204	24.225
		3C57BL/6N	21.766*	6.419	166.765	.005	4.675	38.856
		4C57BL/6J	11.819	6.419	166.783	.342	-5.271	28.910
	2BALB/cJ	1BALB/cN	-8.011	6.089	166.488	.718	-24.225	8.204
		3C57BL/6N	13.755	6.412	166.586	.184	-3.319	30.829
		4C57BL/6J	3.809	6.412	166.605	.992	-13.265	20.882
	3C57BL/6N	1BALB/cN	-21.766*	6.419	166.765	.005	-38.856	-4.675
		2BALB/cJ	-13.755	6.412	166.586	.184	-30.829	3.319
		4C57BL/6J	-9.946	6.717	166.842	.597	-27.831	7.938
	4C57BL/6J	1BALB/cN	-11.819	6.419	166.783	.342	-28.910	5.271
		2BALB/cJ	-3.809	6.412	166.605	.992	-20.882	13.265
		3C57BL/6N	9.946	6.717	166.842	.597	-7.938	27.831
6	1BALB/cN	2BALB/cJ	8.393	9.736	142.770	.949	-17.583	34.369
		3C57BL/6N	22.012	10.768	144.294	.231	-6.712	50.737

		4C57BL/6J	9.632	10.767	145.926	.939	-19.086	38.349
	2BALB/cJ	1BALB/cN	-8.393	9.736	142.770	.949	-34.369	17.583
		3C57BL/6N	13.620	8.762	168.940	.542	-9.706	36.945
		4C57BL/6J	1.239	8.768	168.966	1.000	-22.102	24.580
	3C57BL/6N	1BALB/cN	-22.012	10.768	144.294	.231	-50.737	6.712
		2BALB/cJ	-13.620	8.762	168.940	.542	-36.945	9.706
		4C57BL/6J	-12.381	9.463	168.884	.723	-37.573	12.812
	4C57BL/6J	1BALB/cN	-9.632	10.767	145.926	.939	-38.349	19.086
		2BALB/cJ	-1.239	8.768	168.966	1.000	-24.580	22.102
		3C57BL/6N	12.381	9.463	168.884	.723	-12.812	37.573
8	1BALB/cN	2BALB/cJ	-1.778	8.505	167.148	1.000	-24.423	20.868
		3C57BL/6N	-13.583	8.400	166.737	.495	-35.950	8.783
		4C57BL/6J	-16.175	9.275	167.135	.405	-40.870	8.519
	2BALB/cJ	1BALB/cN	1.778	8.505	167.148	1.000	-20.868	24.423
		3C57BL/6N	-11.806	8.024	165.967	.604	-33.173	9.561
		4C57BL/6J	-14.398	8.874	166.835	.491	-38.025	9.229
	3C57BL/6N	1BALB/cN	13.583	8.400	166.737	.495	-8.783	35.950
		2BALB/cJ	11.806	8.024	165.967	.604	-9.561	33.173
		4C57BL/6J	-2.592	8.784	166.575	1.000	-25.980	20.796
	4C57BL/6J	1BALB/cN	16.175	9.275	167.135	.405	-8.519	40.870
		2BALB/cJ	14.398	8.874	166.835	.491	-9.229	38.025
		3C57BL/6N	2.592	8.784	166.575	1.000	-20.796	25.980

Based on estimated marginal means^a

*. The mean difference is significant at the .05 level.

a. Dependent Variable: T1.

c. Adjustment for multiple comparisons: Sidak.

Univariate Tests^a

Week	Numerator df	Denominator df	F	Sig.
4	3	166.672	3.949	.009
6	3	153.789	1.524	.211
8	3	166.691	1.739	.161

Each F tests the simple effects of Substrain within each level combination of the other effects shown. These tests are based on the linearly independent pairwise comparisons among the estimated marginal means.^a

a. Dependent Variable: T1.

9. Substrain * Week

Estimates ^a						
Substrain	Week	Mean	Std. Error	df	95% Confidence Interval	
					Lower Bound	Upper Bound
1BALB/cN	4	32.905	4.317	166.727	24.382	41.429
	6	45.291	8.431	118.628	28.597	61.985
	8	25.466	6.396	167.356	12.839	38.093
2BALB/cJ	4	24.895	4.308	166.320	16.390	33.400
	6	36.898	5.659	168.873	25.728	48.069
	8	27.244	5.799	166.714	15.796	38.693
3C57BL/6N	4	11.140	4.750	166.856	1.763	20.517
	6	23.279	6.686	168.445	10.080	36.477
	8	39.050	5.660	166.039	27.874	50.226
4C57BL/6J	4	21.086	4.750	166.828	11.709	30.463
	6	35.659	6.697	168.996	22.439	48.880
	8	41.642	6.717	166.923	28.381	54.902

a. Dependent Variable: T1.

Pairwise Comparisons ^a							
Substrain	(I) Week	(J) Week	Mean Difference (I-J)	Std. Error	df	Sig. ^c	95% Confidence Interval for Difference ^c
							Lower Bound
1BALB/cN	4	6	-12.386	9.013	91.469	.434	-34.308
		8	7.439	7.540	168.800	.693	-10.745
	6	4	12.386	9.013	91.469	.434	-9.536
		8	19.825	9.523	79.184	.117	-3.405
	8	4	-7.439	7.540	168.800	.693	-25.622
		6	-19.825	9.523	79.184	.117	-43.054
2BALB/cJ	4	6	-12.004	6.768	107.866	.219	-28.419
		8	-2.349	7.134	168.590	.983	-19.555
	6	4	12.004	6.768	107.866	.219	-4.412
		8	9.654	7.598	83.260	.502	-8.859
	8	4	2.349	7.134	168.590	.983	-14.856
		6	-9.654	7.598	83.260	.502	-28.167
3C57BL/6N	4	6	-12.139	7.898	110.796	.335	-31.286
		8	-27.910*	7.363	168.998	.001	-45.668

	6	4	12.139	7.898	110.796	.335	-7.008	
		8	-15.771	8.356	94.281	.175	-36.083	
	8	4	27.910*	7.363	168.998	.001	10.152	
		6	15.771	8.356	94.281	.175	-4.541	
4C57BL/6J	4	6	-14.574	7.906	114.943	.190	-33.730	
		8	-20.556*	8.194	168.810	.039	-40.317	
	6	4	14.574	7.906	114.943	.190	-4.583	
		8	-5.982	8.957	80.148	.880	-27.824	
	8	4	20.556*	8.194	168.810	.039	.795	
		6	5.982	8.957	80.148	.880	-15.859	

Univariate Tests^a

Substrain	Numerator df	Denominator df	F	Sig.
1BALB/cN	2	122.798	2.167	.119
2BALB/cJ	2	105.540	1.662	.195
3C57BL/6N	2	126.779	7.184	.001
4C57BL/6J	2	104.932	3.606	.031

Each F tests the simple effects of Week within each level combination of the other effects shown. These tests are based on the linearly independent pairwise comparisons among the estimated marginal means.^a

a. Dependent Variable: T1.

APPENDIX C: SPSS HISTOLOGY ORDINAL REGRESSION ANALYSIS

```

GENLIN Grade (ORDER=DESCENDING) BY Week Substrain Sex (ORDER=DESCENDING)
  /MODEL Week Substrain Sex Substrain*Week Substrain*Sex Sex*Week
  DISTRIBUTION=MULTINOMIAL LINK=CUMLOGIT
  /CRITERIA METHOD=FISHER(1) SCALE=1 COVB=MODEL MAXITERATIONS=100
MAXSTEPHALVING=5
  PCONVERGE=1E-006 (ABSOLUTE) SINGULAR=1E-012 ANALYSISTYPE=3 (WALD)
CILEVEL=95 CITYPE=WALD
  LIKELIHOOD=FULL
  /MISSING CLASSMISSING=EXCLUDE
  /PRINT CPS DESCRIPTIVES MODELINFO FIT SUMMARY SOLUTION.

```

Generalized Linear Models

Notes		
Output Created		17-JAN-2020 12:00:23
Comments		
Input	Data	
	Active Dataset	DataSet1
	Filter	<none>
	Weight	<none>
	Split File	<none>
	N of Rows in Working Data	188
	File	
Missing Value Handling	Definition of Missing	User-defined missing values for factor, subject and within-subject variables are treated as missing.
	Cases Used	Statistics are based on cases with valid data for all variables in the model.
Weight Handling		not applicable

Syntax	<pre> GENLIN Grade (ORDER=DESCENDING) BY Week Substrain Sex (ORDER=DESCENDING) /MODEL Week Substrain Sex Substrain*Week Substrain*Sex Sex*Week DISTRIBUTION=MULTINOMI AL LINK=CUMLOGIT /CRITERIA METHOD=FISHER(1) SCALE=1 COVB=MODEL MAXITERATIONS=100 MAXSTEPHALVING=5 PCONVERGE=1E- 006(ABSOLUTE) SINGULAR=1E-012 ANALYSISTYPE=3(WALD) CILEVEL=95 CITYPE=WALD LIKELIHOOD=FULL /MISSING CLASSMISSING=EXCLUDE /PRINT CPS DESCRIPTIVES MODELINFO FIT SUMMARY SOLUTION. </pre>	
Resources	Processor Time	00:00:00.05
	Elapsed Time	00:00:00.14

Model Information

Dependent Variable	Grade ^a
Probability Distribution	Multinomial
Link Function	Cumulative logit

a. The procedure applies the cumulative link function to the dependent variable values in descending order.

Case Processing Summary

	N	Percent
Included	93	49.5%
Excluded	95	50.5%
Total	188	100.0%

Categorical Variable Information

			N	Percent
Dependent Variable	Grade	3	27	29.0%
		2	26	28.0%
		1	40	43.0%
		Total	93	100.0%
Factor	Week	8	53	57.0%
		4	40	43.0%
		Total	93	100.0%
	Substrain	4C57BL/6J	20	21.5%
		3C57BL/6N	25	26.9%
		2BALB/cJ	25	26.9%
		1BALB/cN	23	24.7%
		Total	93	100.0%
		Sex	M	38
	F		55	59.1%
	Total		93	100.0%

Goodness of Fit^a

	Value	df	Value/df
Deviance	20.898	18	1.161
Scaled Deviance	20.898	18	
Pearson Chi-Square	19.083	18	1.060
Scaled Pearson Chi-Square	19.083	18	
Log Likelihood ^b	-28.293		
Akaike's Information Criterion (AIC)	84.586		
Finite Sample Corrected AIC (AICC)	89.971		
Bayesian Information Criterion (BIC)	120.042		
Consistent AIC (CAIC)	134.042		

Dependent Variable: Grade

Model: (Threshold), Week, Substrain, Sex, Week * Substrain,
Substrain * Sex, Week * Sex^a

- Information criteria are in smaller-is-better form.
- The full log likelihood function is displayed and used in computing information criteria.

Omnibus Test^a

Likelihood Ratio Chi-Square	df	Sig.
62.017	12	.000

Dependent Variable: Grade

Model: (Threshold), Week, Substrain, Sex,
Week * Substrain, Substrain * Sex, Week *
Sex^a

- Compares the fitted model against the thresholds-only model.

Tests of Model Effects

Source	Wald Chi-Square	Type III df	Sig.
Week	32.380	1	.000
Substrain	2.206	3	.531
Sex	.038	1	.845
Week * Substrain	10.650	3	.014
Substrain * Sex	3.816	3	.282
Week * Sex	1.193	1	.275

Dependent Variable: Grade

Model: (Threshold), Week, Substrain, Sex, Week * Substrain, Substrain * Sex, Week * Sex

Parameter Estimates

Parameter	B	Std. Error	95% Wald Confidence Interval		Hypothesis Test		
			Lower	Upper	Wald Chi-Square	df	Sig.
Threshold [Grade=3]	-3.142	.9591	-5.022	-1.263	10.734	1	.001
[Grade=2]	-1.037	.8939	-2.789	.715	1.345	1	.246
[Week=8]	-2.766	1.0249	-4.775	-.757	7.284	1	.007
[Week=4]	0 ^a
[Substrain=4C57BL/6J]	2.233	1.8004	-1.296	5.762	1.538	1	.215
[Substrain=3C57BL/6N]	1.342	1.4307	-1.462	4.146	.880	1	.348
[Substrain=2BALB/cJ]	-.564	1.1448	-2.808	1.680	.243	1	.622
[Substrain=1BALB/cN]	0 ^a
[Sex=M]	.940	1.2008	-1.414	3.293	.612	1	.434
[Sex=F]	0 ^a
[Week=8] * [Substrain=4C57BL/6J]	-3.820	1.7766	-7.302	-.338	4.623	1	.032
[Week=8] * [Substrain=3C57BL/6N]	-2.154	1.4753	-5.045	.738	2.131	1	.144
[Week=8] * [Substrain=2BALB/cJ]	1.028	1.2622	-1.446	3.502	.663	1	.415
[Week=8] * [Substrain=1BALB/cN]	0 ^a
[Week=4] * [Substrain=4C57BL/6J]	0 ^a

[Week=4] * [Substrain=3C57BL/6N]	0 ^a
[Week=4] * [Substrain=2BALB/cJ]	0 ^a
[Week=4] * [Substrain=1BALB/cN]	0 ^a
[Substrain=4C57BL/6J] * [Sex=M]	-2.543	1.6952	-5.865	.780	2.250	1	.134
[Substrain=4C57BL/6J] * [Sex=F]	0 ^a
[Substrain=3C57BL/6N] * [Sex=M]	-2.485	1.4072	-5.243	.273	3.119	1	.077
[Substrain=3C57BL/6N] * [Sex=F]	0 ^a
[Substrain=2BALB/cJ] * [Sex=M]	-1.458	1.2877	-3.982	1.066	1.283	1	.257
[Substrain=2BALB/cJ] * [Sex=F]	0 ^a
[Substrain=1BALB/cN] * [Sex=M]	0 ^a
[Substrain=1BALB/cN] * [Sex=F]	0 ^a
[Week=8] * [Sex=M]	1.147	1.0504	-.911	3.206	1.193	1	.275
[Week=8] * [Sex=F]	0 ^a
[Week=4] * [Sex=M]	0 ^a
[Week=4] * [Sex=F]	0 ^a
(Scale)	1 ^b						

Dependent Variable: Grade

Model: (Threshold), Week, Substrain, Sex, Week * Substrain, Substrain * Sex, Week * Sex

a. Set to zero because this parameter is redundant.

b. Fixed at the displayed value.

PART VI – FUTURE DIRECTIONS AND CONCLUSIONS

Future Use of Murine Model of Cerebral Radiation Necrosis

The research that was performed was meant to be built on by future work aimed at developing new ways of treating radiation necrosis or mitigating the symptoms. In developing our mouse model that uses Precision X-Ray's X-RAD 320, we wanted to be able to develop radiation necrosis in the mouse brain similar to what has been already observed using Leksell's Gamma Knife (84–87), which was developed to as closely as possible produce radiation necrosis similar to what would be observed in humans who develop cerebral necrosis as a consequence of radiation therapy. Using the X-RAD 320, we found that single doses of 80 Gy or 90 Gy were capable of producing sufficient levels of radiation necrosis using our model for analysis purposes. We also established that the sparing effects of fractionation would be minimal for four different fractionation schemes that were carried out using daily weekday fractionation schemes of 5 fractions of 20 Gy, 5 fractions of 18 Gy, 10 fractions of 10 Gy, and 10 fractions of 9 Gy. We further characterized the development of radiation necrosis in four different substrains of mice using both sexes, which should help guide the future choice of mice used in this model.

Mouse Apparatus Positioning Accuracy

The most noticeable limitation of our X-RAD 320 model was that the reproducibility of mice positioning was not as consistent as would be seen in similar Gamma Knife models (84–87) as well as our earlier LINAC based model (122). We used 3D-printed head holders in our mouse apparatus to hold mice in place. However, the reproducibility of positioning using this method is not as consistent as would be obtained using ear bars as was used in our LINAC based model (122). The effects of this lower reproducibility in positioning may be of particular concern in our

model due to the irradiated area, a 0.5×0.5 cm square shaped field, is not 100% entirely in the mouse brain. Shifts particularly in the horizontal direction (left or right) could potentially affect the amount of tissue in the mouse brain that is actually irradiated. This could be of particular interest if doing fractionation work, as slight movement in the position of the irradiated area may add up over time. It is thus suggested that future work with this model move the irradiated field to a more central position in the mouse brain, adjust the size of the irradiated field so that all of it is within the span of the mouse brain, or redesign the mouse holding apparatus to incorporate ear bars to limit motion.

Future Fractionation Studies

As part of this research, four different fractionation schemes were used to irradiate mice: 5 fractions of 20 Gy, 10 fractions of 10 Gy, 5 fractions of 18 Gy, and 10 fractions of 9 Gy. All of these fractionation schemes had single fraction equivalent doses (SFED) that were less than 50 Gy. As previous single fraction irradiations of 50 Gy failed to produce radiation necrosis in the mouse brain within a 26-week span, it was expected none of the fractionation schemes we delivered would result in the development of radiation necrosis. However, the 100 Gy total fractionation schemes (5 fractions of 20 Gy and 10 fractions of 10 Gy) and 90 Gy total fractionation schemes (5 fractions of 18 Gy, and 10 fractions of 9 Gy) produced radiation necrosis volumes most similar to what is observed with 90 Gy and 80 Gy single fraction irradiations respectively as can be seen in Figure 14. Thus, while the linear-quadratic model has proven very useful in the clinical setting, it is not infallible.

We mentioned three different reasons for this lack of sparing in our publication (135): large fraction sizes and total dose in our study, differences between the mouse and human brain,

and potential insufficient time between fractions delivered. The large fraction sizes and total dose in our study is not something that can be easily changed in future studies, with the highly radioresistant nature of the mouse brain requiring high total doses to be able to obtain radiation necrosis, and the required time commitment and repositioning accuracy making more highly fractionated schemes than 10 fractions difficult to carry out. The differences between the mouse and human brain similarly are difficult to account for in our model, with a change from mice to rats or another type of research animal likely requiring a redesign of the irradiation setup seen in Figure 8. However, the potential insufficient time between fractions delivered is a factor that can be easily investigated further and there is cause to want to investigate this. Fractions were delivered every twenty four hours (daily) on weekdays in our study, yet a prior report (121) calculated that the repair halftime for radiation necrosis was 38.1 (6.9–76) hours based on human data, which suggests that perhaps not enough time was available for complete repair between fractions in our study. Furthermore, the fractionation schemes that we used in our study could be classified as hypofractionated schemes, and it is common in clinical practice to deliver hypofractionated schemes fractions as in SBRT every other day (136–138), with it being found in humans that increasing the amount of time between fractions may decrease potential radiation side effects (138–140). Based on this data, further investigation into whether increasing the time between fractions would reduce the level of radiation necrosis in mice may be valuable. However, it is recommended that the dose per fraction should not be excessively high due to a previous study (85) using a Gamma Knife delivering three fractions of 20 Gy to the 50% isodose, with fractions being delivered on Monday, Wednesday, and Friday, with no sparing of radiation necrosis observed. At the maximum

point of dose in the Gamma Knife's dose distribution, this roughly is equivalent to three fractions of 40 Gy with the X-Rad 320. It is suggested that future fractionation studies that are analyzing the effect of time in between fractions use dose per fraction values more in line with what our own study used (9-20 Gy per fraction) or lower.

The days that irradiations were carried out on is also an important factor that should be considered. In our fractionation study, we irradiated on weekdays only. Our justification was that most clinics treat patients only on weekdays, so we wanted to mimic as closely as possible what is done in the clinic. However, the clinical reasoning for treating patients on weekdays is not based on science but of convenience regarding people's schedules. For a preclinical fractionation study, it is more scientifically correct to deliver all fractions sequentially regardless if the day of delivery of a fraction falls on a weekday or not.

Future Mouse Age and Sex Studies

8–9 week old mice were used in all of the published data presented as part of this research. In spite of this, age is suspected to be a factor that may have a significant effect on the development of radiation necrosis, as human data has shown that individuals are more radiosensitive when they are younger (*141*). In our substrain and sex experiments with 8-9 week mice, we found that sex was not a statistically significant factor regarding radiation necrosis development, which contradicts human data where females are more radiosensitive than males (*142–144*).

Furthermore, it has been found that irradiation to the young mouse brain impairs white matter growth more in female than in male C57BL/6J mice (*145*). Based on this, there may be value in a similar study based off our substrain and sex experimental methodology for age and sex. One potential setup has mice of both sexes and ages 1, 2, 4, 10, and 18 months old corresponding in people to pediatric, teenagers, young adults, middle-aged adults, and older adults respectively

(146). These ten combined groups of mice could be irradiated to test for significant differences in regard to both sex and age on the development of radiation necrosis.

Chronoradiosensitivity Mouse Study

One study found that the time of the day that mice were irradiated during determined their radiation sensitivity when looking at LD_{50/30} data (77). Mice were found to be most radiosensitive during midday (11am-1pm), followed by afternoon (1pm-5:15pm), with mice during the morning (9am-11am) being found to be least radiosensitive. Statistically speaking, mice that were irradiated during the morning were found to be more radioresistant than mice irradiated at either other time (Kaplan-Meier $P \leq 0.019$) (77). Most reviewed mouse models did not consider the effects the time of day would have on their radionecrosis development including our own model (112, 135). As a result, there may be value in testing for the chronoradiosensitivity of mice using a model of radiation necrosis such as ours. A potential study would match the methodology of the previous study of interest (77), with both sexes of C57BL/6J mice being irradiated at the three timepoints mentioned. Such a study would verify if radiation necrosis response is dependent on the time of day of irradiations, which would help reduce the fluctuation in study results and make future studies more precise.

Experimental Parameters and Reproducibility in Science

A part of this research focused on how the strain and sex of mice impacted the development of radiation necrosis. The strain of mice was found to be statistically significant with BALB/c mice developing radiation necrosis faster and developing larger lesion sizes than C57BL/6 mice, while the substrain was found to be of lesser importance, with BALB/cN mice developing radiation

necrosis slightly faster than BALB/cJ mice. Sex was not found to be a statistically significant parameter. The initial motivation of this research stems from unpublished findings that the BALB/cJ mice appeared to develop radiation necrosis faster than BALB/cN mice, although the results of our study appear to contradict this.

Our findings confirm the need to have a well characterized model and be thorough in explaining how an experiment is setup. Many decisions go into model design, such as the choice of the particle type, energy of particle, dose delivered, dose rate, animal type, fractionation scheme, time between fractions, etc. How each of these decisions may affect the experimental result obtained needs to be considered as each combination of these choices represent a model. Trying to compare models which are not the same either intentionally or otherwise is likely a contributing factor to the current issue of irreproducibility in science (*147–150*), which may be a reason for issues such as a reduction in development projects in Phase II trials (*149*). While a goal of this research was to get preclinical labs to pay attention to the type of mice that they are using, it is also the hope of this research that groups will be more meticulous in how they design and document their experimental setup to improve reproducibility in science.

Radiation Necrosis Treatment Development

The ultimate goal of radiation necrosis research should be the development of new ways of either preventing radiation necrosis from developing or mitigating the symptoms of radiation necrosis without the treatment itself having side effects that require patients to come off the treatment. Future development of such treatments is necessary as the current ways of dealing with radiation necrosis are not adequate, with corticosteroids having adverse chronic side effects with the symptoms of radiation necrosis reemerging if patients come off the corticosteroids (*88, 90, 91*), hyperbaric oxygen therapy having its own unwanted side effects (*92*), and surgical removal of

the radiation necrosis often not being an option, especially in elderly patients with multiple comorbidities. As such, the discovery of a drug that could reduce the development of radiation necrosis while not protecting the tumor that is irradiated during radiation therapy would greatly improve patient care. In particular, our group continues to look for a chemical radioprotector such as Amifostine, which has been shown to reduce the side effects associated with radiation therapy without protecting tumors in head and neck cases (69). As our research has setup a well characterized mouse model capable of studying radiation necrosis, our mouse model is capable of testing drugs for their efficacy in impairing radiation necrosis development. If a drug is found to be effective, the drug would likely be tested in another preclinical animal model such as in a minipig before moving onto human clinical trials.

Radiation Necrosis: A Consequence of Radiation Therapy's Success

The death rate associated with cancer has fallen as techniques for diagnosing and treating the disease have improved. The American Cancer Society has found that the cancer death rate has fallen by about 27% from 1991 to 2016 (151). As the death rate of cancer decreases though, the number of patients who will live long enough to experience the side effects of radiation therapy will inevitably increase. This necessitates improving the treatments that are available for these patients, which is especially important for radiation necrosis, with the current treatment options being inadequate.

Our lab will continue to improve our murine model of radiation necrosis as well as continue our search for treatments that can either decrease the volume and severity of radiation necrosis that develops or manages the symptoms without having severe deleterious side effects that necessitates taking patients off the treatment. Further success in the area of inhibiting and managing radiation necrosis will mean that the prolonged life of cancer patients that has been

exhibited will be accompanied by a greater quality of life. As we continue with our research, it is expected that further problems will arise as we develop solutions for the problems of today. However, multiple labs with a wide range of expertise are currently studying radiation necrosis, and they are up to the task of addressing whatever challenges appear.

REFERENCES

1. Jaffray DA, Gospodarowicz MK. Radiation Therapy for Cancer. In: Gelband H, Jha P, Sankaranarayanan R, Horton S, editors. *Cancer: Disease Control Priorities, Third Edition (Volume 3)*. Washington (DC): The International Bank for Reconstruction and Development / The World Bank; 2015.
2. Siegel RL, Miller KD, Jemal A. Cancer statistics, 2020. *CA Cancer J Clin*. 2020; 70(1):7–30.
3. Merchant TE, Pollack IF, Loeffler JS. Brain tumors across the age spectrum: biology, therapy, and late effects. *Semin Radiat Oncol*. 2010; 20(1):58–66.
4. DeSantis CE, Lin CC, Mariotto AB, Siegel RL, Stein KD, Kramer JL, et al. Cancer treatment and survivorship statistics, 2014. *CA Cancer J Clin*. 2014; 64(4):252–71.
5. Siegel RL, Miller KD, Jemal A. Cancer Statistics, 2017. *CA Cancer J Clin*. 2017; 67(1):7–30.
6. *Understanding Brain Tumors: The Basics*. Roswell Park Comprehensive Cancer Center.
7. Dolecek TA, Propp JM, Stroup NE, Kruchko C. CBTRUS statistical report: primary brain and central nervous system tumors diagnosed in the United States in 2005-2009. *Neuro-Oncol*. 2012; 14 Suppl 5:v1-49.
8. Ostrom QT, Gittleman H, Farah P, Ondracek A, Chen Y, Wolinsky Y, et al. CBTRUS statistical report: Primary brain and central nervous system tumors diagnosed in the United States in 2006-2010. *Neuro-Oncol*. 2013; 15 Suppl 2:ii1-56.
9. Koshy M, Villano JL, Dolecek TA, Howard A, Mahmood U, Chmura SJ, et al. Improved survival time trends for glioblastoma using the SEER 17 population-based registries. *J Neurooncol*. 2012; 107(1):207–12.
10. Ostrom QT, Gittleman H, Xu J, Kromer C, Wolinsky Y, Kruchko C, et al. CBTRUS Statistical Report: Primary Brain and Other Central Nervous System Tumors Diagnosed in the United States in 2009–2013. *Neuro-Oncol*. Oxford Academic; 2016; 18(suppl_5):v1–75.
11. Phoenix TN, Patmore DM, Boop S, Boulos N, Jacus MO, Patel YT, et al. Medulloblastoma Genotype Dictates Blood Brain Barrier Phenotype. *Cancer Cell*. 2016; 29(4):508–22.
12. Gerstner ER, Fine RL. Increased permeability of the blood-brain barrier to chemotherapy in metastatic brain tumors: establishing a treatment paradigm. *J Clin Oncol Off J Am Soc Clin Oncol*. 2007; 25(16):2306–12.
13. Aldape K, Brindle KM, Chesler L, Chopra R, Gajjar A, Gilbert MR, et al. Challenges to curing primary brain tumours. *Nat Rev Clin Oncol*. 2019; 16(8):509–20.
14. Pollock RE, Morton DL. *Principles of Surgical Oncology*. Holl-Frei Cancer Med 6th Ed. BC Decker; 2003.
15. Dare AJ, Anderson BO, Sullivan R, Pramesh CS, Andre I, Adewole IF, et al. Surgical Services for Cancer Care. In: Gelband H, Jha P, Sankaranarayanan R, Horton S, editors. *Cancer: Disease Control Priorities, Third Edition (Volume 3)*. Washington (DC): The International Bank for Reconstruction and Development / The World Bank; 2015.
16. Lara-Velazquez M, Al-Kharboosh R, Jeanneret S, Vazquez-Ramos C, Mahato D, Tavanaiepour D, et al. Advances in Brain Tumor Surgery for Glioblastoma in Adults. *Brain Sci*. 2017; 7(12).
17. De la Garza-Ramos R, Kerezoudis P, Tamargo RJ, Brem H, Huang J, Bydon M. Surgical complications following malignant brain tumor surgery: An analysis of 2002–2011 data. *Clin Neurol Neurosurg*. 2016; 140:6–10.

18. Voegeli M, Wicki A. [Neoadjuvant, adjuvant and palliative systemic therapy of colorectal cancer]. *Ther Umsch Rev Ther*. 2018; 75(10):622–6.
19. Bae WK, Lee HJ, Park SH, Kim JH, Kim HJ, Maeng CH, et al. Comparative effectiveness of palliative chemotherapy versus neoadjuvant chemotherapy followed by radical cystectomy versus cystectomy followed by adjuvant chemotherapy versus cystectomy for regional node-positive bladder cancer: A retrospective analysis: KCSG GU 17-03. *Cancer Med*. 2019; 8(12):5431–7.
20. Herreros-Villanueva M, Hijona E, Cosme A, Bujanda L. Adjuvant and neoadjuvant treatment in pancreatic cancer. *World J Gastroenterol WJG*. 2012; 18(14):1565–72.
21. Jayachandran D, Rundell AE, Hannemann RE, Vik TA, Ramkrishna D. Optimal Chemotherapy for Leukemia: A Model-Based Strategy for Individualized Treatment. *PLoS ONE*. 2014; 9(10).
22. Zappa C, Mousa SA. Non-small cell lung cancer: current treatment and future advances. *Transl Lung Cancer Res*. 2016; 5(3):288–300.
23. Nounou MI, ElAmrawy F, Ahmed N, Abdelraouf K, Goda S, Syed-Sha-Qhattal H. Breast Cancer: Conventional Diagnosis and Treatment Modalities and Recent Patents and Technologies. *Breast Cancer Basic Clin Res*. 2015; 9(Suppl 2):17–34.
24. Hajatdoost L, Sedaghat K, Walker EJ, Thomas J, Kosari S. Chemotherapy in Pancreatic Cancer: A Systematic Review. *Medicina (Mex)*. 2018; 54(3).
25. Weller M. [Chemotherapy for brain tumors in adult patients]. *Nervenarzt*. 2008; 79(2):231–41.
26. Minniti G, Muni R, Lanzetta G, Marchetti P, Enrici RM. Chemotherapy for glioblastoma: current treatment and future perspectives for cytotoxic and targeted agents. *Anticancer Res*. 2009; 29(12):5171–84.
27. Wang Z, Yang G, Zhang Y-Y, Yao Y, Dong L-H. A comparison between oral chemotherapy combined with radiotherapy and radiotherapy for newly diagnosed glioblastoma. *Medicine (Baltimore)*. 2017; 96(44).
28. Thomas A, Noël G. Medulloblastoma: optimizing care with a multidisciplinary approach. *J Multidiscip Healthc*. 2019; 12:335–47.
29. Kim SK, Kim JW, Kim YH, Kim TM, Lee S-H, Park C-K. The Role of Chemotherapy in Anaplastic Astrocytoma Patients. *J Korean Neurosurg Soc*. 2012; 51(4):199–202.
30. Nurgali K, Jagoe RT, Abalo R. Editorial: Adverse Effects of Cancer Chemotherapy: Anything New to Improve Tolerance and Reduce Sequelae? *Front Pharmacol*. 2018; 9.
31. Frenkel M. Refusing Treatment. *The Oncologist*. 2013; 18(5):634–6.
32. Desouky O, Ding N, Zhou G. Targeted and non-targeted effects of ionizing radiation. *J Radiat Res Appl Sci*. 2015; 8(2):247–54.
33. Mehta S, Suhag V, Semwal M, Sharma N. Radiotherapy: Basic Concepts and Recent Advances. *Med J Armed Forces India*. 2010; 66(2):158–62.
34. Baskar R, Lee KA, Yeo R, Yeoh K-W. Cancer and Radiation Therapy: Current Advances and Future Directions. *Int J Med Sci*. 2012; 9(3):193–9.
35. Nahum AE. The radiobiology of hypofractionation. *Clin Oncol R Coll Radiol G B*. 2015; 27(5):260–9.
36. Withers HR. The Four R's of Radiotherapy. In: Lett JT, Adler H, editors. *Advances in Radiation Biology*. Elsevier; 1975; bk. 5, pp. 241–71.
37. Brenner DJ. The linear-quadratic model is an appropriate methodology for determining isoeffective doses at large doses per fraction. *Semin Radiat Oncol*. 2008; 18(4):234–9.

38. Greene-Schloesser D, Robbins ME, Peiffer AM, Shaw EG, Wheeler KT, Chan MD. Radiation-induced brain injury: A review. *Front Oncol.* 2012; 2:73.
39. Hatiboglu MA, Wildrick DM, Sawaya R. The role of surgical resection in patients with brain metastases. *ecancermedicalsecience.* 2013; 7.
40. Markesbery WR, Brooks WH, Gupta GD, Young AB. Treatment for patients with cerebral metastases. *Arch Neurol.* 1978; 35(11):754–6.
41. Egawa S, Tukiyaama I, Akine Y, Kajiura Y, Yanagawa S, Watai K, et al. Radiotherapy of brain metastases. *Int J Radiat Oncol Biol Phys.* 1986; 12(9):1621–5.
42. Horton J, Baxter DH, Olson KB. The management of metastases to the brain by irradiation and corticosteroids. *Am J Roentgenol Radium Ther Nucl Med.* 1971; 111(2):334–6.
43. Murray KJ, Scott C, Greenberg HM, Emami B, Seider M, Vora NL, et al. A randomized phase III study of accelerated hyperfractionation versus standard in patients with unresected brain metastases: a report of the Radiation Therapy Oncology Group (RTOG) 9104. *Int J Radiat Oncol Biol Phys.* 1997; 39(3):571–4.
44. Rades D, Haatanen T, Schild SE, Dunst J. Dose escalation beyond 30 grays in 10 fractions for patients with multiple brain metastases. *Cancer.* 2007; 110(6):1345–50.
45. Walker MD, Strike TA, Sheline GE. An analysis of dose-effect relationship in the radiotherapy of malignant gliomas. *Int J Radiat Oncol.* 1979; 5(10):1725–31.
46. McMahon SJ, Prise KM. Mechanistic Modelling of Radiation Responses. *Cancers. Multidisciplinary Digital Publishing Institute;* 2019; 11(2):205.
47. Tofilon PJ, Fike JR. The radioresponse of the central nervous system: a dynamic process. *Radiat Res.* 2000; 153(4):357–70.
48. Balentova S, Adamkov M. Molecular, Cellular and Functional Effects of Radiation-Induced Brain Injury: A Review. *Int J Mol Sci.* 2015; 16(11):27796–815.
49. Van Ryckeghem F. Corticosteroids, the oldest agent in the prevention of chemotherapy-induced nausea and vomiting: What about the guidelines? *J Transl Intern Med.* 2016; 4(1):46–51.
50. Medicines to Prevent and Treat Nausea and Vomiting | American Cancer Society.
51. Giglio P, Gilbert MR. Cerebral Radiation Necrosis. *The Neurologist.* 2003; 9(4):180–188.
52. Verma N, Cowperthwaite MC, Burnett MG, Markey MK. Differentiating tumor recurrence from treatment necrosis: a review of neuro-oncologic imaging strategies. *Neuro-Oncol.* 2013; 15(5):515–34.
53. Buboltz JB, Dulebohn SC. Hyperbaric, Brain Radiation Necrosis. In: *StatPearls. Treasure Island (FL): StatPearls Publishing;* 2018.
54. Furuse M, Nonoguchi N, Kawabata S, Miyatake S-I, Kuroiwa T. Delayed brain radiation necrosis: pathological review and new molecular targets for treatment. *Med Mol Morphol.* 2015; 48(4):183–90.
55. Ruben JD, Dally M, Bailey M, Smith R, McLean CA, Fedele P. Cerebral radiation necrosis: incidence, outcomes, and risk factors with emphasis on radiation parameters and chemotherapy. *Int J Radiat Oncol Biol Phys.* 2006; 65(2):499–508.
56. Zhuang H, Zheng Y, Wang J, Chang JY, Wang X, Yuan Z, et al. Analysis of risk and predictors of brain radiation necrosis after radiosurgery. *Oncotarget.* 2015; 7(7):7773–9.
57. Patel U, Patel A, Cobb C, Benkers T, Vermeulen S. The management of brain necrosis as a result of SRS treatment for intra-cranial tumors. *Transl Cancer Res.* 2014; 3(4):373–82.
58. Jagannathan J, Petit JH, Balsara K, Hudes R, Chin LS. Long-term survival after gamma knife radiosurgery for primary and metastatic brain tumors. *Am J Clin Oncol.* 2004; 27(5):441–4.

59. Murovic JA, Chang SD. The Pathophysiology of Cerebral Radiation Necrosis and the Role of Laser Interstitial Thermal Therapy. *World Neurosurg.* 2015; 83(1):23–6.
60. Vellayappan B, Tan CL, Yong C, Khor LK, Koh WY, Yeo TT, et al. Diagnosis and Management of Radiation Necrosis in Patients With Brain Metastases. *Front Oncol.* 2018; 8.
61. Mehrabian H, Desmond KL, Soliman H, Sahgal A, Stanisz GJ. Differentiation between Radiation Necrosis and Tumor Progression Using Chemical Exchange Saturation Transfer. *Clin Cancer Res. American Association for Cancer Research;* 2017; 23(14):3667–75.
62. Chambless LB, Angel FB, Abel TW, Xia F, Weaver KD. Delayed cerebral radiation necrosis following treatment for a plasmacytoma of the skull. *Surg Neurol Int.* 2010; 1.
63. Xu J-L, Li Y-L, Lian J-M, Dou S, Yan F-S, Wu H, et al. Distinction between postoperative recurrent glioma and radiation injury using MR diffusion tensor imaging. *Neuroradiology.* 2010; 52(12):1193–9.
64. Zeng Q-S, Li C-F, Liu H, Zhen J-H, Feng D-C. Distinction between recurrent glioma and radiation injury using magnetic resonance spectroscopy in combination with diffusion-weighted imaging. *Int J Radiat Oncol Biol Phys.* 2007; 68(1):151–8.
65. Kashimura H, Inoue T, Beppu T, Ogasawara K, Ogawa A. Diffusion tensor imaging for differentiation of recurrent brain tumor and radiation necrosis after radiotherapy--three case reports. *Clin Neurol Neurosurg.* 2007; 109(1):106–10.
66. Sundgren PC, Fan X, Weybright P, Welsh RC, Carlos RC, Petrou M, et al. Differentiation of recurrent brain tumor versus radiation injury using diffusion tensor imaging in patients with new contrast-enhancing lesions. *Magn Reson Imaging.* 2006; 24(9):1131–42.
67. Weybright P, Sundgren PC, Maly P, Hassan DG, Nan B, Rohrer S, et al. Differentiation between brain tumor recurrence and radiation injury using MR spectroscopy. *AJR Am J Roentgenol.* 2005; 185(6):1471–6.
68. Smith EA, Carlos RC, Junck LR, Tsien CI, Elias A, Sundgren PC. Developing a clinical decision model: MR spectroscopy to differentiate between recurrent tumor and radiation change in patients with new contrast-enhancing lesions. *AJR Am J Roentgenol.* 2009; 192(2):W45-52.
69. Gu J, Zhu S, Li X, Wu H, Li Y, Hua F. Effect of Amifostine in Head and Neck Cancer Patients Treated with Radiotherapy: A Systematic Review and Meta-Analysis Based on Randomized Controlled Trials. *PLoS ONE.* 2014; 9(5).
70. Hranitzky EB, Almond PR, Suit HD, Moore EB. A Cesium-137 Irradiator for Small Laboratory Animals. *Radiology. Radiological Society of North America;* 1973; 107(3):641–4.
71. Moravan MJ, Olschowka JA, Williams JP, O'Banion MK. Cranial Irradiation Leads to Acute and Persistent Neuroinflammation with Delayed Increases in T-Cell Infiltration and CD11c Expression in C57BL/6 Mouse Brain. *Radiat Res.* 2011; 176(4):459–73.
72. Harris DL, Yamaguchi T, Hamrah P. A Novel Murine Model of Radiation Keratopathy. *Invest Ophthalmol Vis Sci. The Association for Research in Vision and Ophthalmology;* 2018; 59(10):3889–96.
73. Ford EC, Achanta P, Purger D, Armour M, Reyes J, Fong J, et al. Localized CT-Guided Irradiation Inhibits Neurogenesis in Specific Regions of the Adult Mouse Brain. *Radiat Res.* 2011; 175(6):774–83.
74. Arndt CD, Wang IZ, Saito NG, Podgorsak MB. Dosimetric Calibration and Characterization for Experimental Mouse Thoracic Irradiation Using Orthovoltage X Rays. *Radiat Res.* 2011; 175(6):784–9.

75. Azimi R, Alaei P, Spezi E, Hui SK. Characterization of an orthovoltage biological irradiator used for radiobiological research. *J Radiat Res (Tokyo)*. 2015; 56(3):485–92.
76. Mole RH. The LD50 for uniform low LET irradiation of man. *Br J Radiol*. 1984; 57(677):355–69.
77. Plett PA, Sampson CH, Chua HL, Joshi M, Booth C, Gough A, et al. Establishing a murine model of the Hematopoietic Syndrome of the Acute Radiation Syndrome. *Health Phys*. 2012; 103(4):343–55.
78. Fujita S, Kato H, Schull WJ. The LD50 associated with exposure to the atomic bombing of Hiroshima and Nagasaki. *J Radiat Res (Tokyo)*. 1991; 32 Suppl:154–61.
79. Shakhov AN, Singh VK, Bone F, Cheney A, Kononov Y, Krasnov P, et al. Prevention and Mitigation of Acute Radiation Syndrome in Mice by Synthetic Lipopeptide Agonists of Toll-Like Receptor 2 (TLR2). *PLOS ONE*. Public Library of Science; 2012; 7(3):e33044.
80. Alexander P, Connell DI. Shortening of the life span of mice by irradiation with x-rays and treatment with radiomimetic chemicals. *Radiat Res*. 1960; 12:38–48.
81. Srinivasan V, Doctrow S, Singh VK, Whitnall MH. Evaluation of EUK-189, a synthetic superoxide dismutase/catalase mimetic as a radiation countermeasure. *Immunopharmacol Immunotoxicol*. 2008; 30(2):271–90.
82. Ghosh SP, Kulkarni S, Hieber K, Toles R, Romanyukha L, Kao T-C, et al. Gamma-tocotrienol, a tocol antioxidant as a potent radioprotector. *Int J Radiat Biol*. 2009; 85(7):598–606.
83. Mak IW, Evaniew N, Ghert M. Lost in translation: animal models and clinical trials in cancer treatment. *Am J Transl Res*. 2014; 6(2):114–8.
84. Perez-Torres CJ, Yuan L, Schmidt RE, Rich KM, Drzymala RE, Hallahan DE, et al. Specificity of Vascular Endothelial Growth Factor Treatment for Radiation Necrosis. *Radiother Oncol J Eur Soc Ther Radiol Oncol*. 2015; 117(2):382–5.
85. Jiang X, Yuan L, Engelbach JA, Cates J, Perez-Torres CJ, Gao F, et al. A Gamma-Knife-Enabled Mouse Model of Cerebral Single-Hemisphere Delayed Radiation Necrosis. *PLOS ONE*. 2015; 10(10):e0139596.
86. Perez-Torres CJ, Engelbach JA, Cates J, Thotala D, Yuan L, Schmidt RE, et al. Toward Distinguishing Recurrent Tumor from Radiation Necrosis: DWI and MTC in a Gamma Knife® Irradiated Mouse Glioma Model. *Int J Radiat Oncol Biol Phys*. 2014; 90(2):446–53.
87. Constanzo J, Masson-Côté L, Tremblay L, Fouquet JP, Sarret P, Geha S, et al. Understanding the continuum of radionecrosis and vascular disorders in the brain following gamma knife irradiation: An MRI study. *Magn Reson Med*. 2017; 78(4):1420–31.
88. Song YP, Colaco RJ. Radiation Necrosis – A Growing Problem in a Case of Brain Metastases Following Whole Brain Radiotherapy and Stereotactic Radiosurgery. *Cureus*. 2018; 10(1):e2037.
89. Powell M. Clinical trial for first-ever treatment of radiation necrosis. 2017.
90. Buchman AL. Side effects of corticosteroid therapy. *J Clin Gastroenterol*. 2001; 33(4):289–94.
91. Goette DK, Odom RB. Adverse effects of corticosteroids. *Cutis*. 1979; 23(4):477–87.
92. Meyers L. Radiation Necrosis and Hyperbaric Oxygen Therapy. *WoundSource*. 2013.
93. Du Four S, Wilgenhof S, Duerinck J, Michotte A, Binst AV, Ridder MD, et al. Radiation necrosis of the brain in melanoma patients successfully treated with ipilimumab, three case studies. *Eur J Cancer*. 2012; 48(16):3045–51.

94. Jiang X, Engelbach JA, Yuan L, Cates J, Gao F, Drzymala RE, et al. Anti-VEGF antibodies mitigate the development of radiation necrosis in mouse brain. *Clin Cancer Res Off J Am Assoc Cancer Res.* 2014; 20(10):2695–702.
95. Lindquist C. Gamma knife radiosurgery. *Semin Radiat Oncol.* 1995; 5(3):197–202.
96. Brezovich IA, Wu X, Duan J, Popple RA, Shen S, Benhabib S, et al. End-to-end test of spatial accuracy in Gamma Knife treatments for trigeminal neuralgia a). *Med Phys.* 2014; 41(11):111703.
97. Champoudry J, Dorenlot A. 53 - Evaluation of geometric uncertainties and planning target volume (PTV) margin in hypo-fractionated radiosurgery using Gamma Knife Extend system. *Phys Med.* 2015; 31:e43.
98. Ohri N, Dicker AP, Showalter TN. Late toxicity rates following definitive radiotherapy for prostate cancer. *Can J Urol.* 2012; 19(4):6373–80.
99. Kulkarni S, Wang TC, Guha C. Stromal Progenitor Cells in Mitigation of Non-Hematopoietic Radiation Injuries. *Curr Pathobiol Rep.* 2016; 4(4):221–30.
100. Yang L, Yang J, Li G, Li Y, Wu R, Cheng J, et al. Pathophysiological Responses in Rat and Mouse Models of Radiation-Induced Brain Injury. *Mol Neurobiol.* 2017; 54(2):1022–32.
101. Mesbahi A, Zakariaee S-S. Effect of anode angle on photon beam spectra and depth dose characteristics for X-RAD320 orthovoltage unit. *Rep Pract Oncol Radiother.* 2013; 18(3):148–52.
102. Hartl BA, Ma HSW, Hansen KS, Perks J, Kent MS, Fragoso RC, et al. The effect of radiation dose on the onset and progression of radiation-induced brain necrosis in the rat model. *Int J Radiat Biol.* 2017; 93(7):676–82.
103. Perez-Torres CJ, Yuan L, Schmidt RE, Rich KM, Ackerman JJ, Garbow JR. Perilesional edema in radiation necrosis reflects axonal degeneration. *Radiat Oncol Lond Engl.* 2015; 10.
104. Perry A, Schmidt RE. Cancer therapy-associated CNS neuropathology: an update and review of the literature. *Acta Neuropathol (Berl).* 2006; 111(3):197–212.
105. Ngen EJ, Wang L, Gandhi N, Kato Y, Armour M, Zhu W, et al. A preclinical murine model for the early detection of radiation-induced brain injury using magnetic resonance imaging and behavioral tests for learning and memory: with applications for the evaluation of possible stem cell imaging agents and therapies. *J Neurooncol.* 2016; 128(2):225–33.
106. Constanzo J, Dumont M, Lebel R, Tremblay L, Whittingstall K, Masson-Côté L, et al. Diffusion MRI monitoring of specific structures in the irradiated rat brain. *Magn Reson Med.* 2018; 80(4):1614–25.
107. Morgan TM, Zaenger D, Switchenko JM, Eaton BR, Crocker IR, Ali AN, et al. Fractionated Radiotherapy Is Associated with Lower Rates of Treatment-Related Edema than Stereotactic Radiosurgery in Magnetic Resonance Imaging-Defined Meningiomas. *World Neurosurg.* 2019; 121:e640–6.
108. Cozzarini C, Fiorino C, Deantoni C, Briganti A, Fodor A, La Macchia M, et al. Higher-than-expected severe (Grade 3-4) late urinary toxicity after postprostatectomy hypofractionated radiotherapy: a single-institution analysis of 1176 patients. *Eur Urol.* 2014; 66(6):1024–30.
109. Fiorino C, Cozzarini C, Rancati T, Briganti A, Cattaneo GM, Mangili P, et al. Modelling the impact of fractionation on late urinary toxicity after postprostatectomy radiation therapy. *Int J Radiat Oncol Biol Phys.* 2014; 90(5):1250–7.
110. Kirkpatrick JP, Soltys SG, Lo SS, Beal K, Shrieve DC, Brown PD. The radiosurgery fractionation quandary: single fraction or hypofractionation? *Neuro-Oncol.* 2017; 19(2):ii38–49.

111. Kondo N, Sakurai Y, Takata T, Takai N, Nakagawa Y, Tanaka H, et al. Localized radiation necrosis model in mouse brain using proton ion beams. *Appl Radiat Isot Data Instrum Methods Use Agric Ind Med*. 2015; 106:242–6.
112. Boria AJ, Perez-Torres CJ. Influence of Dose Uniformity when Replicating a Gamma Knife Mouse Model of Radiation Necrosis with a Preclinical Irradiator. *Radiat Res*. 2019; 191(4):352–9.
113. Fowler JF. The linear-quadratic formula and progress in fractionated radiotherapy. *Br J Radiol*. 1989; 62(740):679–94.
114. Park S, Urm S, Cho H. Analysis of Biologically Equivalent Dose of Stereotactic Body Radiotherapy for Primary and Metastatic Lung Tumors. *Cancer Res Treat Off J Korean Cancer Assoc*. 2014; 46(4):403–10.
115. Jones B, Dale RG, Deehan C, Hopkins KI, Morgan DA. The role of biologically effective dose (BED) in clinical oncology. *Clin Oncol R Coll Radiol G B*. 2001; 13(2):71–81.
116. Lee C-C, Yen C-P, Xu Z, Schlesinger D, Sheehan J. Large intracranial metastatic tumors treated by Gamma Knife surgery: outcomes and prognostic factors. *J Neurosurg*. 2014; 120(1):52–9.
117. Urbanski K, Gasinska A, Pudelek J, Fowler JF, Lind B, Brahme A. Biologically effective doses in radiotherapy of cervical carcinoma*. *Neoplasma*. 2004; 51(3):228–38.
118. Greene-Schloesser DM, Kooshki M, Payne V, Jr RBD, Wheeler KT, Metheny-Barlow LJ, et al. Cellular response of the rat brain to single doses of ^{137}Cs γ rays does not predict its response to prolonged ‘biologically equivalent’ fractionated doses. *Int J Radiat Biol*. 2014; 90(9):790–8.
119. Baardwijk A van, Tomé WA, Elmtpt W van, Bentzen SM, Reymen B, Wanders R, et al. Is high-dose stereotactic body radiotherapy (SBRT) for stage I non-small cell lung cancer (NSCLC) overkill? A systematic review. *Radiother Oncol*. 2012; 105(2):145–9.
120. Daly ME, Perks JR, Chen AM. Patterns-of-Care for Thoracic Stereotactic Body Radiotherapy among Practicing Radiation Oncologists in the United States. *J Thorac Oncol*. 2013; 8(2):202–7.
121. Bender ET. Brain necrosis after fractionated radiation therapy: Is the half-time for repair longer than we thought? *Med Phys*. 2012; 39(11):7055–61.
122. Rancilio NJ, Dahl S, Athanasiadi I, Perez-Torres CJ. Design, construction, and in vivo feasibility of a positioning device for irradiation of mice brains using a clinical linear accelerator and intensity modulated radiation therapy. *Int J Radiat Biol*. 2017; 93(12):1321–6.
123. Kumar AJ, Leeds NE, Fuller GN, Tassel PV, Maor MH, Sawaya RE, et al. Malignant Gliomas: MR Imaging Spectrum of Radiation Therapy- and Chemotherapy-induced Necrosis of the Brain after Treatment. *Radiology*. 2000; 217(2):377–84.
124. Bojaxhiu B, Ahlhelm F, Walser M, Placidi L, Kliebisch U, Mikroutsikos L, et al. Radiation Necrosis and White Matter Lesions in Pediatric Patients With Brain Tumors Treated With Pencil Beam Scanning Proton Therapy. *Int J Radiat Oncol Biol Phys*. 2018; 100(4):987–96.
125. Boria AJ, Perez-Torres CJ. Minimal difference between fractionated and single-fraction exposure in a murine model of radiation necrosis. *Radiat Oncol Lond Engl*. 2019; 14(1):144.
126. Kondo N, Sakurai Y, Takata T, Takai N, Nakagawa Y, Tanaka H, et al. Localized radiation necrosis model in mouse brain using proton ion beams. *Appl Radiat Isot*. 2015; 106:242–6.
127. Moravan MJ, Olschowka JA, Williams JP, O’Banion MK. Cranial Irradiation Leads to Acute and Persistent Neuroinflammation with Delayed Increases in T-Cell Infiltration and CD11c Expression in C57BL/6 Mouse Brain. *Radiat Res*. 2011; 176(4):459–73.

128. Grahn D, Hamilton KF. Genetic Variation in the Acute Lethal Response of Four Inbred Mouse Strains to Whole Body X-Irradiation. *Genetics*. 1957; 42(3):189–98.
129. Hanson WR, Fry RJ, Sallèse AR, Frischer H, Ahmad T, Ainsworth EJ. Comparison of intestine and bone marrow radiosensitivity of the BALB/c and the C57BL/6 mouse strains and their B6CF1 offspring. *Radiat Res*. 1987; 110(3):340–52.
130. Perincheri S, Dingle RWC, Peterson ML, Spear BT. Hereditary persistence of α -fetoprotein and H19 expression in liver of BALB/cJ mice is due to a retrovirus insertion in the *Zhx2* gene. *Proc Natl Acad Sci U S A*. 2005; 102(2):396–401.
131. Ronchi JA, Figueira TR, Ravagnani FG, Oliveira HCF, Vercesi AE, Castilho RF. A spontaneous mutation in the nicotinamide nucleotide transhydrogenase gene of C57BL/6J mice results in mitochondrial redox abnormalities. *Free Radic Biol Med*. 2013; 63:446–56.
132. Constanzo J, Masson-Côté L, Tremblay L, Fouquet JP, Sarret P, Geha S, et al. Understanding the continuum of radionecrosis and vascular disorders in the brain following gamma knife irradiation: An MRI study. *Magn Reson Med*. 2017; 78(4):1420–31.
133. Belliveau J-G, Jensen MD, Stewart JMP, Solovey I, Klassen LM, Bauman GS, et al. Prediction of radiation necrosis in a rodent model using magnetic resonance imaging apparent transverse relaxation. *Phys Med Biol*. 2018; 63(3):035010.
134. Perez-Torres CJ, Engelbach JA, Cates J, Thotala D, Yuan L, Schmidt RE, et al. Toward Distinguishing Recurrent Tumor From Radiation Necrosis: DWI and MTC in a Gamma Knife–Irradiated Mouse Glioma Model. *Int J Radiat Oncol*. 2014; 90(2):446–53.
135. Boria AJ, Perez-Torres CJ. Minimal difference between fractionated and single-fraction exposure in a murine model of radiation necrosis. *Radiat Oncol*. 2019; 14(1):144.
136. Zilli T, Jorcano S, Bral S, Rubio C, Bruynzeel A, Oliveira A, et al. OC-0503: Weekly vs. every-other-day prostate cancer SBRT: 18-months results from a randomized phase II trial. *Radiother Oncol*. 2018; 127:S260.
137. Verma V, Simone CB. Approaches to stereotactic body radiation therapy for large (≥ 5 centimeter) non-small cell lung cancer. *Transl Lung Cancer Res*. 2019; 8(1):70–7.
138. Hasan S, Renz P, Packard M, Horrigan S, Gresswell S, Kirichenko AV. Effect of Daily and Every Other Day Stereotactic Body Radiation Therapy Schedules on Treatment-Related Fatigue in Patients With Hepatocellular Carcinoma. *Pract Radiat Oncol*. 2019; 9(1):e38–45.
139. Quon HC, Ong A, Cheung P, Chu W, Chung HT, Vesprini D, et al. Once-weekly versus every-other-day stereotactic body radiotherapy in patients with prostate cancer (PATRIOT): A phase 2 randomized trial. *Radiother Oncol J Eur Soc Ther Radiol Oncol*. 2018; 127(2):206–12.
140. Yamazaki H, Kodani N, Ogita M, Sato K, Himei K. Reirradiation of head and neck cancer focusing on hypofractionated stereotactic body radiation therapy. *Radiat Oncol Lond Engl*. 2011; 6:98.
141. Hernández L, Terradas M, Camps J, Martín M, Tusell L, Genescà A. Aging and radiation: bad companions. *Aging Cell*. 2015; 14(2):153–61.
142. Narendran N, Luzhna L, Kovalchuk O. Sex Difference of Radiation Response in Occupational and Accidental Exposure. *Front Genet*. 2019; 10.
143. Alsbeih G, Al-Meer RS, Al-Harbi N, Bin Judia S, Al-Buhairi M, Venturina NQ, et al. Gender bias in individual radiosensitivity and the association with genetic polymorphic variations. *Radiother Oncol*. 2016; 119(2):236–43.

144. Alkhorayef M, Babikir E, Alrushoud A, Al-Mohammed H, Sulieman A. Patient radiation biological risk in computed tomography angiography procedure. *Saudi J Biol Sci.* 2017; 24(2):235–40.
145. Roughton K, Boström M, Kalm M, Blomgren K. Irradiation to the young mouse brain impaired white matter growth more in females than in males. *Cell Death Dis.* 2013; 4(10):e897–e897.
146. Hagan C, D.V.M., Ph.D. When are mice considered old? The Jackson Laboratory.
147. Shiffrin RM, Börner K, Stigler SM. Scientific progress despite irreproducibility: A seeming paradox. *Proc Natl Acad Sci. National Academy of Sciences*; 2018; 115(11):2632–9.
148. Ioannidis JPA. Why Most Published Research Findings Are False. *PLOS Med. Public Library of Science*; 2005; 2(8):e124.
149. Prinz F, Schlange T, Asadullah K. Believe it or not: how much can we rely on published data on potential drug targets? *Nat Rev Drug Discov. Nature Publishing Group*; 2011; 10(9):712–712.
150. Williams Ruth. Can't Get No Reproduction. *Circ Res. American Heart Association*; 2015; 117(8):667–70.
151. Facts & Figures 2019: US Cancer Death Rate has Dropped 27% in 25 Years.